Nanoscale Interface Control for Advanced Electrochemical Devices

January, 2018

Doctor of Engineering

Pascal Sugri Fuseini Nbelayim

Toyohashi University of Technology,

Department of Electrical and Electronic Information Engineering

Chapter 1

General introduction

1.1 Nanoscience and nanotechnology [1]

Nanoscience and nanotechnology are currently one of the most, if not the most, important and researched areas in various scientific fields and engineering. This huge attention comes from mainly two reasons: 1) nanomaterials have high prospects in various technological applications because these materials usually show novel properties and functionalities; and 2) there is a huge potential of creating new knowledge from explaining size-dependent evolved properties, and in explaining new and hitherto unnoticed characteristics. Thus, nanoscale materials can be used to fabricate novel devices with enhanced properties and functionalities. A typical example of a nanomaterial has a different property from its bulk is a thin, ~ 60 nm, electrically conducting Au coating aggregating into particles above 120 °C and becoming non-conducting, while bulk Au will remain conducting even at 1000 °C. Studies to understand the phenomena in nanomaterials are now a common activity with graduate and postgraduate programs, and offered to students from different backgrounds in the sciences and engineering fields. There are also many international journals specifically dedicated to publishing research works on nanoscience and nanotechnology. Thus, there is currently a huge knowledge base on nanoscience and nanotechnology, with yet more new knowledge being added almost on the daily basis such that it becomes a big challenge for even an expert in the field to remain up-to-date.

The concepts of nanoscience and nanotechnology were first discussed by the renowned physicist Richard Feynman in 1959 in his talk, “There's Plenty of Room at the Bottom” [2], and well captured in his famous words, “the principles of physics, as far as I can see, do not speak against the possibility of maneuvering things atom by atom”. However, it was Norio

Taniguchi in 1974 who first used the term “Nanotechnology” [3]. And then in 1986, Drexler, inspired by Feynman, wrote his book, “Engines of Creation: The Coming Era of Nanotechnology” [4], in which he described nanotechnology as, “Nanotechnology is the principle of manipulation atom by atom, through control of the structure of matter at the molecular level. It entails the ability to build molecular systems with atom-by-atom precision, yielding a variety of nanomachines”.

However, although nanoscience and nanotechnology is a relatively new term, in nature and in practice, there were, and are, many objects/activities that function/were practiced on a micro and nanoscale. For example, the bacterial or archaeal flagella, which are on the size scale of 20-30 nm, can reach rotations over 10000 rpm, powered by the flow of ions and ATP over membranes, respectively. These can be considered biological molecular machines. Another example is in the famous coloured glasses of medieval churches which were achieved by the dispersion of metallic nanoparticles in the glass matrices. However, the important point to note here is that, the understanding and control which modern nanotechnologists have were not available in these ancient technologies.

1.1.1 Definition of nanoscience and nanotechnology

The term “nano” comes from the Greek word “nanos” for “dwarf” and adopted into the scientific field of the metric system to mean 1 billionth (1/1000,000,000), i.e. 1 nm is 1 billionth of a meter. To put it in perspective, the smallest feature that the unaided human eye can resolve is more than 10,000 nm across.

Generally, nanoscience is defined as the fundamental study of the principles of molecules or structures with at least one dimension roughly between 1 and 100 nm, to reflect the fact that quantum mechanical effects are important at this size realm. Whiles nanotechnology refers to the application of nanoscience and nanomaterials into useful nanoscale materials or devices. The typical length of a C-C bond in a molecule is about 0.12-0.15 nm, whiles the diameter of

a double helix DNA strand is about 2 nm. Thus, the conventional limit range of 1-100 nm were selected such that the lower limit of 1 nm was to reflect the fact that a nanomaterial/device should be bigger than an atom (with the ~ 0.25 nm size of the smallest atom from hydrogen in mind) since nanotechnology must build from atoms and molecules. The upper limit of 100 nm is somewhat arbitrary but with the intention that around and below this size phenomena not observed in the bulk will be observed [*The National Nanotechnology Initiative, USA*].

1.1.2 Applications of nanoscience and nanotechnology

Science and technology is an ever evolving field with the consequent results of generally replacing old devices and technologies with new and/or improved ones. A little history in the past centuries suggests that every century experiences approximately 2 major technological revolutions, e.g. in the 18th century it was textile and rail; in the 19th century it was rail and automobile; in the 20th century was computer and nanotechnology; and in our current 21st century it appears to be nanotechnology and genetic engineering.

Using nanosystems, better and cheaper products can be obtained to replace those obtained by using conventional bulk materials. Many technological predictors had predicted many possible applications of nanotechnology which seemed like science fictions then, however today they are normal realities. Thus, presently there are many fascinating achievements based on nanotechnology such as: sub-wavelength metallic nanostructures that exhibit plasmonic resonance phenomenon with unlimited applications such as cancer therapy, enhanced light absorbance by photonic materials, especially in photovoltaic (PV) systems, photocatalysis, photosensing applications such as Raman spectroscopy, etc. Carbon nanotubes are the stiffest materials measured today (Young modulus of ~ 1000 GPa) and are used to reinforce the polymer matrix in certain high performance graphite-fiber composites. Their addition in graphite photoanodes increase the capacity of lithium ion battery by about

20 %. Quantum dots are used as biological tags and also used in electro-optic devices as luminophores [5].

There are predictions for advanced future applications of nanotechnology such as performing surgery at cellular and molecular levels; computers smaller than a speck of sand; nanorobots to repair defective airframes and ship hulls before they are damaged; prevention of money laundering by imprinting every computer digit; etc. [1].

Thus, the general, fundamental and ultimate aim of this research is the effective usage of nanofabrication to reduce device-fabrication material yet achieve enhanced functionality; with a narrowed focused in two main areas : a) electrowetting - where nano-coated films were used to achieve highly non-wetting robust superhydrophobic surface and a much desired extremely low actuation voltage (3 V) reversible electrowetting robust surface; b) the use of plasmonic nanostructures in dye-sensitized solar cells (DSSCs) to extremely enhance light absorption, with the ultimate aim of highly enhanced power conversion efficiency (PCE) and reduction in the photoanode fabrication material. Although some successes have been achieved in this area however, these achievements are below expectation and still riddled with controversies regards the role of the plasmonic nanostructures. Hence, under this area we used various Ag@TiO_2 core-shell nanostructures to study the effect of plasmonic nanostructures on the performance of DSSCs, with the aim of increasing the understanding of the role of plasmonic nanostructures in DSSCs for the ultimate aim of achieving this laudable predicted potential.

1.2 Superhydrophobic coatings and electrowetting

1.2.1 Superhydrophobic surfaces

When water is poured onto a surface and the adhesive forces between the liquid water and the solid surface are stronger than the cohesive forces between molecules of the water, the water

spreads on (wets) the surface, and the surface is said to be hydrophilic (water-loving). If on the other hand the cohesive forces are stronger than the adhesive forces the water rounds up into a non-wetting spherical balls or beads and the surface is termed hydrophobic (water-fearing). The extent of the spherical shape of the beaded water depends on the difference between the cohesive and adhesive forces such that a high cohesive force and a low adhesive force leads to a more spherical or higher non-wetting state. Wetting can be quantified by the contact angle (CA), given as Θ in Fig. 1.1.

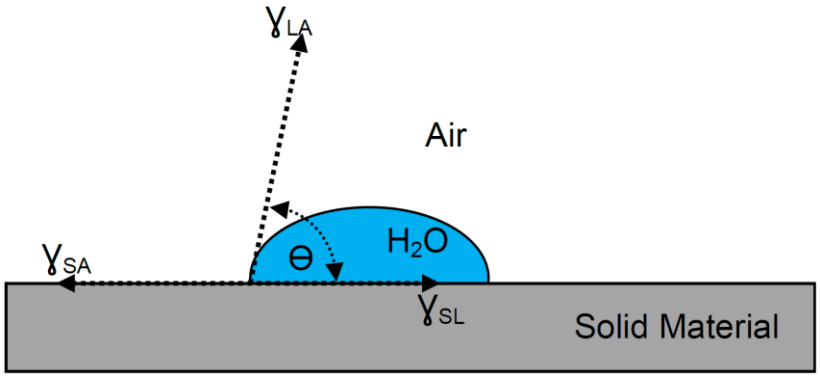

Fig. 1.1 Schematic of the balance of interfacial energies about a water droplet on a solid surface.

The CA is the angle a liquid droplet makes at an interface when it comes in contact with another phase such as a solid surface. By this CA, surfaces are conventionally classified into various states of wetting by the terms, Superhydrophilic, Hydrophilic, Hydrophobic and Superhydrophobic when $\Theta < 10°$; $10° < \Theta < 90°$; $90° < \Theta < 150°$; and when $\Theta > 150°$, respectively [6]. These are schematically illustrated in Fig. 1.2.

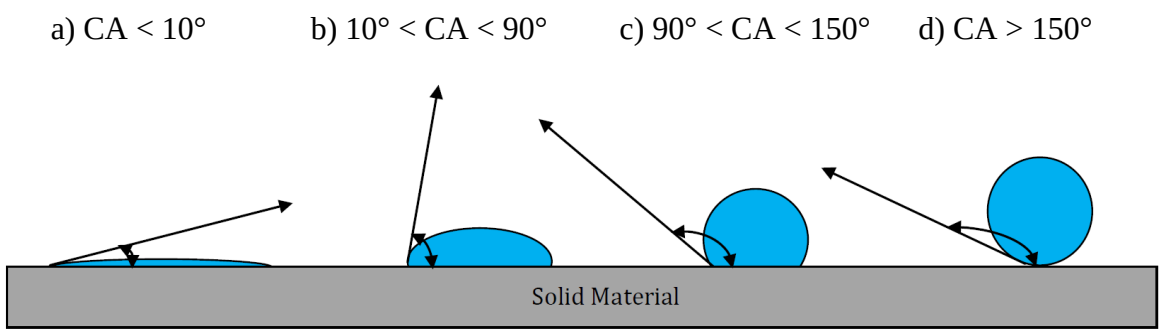

Fig. 1.2 Schematic of: **a)** superhydrophilic, **b)** hydrophilic, **c)** hydrophobic, **d)** superhydrophobic surfaces.

In terms of thermodynamic considerations, the shape of a liquid droplet on a surface at thermodynamic equilibrium is governed by the balance of three interfacial tensions/energies: the solid-liquid (γ_{SL}), the solid-air (γ_{SA}) and the liquid-air (γ_{LA}), as shown in Fig. 1.1. In the situation where the system is in a medium other than air, oil for example, the solid-air and liquid-air interfacial energies would be replaced by solid-oil and liquid-oil interfacial energies, respectively.

1.2.1.1 Interfacial (surface) Tension? Or Interfacial (surface) Energy?

Surface Tension is force per unit length (N/m), whiles surface (free) energy is energy per unit area (J/m^2). Hence these two concepts, surface tension and surface free energy, are equivalent but are a matter of mechanical and mathematical approaches, respectively [7]].

In 1805 the British Physicist, Thomas Young, found a relationship involving the CA and the balanced forces at the triple-point (the point at which all three phases contact), known famously as the Young equation, given in eqn.1.1 below:

$$\gamma_{LA}\text{Cos}\Theta = \gamma_{SA} - \gamma_{SL} \qquad \text{— (1.1)}$$

This relation is based on the assumption that the droplet is on an ideal surface. An ideal surface being one that is flat, rigid, perfectly smooth, chemically homogeneous, and has zero contact angle hysteresis (where, CA hysteresis is the CA difference between an advancing CA and a receding CA when the surface on which a droplet is resting is tilted to the point the droplet begins to roll away).

From Young's eqn. it can be observed that by manipulating the interfacial energies (γ) a particular Θ value can be obtained, and hence resulting in a particular wetting surface type (e.g. hydrophobic or hydrophilic). For a hydrophobic surface, γ_{LA} will be constant since the liquid would be water, and γ_{SL} will also be relatively constant as its value depends partially on the liquid water (which is constant) and solid surface. This leaves for only γ_{SA} for manipulation. Hence by lowering the surface energy of a material (i.e. low γ_{SA}) it is possible to obtain $\Theta > 90°$. This is usually done by chemically modifying the surface (usually by various coating methods) with low surface energy materials. This is known as hydrophobizing. These materials are usually non-polar polymeric materials that are repellent to polar liquids like water. The most commonly used ones are the fluoroalkanes and their derivatives.

Fluoroalkanes are organic compounds in which saturated carbon backbone chains are bonded to fluorine atoms, e.g. perfluorohexane, Fig. 1.3 a). The high electronegativity of fluorine reduces the polarizability of the atom [8]. Fluorocarbons are only weakly susceptible to the fleeting dipoles that form the basis of the London dispersion force. As a result, fluorocarbons

have low intramolecular attractive forces and are lipophobic and oleophobic, in addition to being hydrophobic. Thus fluorocarbons find applications as oil-, water-, and stain-repellants. This same high electronegativity of fluorine imparts partial ionic character through partial charges on the carbon and fluorine atoms, Fig. 1.3 b) [9].

Fig. 1.3 Structural formula of: **a)** perfluorohexane *(Wikipedia)*; and **b)** partial charges on the polarized carbon—fluorine.

These partial charges shorten (strengthen) the bond through favorable coulombic interactions. Additionally, multiple carbon–fluorine bonds increase the strength and stability of other nearby carbon–fluorine bonds on the same geminal carbon, as the carbon has a higher positive partial charge [8]. Furthermore, multiple carbon–fluorine bonds also strengthen the "skeletal" carbon–carbon bonds from the inductive effect. This makes fluoroalkanes, generally, chemically and thermally stable.

Examples of some common low surface energy materials used for hydrophobizing surfaces are: fluoralkylsilanes (FAS) (e.g. heptadecafluorodecyltrichlorosilane and heptadecafluorotrimethoxysilane); other silanes; fluoropolymers (e.g. PTFE and polyvinylidene fluoride); organic polymers; paraffin wax; alkylketene dimer; fluorine

compounds (e.g. graphite fluoride and tetrafluoroethylene); polydimethylsiloxane; and carbon or carbon nanotubes [6].

However the maximum attained CA by chemical modification of a surface known is 119°; obtained from a smooth homogeneous surface with regularly well aligned closest-hexagonally-packed —CF_3 groups [10]. Thus, obtaining a superhydrophobic surface (SHS), CA > 150°, involves more than just the chemical modification of surface energy. Barthlott and Neinhuis in their scanning electron microscopy (SEM) analysis of water-repellent self-cleaning plant surfaces, they showed that these surfaces combined microstructures and wax on their surfaces, which afforded them their water repellency. This paved the way for biomimicry in the preparation of highly water repellent SHSs. Hence techniques of preparing SHSs involve a combination of appropriate roughness topographical and chemical modifications of a surface. Fig. 1.4 shows the lotus plant, SEM images of the hierarchical roughness of the leaf surface, and the self-cleaning effect.

Reference [11] describes various preparatory techniques and results on SHSs, grouping the preparatory techniques into two major approaches based on the established topography-surface energy modification approach of preparing superhydrophobic surfaces: a) roughening a low surface energy material/surface; and b) an initial preparation of a rough surface and subsequently coating it with a low surface energy material.

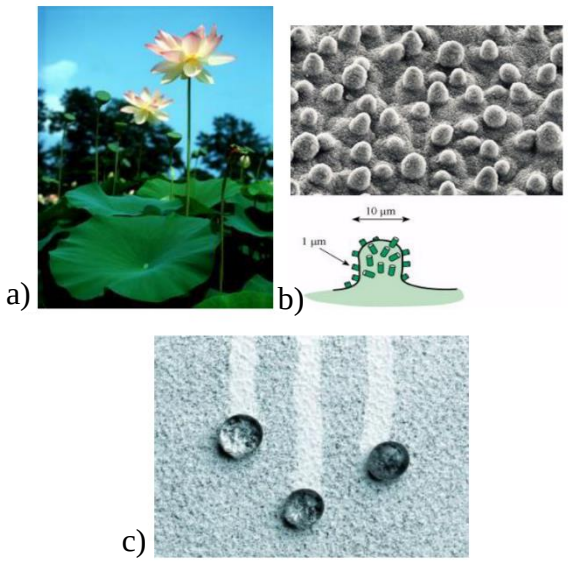

Fig. 1.4 a) Lotus leaf; **b)** SEM image of the lotus leaf surface with micro-nubs (above), and a schematic of nano epicuticular wax crystalloids on them (below); **c)** Rolling liquid droplets showing self-cleaning effect. [*www.lotus-effekt.de*].

The various techniques employed in the roughening of low surface energy materials (LSEMs)/surfaces approach are mostly one-step processes and have the advantage of simplicity. However, they are limited to a small set of LSEMs. On the other hand SHS preparation via roughening and subsequent coating with LSEM separates the surface properties from the bulk properties of the material and expands the potential applications of such surfaces [11]. However, many of the processes involve relatively complex and/or sophisticated equipment or processes, eg electrochemical reaction process involves an electrochemical bath setup; or etching and lithography, which are relatively complicated and laborious or sophisticated processes. These suggest that many of these approaches are expensive.

Therefore, our main aim under this area of the thesis is to use a SHS preparation approach that would be simple, inexpensive and environmentally friendly. We used sol-gel - a versatile and low temperature process, to make a porous alumina coating on a glass substrate; hot-water treatment (HWT) - a low temperature, environmentally friendly, simple and inexpensive process to precipitate the porous alumina into rough pseudoboehmite structures; and finally hydrophobizing the rough pseudoboehmite structures using solution LBL process - an inexpensive, easy and conformal coating process. These processes will be described further ahead.

1.2.1.2 Quantitative superhydrophobicity

For surfaces with rough texture the Young's model/eqn. for a droplet on an ideal surface cannot be used, hence the need for alternative models. Currently the two major models that dominate in reported research works are the Wenzel and Cassie-Baxter models. Wenzel proposed a model in which the liquid droplet wets the rough structures to produce a homogenous liquid-solid interface, Fig. 1.5 a). He proposed a Wenzel CA, Θ_W, by modifying the Young eqn. for a droplet on a surface with rough texture as [12]:

$$\mathrm{Cos}\Theta_W = r(\gamma_{SA} - \gamma_{SL}) / \gamma_{LA} = r\mathrm{Cos}\Theta \qquad \text{— (1.2)}$$

r = (area of actual rough surface) / (area of projected rough structures). This implies $r > 1$, and dimensionless.

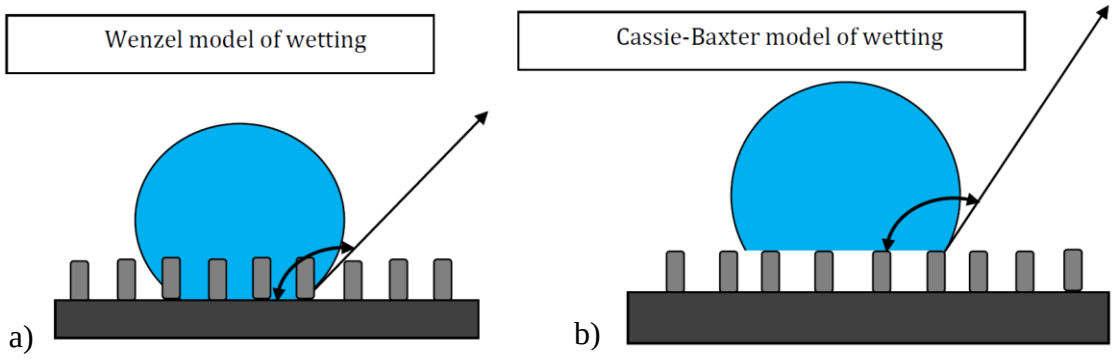

Fig. 1.5 Schematic of wetting of a liquid droplet on a rough surface: **a)** Wenzel's model, and **b)** Cassie-Baxter model.

Cassie and Baxter on the other hand modified the Wenzel model to propose a model in which the droplet sits on top of a composite of solid rough structures and air-filled spaces (if measurement is in an air medium) between the rough structures (Fig. 1.5 (b)), giving a composite solid-liquid-air interface. They predicted a CA, Θ_C, for a droplet on a rough surface [13] as:

$$\mathrm{Cos}\Theta_C = f\mathrm{Cos}\Theta + (1-f)\mathrm{Cos}\Theta_f = f(\mathrm{Cos}\Theta + 1) - 1 \qquad \text{— (1.3)}$$

f = fraction of solid surface area in contact with the droplet, $f < 1$; $(1-f)$ = the fraction of fluid medium between rough structures (air fluid is assumed to obtain the third term of eqn. (1.3)) in contact with the droplet; and Θ_f = CA of droplet with the fluid medium (180° assumed, because water does not wet air [14]).

[Note: the CA for a rough surface is sometimes called the "Apparent CA" whiles that for a smooth surface the "Intrinsic CA"].

The Wenzel model, with $r > 1$, predicts an increase in CA for a roughened hydrophobic surface, i.e. with its initial $\Theta > 90°$, and a decrease in CA for a roughened hydrophilic surface, one with its initial $\Theta < 90°$. The metastable Cassie-Baxter model on the other hand allows for the possibility of increase in CA for a roughened surface even when $\Theta < 90°$. These two models have their limitations though. Some researchers have recently reported their research results and theoretical considerations to express some of these limitations, and subsequently proposed modifications to them, especially so for the Cassie-Baxter model, which is frequently used for most SHSs discussions. For example, according to Nosonovsky and Bhushan [15, 16] the Cassie equation (eqn. (1.3)) is based on the assumption that the heterogeneous surface is composed of well-separated distinct patches of different material, so that the free surface energy can be averaged. But they claim this is not so in real situations. They also argue that when the size of the chemical heterogeneities is very small (of atomic or molecular dimensions), the quantity that should be averaged is not the energy, but the dipole moment of a macromolecule, referencing [17], and that the first part of eqn. (1.3) should be eqn. (1.4) instead [16]:

$$(1 + \mathrm{Cos}\Theta_C)^2 = f(1 + \mathrm{Cos}\Theta)^2 + (1 - f)(\mathrm{Cos}\Theta_f)^2 \qquad \text{— (1.4)}$$

and corroborated with experimental studies of polymers with different functional groups showing good agreement with eqn. (1.4) [18].

1.2.2 Electrowetting (EW)

Dynamic wettability control or the manipulation of the wetting behavior of surfaces (wettability tuning) is a fascinating phenomenon with both academic and commercial applications (e.g. variable liquid lens in mobile cameras *(Varioptic Co.)*, electronic display units by *Liquavista*, electronic paper [19] and many more potential novel applications).

Wettability tuning, which is basically switching between, or within, superhydrophobic and superhydrophilic states, can be achieved in many ways. Two of such ways have been described already as the chemical modification of hydrophilic surfaces into hydrophobic surfaces, and topographical cum chemical modifications into superhydrophobic surfaces. Here we are interested in relatively short time period switching, which can be obtained by various methods which include photo/UV irradiation [20]; pressure/temperature induced switching [21]; pH change [22]; electrowetting [23]; etc. EW is currently one of the promising and most widely used techniques for manipulating tiny amounts of liquids on surfaces [24]. The main disadvantage of chemical and topographical patterns is their static nature, which prevents active control of the liquids. Considerable work has been devoted to the development of surfaces with controllable wettability, typically coated with self-assembled monolayers. Notwithstanding some progress, the degree of switchability, the switching speed, the long term reliability, and the compatibility with variable environments that have been achieved so far are not suitable for most practical applications. In contrast, EW has proven very successful in all these respects: contact angle variations of several tens of degrees are routinely achieved; switching speeds are limited (typically to several milliseconds) by the hydrodynamic response of the droplet rather than the actual switching of the equilibrium value of the contact angle; hundreds of thousands of switching cycles have been performed in long term stability tests without noticeable degradation [25, 26].

These days droplets can be moved freely along programmable paths on surfaces: they can be split, merged and mixed with a high degree of flexibility. Most of these results were achieved within the past five years (2000-2005) by a steadily growing community of researchers in the field [27] [24].

EW is, basically, the application of electric voltage to increase the wetting of a polar or electrically conductive liquid on a surface. Jean Berthier in chapter 4 of his book, Microdrops

and Digital Microfluidics, describes: in the presence of a DC or AC current electric field, electric charges gather at the interface between a conductive and non-conductive (dielectric) material. The same electric field that induces these charges then couples with the interfacial charges to exert an interfacial force, and if the interface is deformable (such as that of a conductive liquid and non-conductive fluid or gas) this force can distort the interface. These induced interfacial electric forces are especially strong on a liquid-gas interface at the vicinity of the contact line, as the electric field often becomes singularly large at the sharp wedges near the contact line [the triple contact line of the liquid droplet, the surrounding fluid medium and the solid surface]. The physics describing the electric forces on interfaces of conducting liquids and on the triple contact lines is called “electrowetting”. Basically the electrostatic field destabilizes the balanced forces acting on the droplet at equilibrium; the liquid droplet adjusts itself to restore the balance, forming a new equilibrium and resulting in EW.

Gabriel Lippmann, in 1875, in his studies of electrocapillarity described that it was possible to manipulate the height of mercury in a column in contact with an electrolyte by the application of a voltage between the mercury and the electrolyte [28]. This is now generally considered to be the beginning of the present EW phenomenon. But it was Gerardo Beni and Susan Hackwood who introduced the term “electrowetting” in 1981[29]. Lippmann proposed practical applications of his work but was mostly restricted by the decomposition of the aqueous electrolytes used, due to electrolysis, when more than a few 100 mV was applied [24]. Bruno Berge in the early 1990s suggested a thin layer of insulating material between the solid metallic surface and conducting liquid droplet to overcome the electrolysis problem [23]. Today this system has come to be known as electrowetting on dielectric (EWOD).

The theory of EW has been studied by various researchers from various fields: physics, physical chemistry, electrochemistry and electrical engineering. Hence there are various

approaches to describing the EW phenomenon. However, there are three common major approaches: classical thermodynamic approach, energy minimization approach and the electromechanical approach [24]. Jean Berthier's description of EW above is an example of an electromechanical approach; due to the electrostatic modification of the liquid-solid interfacial energy, which results in EW, an electrostatic capacitive energy component was added to the Young equation to obtain the famous basic EW equation known as the Lippmann-Young equation, derived by Berge and based on energy minimization approach [23] for EWOD:

$$\mathrm{Cos}\Theta_v = \mathrm{Cos}\Theta + \varepsilon_o\varepsilon_r V^2 / 2d\gamma_{LA} \qquad \text{— (1.5)}$$

Where Θ_v is the electrowetted CA; ε_o is permittivity of free space; ε_r is dielectric constant of insulating material; V = applied voltage; d = thickness of insulating material layer.

Eqn. (1.5) is found to hold true until a certain threshold voltage beyond which CA does not change with further increase in voltage [24]. This is called CA saturation. This observation has been reported in many research results [30-35]. Eqn. (1.5) thus, does not explain CA saturation. However other studies [34, 36] suggest that the electric field strength diverges close to the triple-contact line generating a strong electric field, ~ 100s of volts per micrometer, causing the CA saturation. Currently there is no exact explanation for CA saturation, but there are some proposed mechanisms/reasons: e.g. Verheijen and Prins [31] have suggested charge injection into the insulating material at high voltages; some others [30, 32] have suggested a deviation from the assumption of a perfect conducting liquid or a perfect non-conducting dielectric material. Mugele and Baret in their review [24] think that there may not be a unique cause, but a complex of causes due to the electric field divergence at the triple-contact line, and depending on conditions of an experiment, a particular cause, or combination, may cause the effect.

1.2.2.1 Quantitative EW on Structured Surfaces

For a wider range of CA changes by EW, a high initial CA would be needed, and that is obtained from SHSs. Eqn. (1.5) is for planar surfaces, hence it would have to be adapted for SHSs which have roughness. This was done by Torkelli [37] in the form:

$$\mathrm{Cos}\Theta v = \mathrm{Cos}\Theta c + \varepsilon_o \varepsilon_r f V^2 / 2d\gamma_{LA} \qquad \text{— (1.6)}$$

Torkelli in his thesis [37], in the explanation of the results of Johnson and Dettre [38], on the relationship between roughness ratio and CA, said that when roughness on a surface is gradually increased from a minimum, first the advancing CA increases and the receding CA decreases causing high CA hysteresis; and when the roughness becomes steep enough, the receding CA also begins to increase till a particular roughness when both CAs become equal, i.e. with no CA hysteresis. This is said to happen when both geometrical and energy conditions are favorable to allow the droplet to come in contact with only the tips of the rough structures, trapping air in the spaces between the structures, and between the droplet and the real surface giving the Cassie-Baxter metastable state. Using illustrations, Fig. 1.6, he further explained that at the microscopic level, the local droplet CAs, Θ_o, with the rough structures are predicted by Young's eqn., and the liquid tries to form concave menisci between the surface structures if the slope, α, is too low, Fig. 1.6 a). The concave menisci cause capillary wetting to the surface.

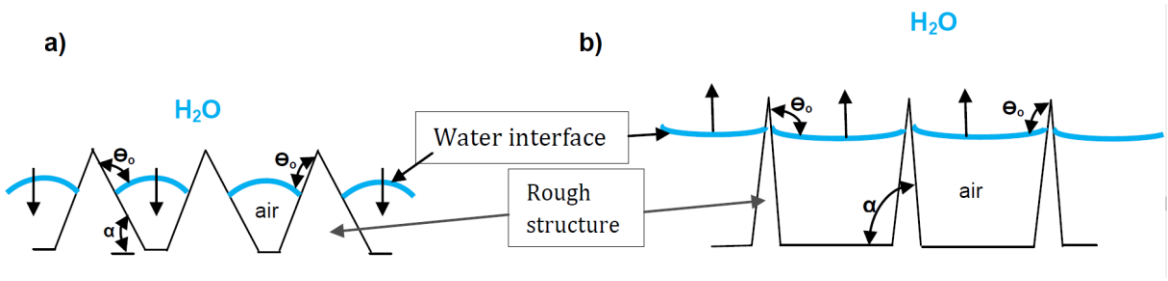

Fig. 1.6 Schematic of water (menisci) on rough hydrophobic structures, showing the geometric effect on wetting of SHSs with: **a)** low and **b)** high slope structures.

When α becomes high, Fig. 1.6 b), the liquid droplet forms convex menisci resulting in a negative capillary action that drives liquid from the surface, resulting in the Cassie-Baxter composite of air-rough structures between the droplet and the solid surface proper. These deductions can be seen more clearly in the capillary height equation such that when the menisci are concave it implies $\Theta_o < 90°$, giving a positive capillarity; and when they are convex, $\Theta_o > 90°$, giving a negative capillarity effect. The droplet mass is supported by the negative capillary pressure of these small liquid membranes/interfaces. From Fig. 1.6 Torkelli deduced a geometric criterion for the Cassie-Baxter composite surface as:

$$\alpha \geq (180° - \Theta_o) \qquad \text{— (1.7)}$$

When voltage is applied to a droplet on a SHS, there is both a lateral and a vertical (capillary) wetting. The electrostatic force generated, which is strongest at the triple contact line point, pushes the liquid droplet laterally, spreading the liquid droplet. At the same time the wetting of the structures occur by capillary effect, by the electrostatic force forcing a transition of the menisci of the droplet from an initial convex state to a concave state, thereby causing capillary wetting. This transition occurs at a threshold EW voltage, called the *capillary threshold voltage*, when the local CAs, Θ_o, become < 90° [49]. Our rough pseudoboehmite

structures in this thesis were random, as shown in the schematic in Fig. 1.7, hence the model explanation in Fig. 1.6 may not accurately fit that for our rough surface EW, but it at least serves a good guide in the explanation and understanding of our system.

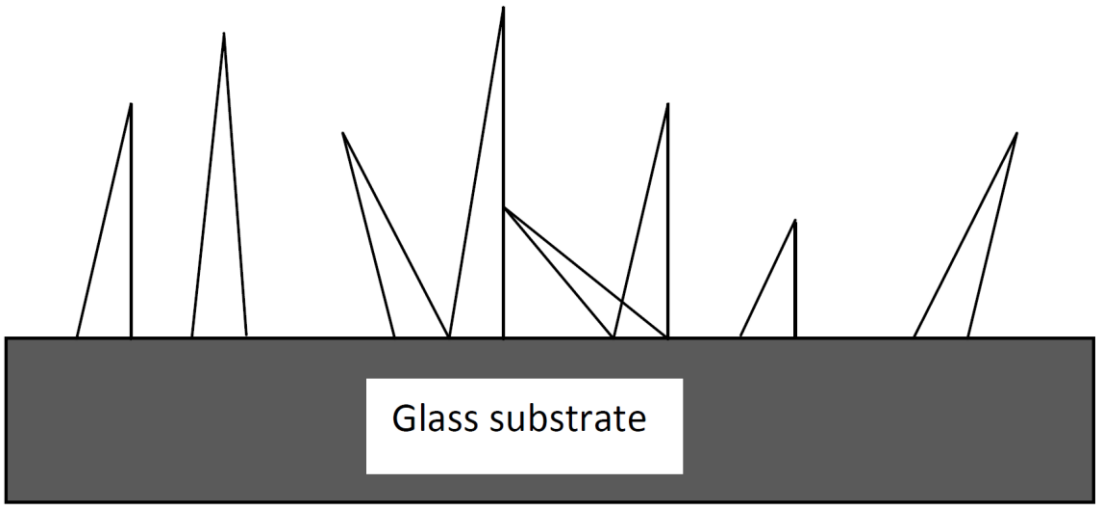

Fig. 1.7 Schematic of our sample showing random rough pseudoboehmite structures on glass substrate.

1.2.2.2 Theoretical basis for the choice of fabrication materials

From eqn. (1.6) the factors that can easily be manipulated to obtain particular desired EW results are ε_r, Θ_c, f and d. The critical concern for the choice of materials in an EW system is to obtain a robust EW system and low voltage application (as a form of low energy consumption) for various CA changes. By decreasing ε_r, the capacitive electric field is also reduced and hence a higher voltage would be needed for a particular CA change. Thus a higher ε_r would be more desirable. However, generally, materials with high ε_r easily break down under intense electric field, although the electric break down also depends on some other properties of the dielectric material, such as its thickness, roughness, nature and

temperature. Thinner materials, generally, have lower dielectric break down values. Hence the dielectric material would have to be chosen carefully when considering its ε_r. A higher Θ means a wider range of CAs from EW, and also implies, from eqn. (1.6), a smaller voltage would be needed to decrease CA. A smaller f would, generally, give a higher Θ_c, from eqn. (1.2). Decreasing the thickness, d, of the dielectric material would decrease how much voltage would be needed for a particular decrease in CA, eqn. (1.6). However, due to the dependence of the possible dielectric break down on the thickness (mentioned above), there is usually a limiting minimum thickness it can be decreased to, in order to be able to use practical voltages for EW [40]. Other desirable material properties for an EW system include: chemical inertness and stability for good reproducibility and durability; the liquid droplet should be a perfect conductor, one of the assumptions on which the EW equation was derived, which is usually achieved by the use of salt solutions (~ 0.01 – 1 M). The concentration and ionic species of the salts used having negligible effects on the EW performance results [24], except for situations such as adsorption of bimolecular ionic species [41], or pH dependent deviations (from eqn. (1.5)) attributed to specific adsorption of hydroxyl ions into insulator material surfaces [42]. In this thesis we used the same material, Au, as both the conducting layer on the substrate and the conductor wire inserted into the droplet to prevent redox reactions during EW, and also because Au is relatively inert. Our dielectric materials consisted of alumina coating (which also served as the roughening material for superhydrophobicity), and a FAS (Heptadecafluorodecyltrimethoxysilane) material as the hydrophobizing material (because we feared, the Nafion® hydrophobizing material, which exhibited very high CA hysteresis might have some undesirable and/or complex effects on the EW system). Alumina is a known good dielectric material with low dielectric constant. Its thickness was about 250 nm. These properties were expected to give a stable and low actuation EW voltage. Also the FAS used, with its many fluoro-carbon bonds, was expected

to give a high water droplet repellency (high Θ) with low CA hysteresis, and also exhibit a high chemical stability.

1.2.3 Reversible EW (REW)

From the discussions made on EW so far, it can be deduced that after EW, when the voltage is removed, an electrowetted droplet should transition back to its original wetting state before the voltage was applied. That is, from eqns. (1.5) and (1.6), Θ_V should return to Θ and Θ_C, respectively. However many research results indicate that EW in an air medium is usually irreversible. This has been explained to be due to surface heterogeneity; both physical and chemical. Krupenkin et al. [43] explained that when a voltage is applied to a droplet on solid surface, the solid-liquid interfacial energy is modified causing the droplet to spread, and by this a sizable energy is dissipated leading to a minimum energy state of the electrowetted droplet its pinning to the solid surface. So that when the voltage is removed the droplet would prefer to remain in the minimum energy state, as many systems. Halim et al. [44] added that during the EW process a solid-gas-liquid composite interface is replaced by a solid-liquid interface, also suggesting a dissipation of energy to form the new solid-liquid interface state. Thus, based on these proposed explanations, 3 major approaches have been proposed for REW:

(1) The thermal approach: this involves providing additional energy to the electrowetted system, apparently to replace the dissipated energy, to return the droplet back to its initial position. This approach has been reported by Krupenkin et al. [43] in which they used a short pulse of electricity to rapidly heat their substrate evaporating part of the droplet into a thin layer of vapour at the solid-liquid interface, disconnecting the droplet from the substrate surface and returning it to its initial state before EW. However this is considered impractical for actual application.

(2) The geometric approach: this involves engineering nanostructures for superhydrophobicity such as to minimize the energy dissipation during EW in order to reduce or eliminate the energy barrier for transitioning back to the original state. Hallim et al. [44] published a work on this; using lattice Boltzman simulations they were able to select relevant experimental parameters to construct a SHS of parallel grooves with an aspect ratio that allows for controlled, barrierless (energetically) EW and REW.

(3) The competitive two liquid wetting approach: this is usually achieved using a liquid water droplet in a liquid oil medium. This is the most common approach used [45-49]. The basic principle is that the oil provides a kind of "lubricating" effect to prevent the droplet from pinning onto the surface, during EW, such that when the voltage is removed the droplet can transition back to the original state usually via a capillarity effect.

In this thesis we used the competitive two-liquid wetting system approach, using a glycerin-KCl-water electrolyte system droplet, in a dodecane medium. We have provided a schematic of the REW phenomenon by competitive two liquid wetting in Fig. 1.8. Oils, with usually lower surface tension than aqueous liquids, would preferentially wet a hydrophobic surfaces (or SHSs) compared to aqueous liquids because the SHS-oil surface tension difference is lower than the SHS-aqueous liquid surface tension difference. So that a SHS in an oil medium would have a droplet sitting on a film of oil between it and rough structures, and with oil between the inter-rough structure spaces, Fig. 1.8 (1). When a voltage is applied to the droplet, the droplet pushes the oil out during the EW process, as shown by the arrows in Fig. 1.8 (1)-(2). However, a thin film of oil remains between the droplet and the rough structures as long as the EW force does not exceed the surface tension of the oil to de-wet (break) the oil into microscopic droplets [50]. This remnant oil prevents the pinning of the droplet. When the voltage is removed, the oil refills into the inter-rough structure spaces by capillary action and with time the oil completely refills the spaces lifting up the droplet back

to its original state, Fig. 1.8 (3)-(4). The process of competitive two liquid REW is affected by the viscosities of the oil and droplet via their effect on the capillary diffusion process.

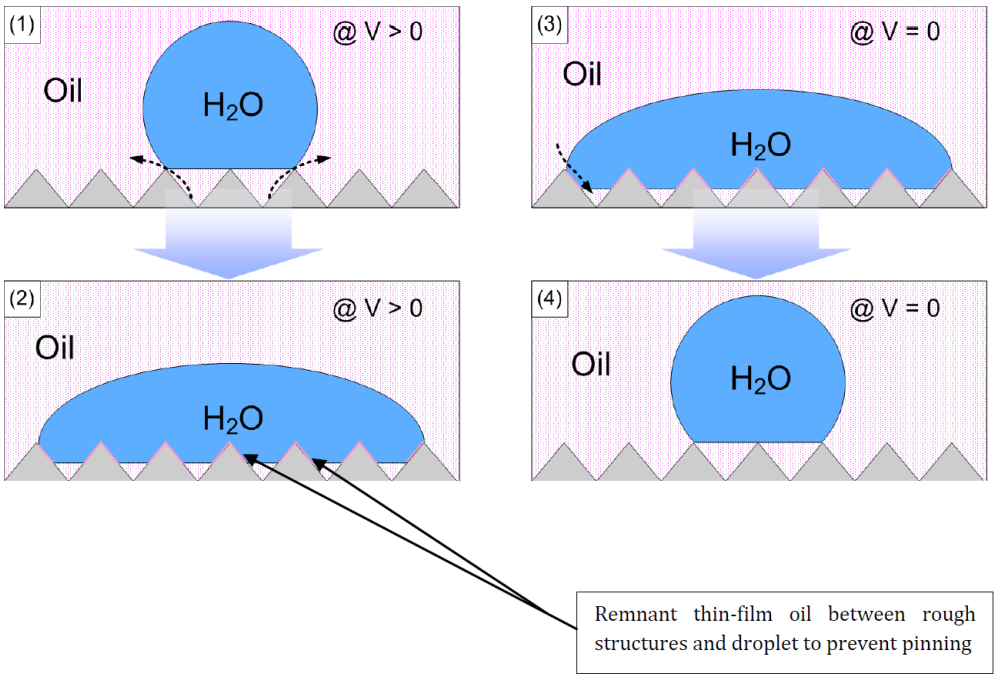

Fig. 1.8 Schematic of EW [(1)-(2)] and REW [(3)-(4)] of an aqueous droplet on SHS in an oil medium: (1) voltage applied to droplet and droplet pushes oil out from rough structure spaces; (2) thin film of oil between rough structures and electrowetted droplet to prevent pinning; (3) voltage removed and oil refilling into spaces by capillary action; (4) oil refills spaces and reverses droplet back to original state.

1.3 Photovoltaics/Solar cells (Dye-sensitized solar cells)

The world population is increasing with growing and emerging economies; and fossil fuel, the major energy source (> 80 % [51]), is finite, depleting and possesses environmental concerns. The most prominent issue is its release of CO_2, causing global warming and its consequent negative environmental effects. This has instigated the search for alternative energy sources that are renewable, low-cost, eco-friendly and sustainable. So far the common

alternative energy sources include, geothermal, biomass, hydropower, wind and solar. Among these, solar is apparently one of the best options as it is clean, inexhaustible and free of cost, with the thermonuclear fusion reactions of the sun exuding a large amount of energy (3.89×1026 J s^{-1}) from its core. While only a fraction of this energy enters the Earth's atmosphere, known as the solar constant (~ 1.367 kW m^{-2}), it is nevertheless still a large amount, as N. S Lewis [52] aptly puts it in perspective, "More energy from sunlight strikes Earth in one hour than all of the energy consumed by humans in an entire year. Thus, photovoltaics (PVs) seem to be the most viable in the search for alternative energy sources. Currently, the most commercially available PVs/solar cells are the solid-state p-n junction cells, most especially the Si-based (well-studied/mature first-generation PV) solar cells, and these are relatively expensive due to the high crystallinity, purity and the thick active material requirements. The second-generation (thin-film) PVs were designed in the form of thin films (1-4 μm) to reduce cost. Examples of these include, amorphous and polycrystalline Si, cadmium telluride (CdTe), copper-indium-selenide/diselenide (CIS) and copper-indium-gallium-selenide/diselenide (CIGS). Then came the third-generation/emerging PVs with novel designs over the 1st and 2nd generation PVs to increase performance at an even lower cost. Additionally, since they are in their pre-/non-commercialized stages yet they will be, and are, a great source of research interest. They include the dye-sensitized solar cell (DSSC) and its close relatives (organic solar cells, perovskite solar cells and quantum-dot solar cells); concentrating PV and novel & emerging solar cell concepts [53].

A solar cell is basically a device that can convert light energy directly to electricity via the PV effect. Such a device should possess these three principal features:

a) Ability to absorb light and generate electron-hole pair charge carriers

b) Separation of these charge carriers and

c) Extraction of these charge carriers to an external circuit.

1.3.1 Dye-sensitized solar cells

1.3.1.1 A Brief history of solar cells to DSSCs

Table 1.1 summarizes significant events in the history of the DSSC. The history of solar cells began in 1839 when French physicist Alexandre-Edmond Becquerel observed the generation of electricity between two Pt electrodes immersed in an acidic solution of AgCl under illumination (photovoltaic effect), with increasing magnitude as the intensity of illumination increased [54]. In the present day, this is considered as an electrochemical cell.

Moser in 1887 [55] and Rigollot in 1893 [56] observed that the sensitivity of the electrodes increased when coated with a dye material. Review articles by Copeland and co-workers [57]; T. Kuwana [58]; M. D. Archer [59] and A. K. Jana [60] throw more light on the journey of DSSCs.

In 1968 H. Gerischer et al. [61], using experimental data, proposed a theoretical model to explain the mechanism of dye-sensitization on n-type ZnO and p-type perylene for the production of photocurrent. Then in 1971 H. Tributsch et al. [62] demonstrated for the first time the conversion of photon energy to electric current via electrochemical reactions of chlorophyll molecules on single-crystal ZnO, similar to photosynthesis, with efficient charge separation. Further research works were carried out with ZnO and TiO_2, especially in relation to the famous publication of A. Fujishima et al. [63] on TiO_2, using it to split water into H_2 and O_2.

Table 1.1: A summary of key events in the history of the DSSC.

Year	J_{sc} /mA cm^{-2}	V_{oc} /V	*FF*	PCE /%	Key materials [ECM/dye/HTM/CE]	Ref.	Comments
1839					AgCl- or AgBr-Pt/$H^+_{(aq)}$/Pt	[4]	Discovery of PV effect.
1883	-	-	-	-	Metal/molten Se/Au	[100]	Great potential of PV.
1887	-	0.25	-	-	I- or Br-Ag/Erythrosine/Ag	[5]	Enhanced photocurrent generation by employing dyes.
1971	1 x 10^{-7} @ 670 nm	0.5	-	-	ZnO/Chlorophyl/KCl-hydroquinone/Pt	[12]	1st photon energy to current energy conversion.
1980	-	-	-	2.5 @ 562 nm	Al_2O_3-doped ZnO/Rose Bengal/KI-I_2/Pt	[14]	1st use of porous electrode DSSC.
1991	11.33	0.681	0.684	7.1	TiO_2/Ru-complex/I^-:I_3^- /Pt	[15]	Unprecedented high PCE - invention of the Gratzel cell.
2001	6.8	0.67	0.46	2.2	TiO_2/Z316/ [Co(dbbip)$_2$]$^{2+/3+}$/Pt	[103]	Introduction of I^-:I_3^--free 1-electron Co-based HTM DSSC.
2005	3.2	0.79	0.55	1.4	TiO_2/Ru-complex/[Cu(dmp)$_2$]$^{1+/2+}$/Pt	[104]	Introduction of Cu-based HTM DSSC.
2006	11.9	0.66	0.68	5.1	TiO_2/D5/I^-:I_3^-/Pt	[101]	Pioneer work on the design of n-type D-*π*-A dyes.
2009	11.0	0.61	0.57	3.81	TiO_2/$CH_3NH_3PbI_3$/LI:I_2/ Pt	[102]	Evolution of Perovskite solar cells from DSSC.
2015	18.27	1.014	0.771	14.3	TiO_2/ ADEKA-1 & LEG4 / [Co-(phen)$_3$]$^{3+/2+}$/Au-GNP	[17]	Record PCE DSSC so far.

NB: ECM – electron conducting material; HTM – hole transport material; CE – counter electrode

In 1980 M. S Matsumura et al. [64] obtained a power conversion efficiency (PCE) of 2.5 % using Al-doped porous ZnO with rose bengal dye; among other works with CdS and TiO_2 using anionic, cationic and zwitterion dyes.

Thus the PCEs of DSSCs were still low, basically from low dye loading with only ~ 1 % absorbed incident light, until the famous work of M. Gratzel et al. [65] in 1991 who used a 3D mesoporous nanocrystalline TiO_2 electrode to obtain an unprecedented PCE of 7.1 %.

Since, then, research in this field has spurred until the current certified record PCE of 11.9 % by Sharp [66]; uncertified record of 14.3 % by Kakiage et al. [67] and Prof. Hwan Kyu Kim of Korea University hinting, at the 1st Dyenamo DSSC conference in Uppsala 10/2017, that they will soon publish a record cell of 15 %. However, the theoretical maximum limit is 32 %, with a potential to subvert and exceed it. Moreover, an ideal 15-20 % PCE is needed to be effectively competitive commercially. Thus, the need for more (and thus, the on-going) research in the DSSC field.

1.3.1.2 Structure, components and working principle of the DSSC

The basic structure and working mechanism of the DSSC is as described in the following steps and as shown in Fig. 1.9.

a. *The transparent conducting oxide (TCO) substrate:*

this is usually made of a thin layer (≤ 1 μm) of fluorine-/indium-doped tin oxide (F/ITO) coating on a transparent glass substrate. The transparency is necessary for maximum incident light passage to reach the photoelectron generator dye; and the conductive FTO or ITO for reception of arriving photogenerated electrons and their subsequent transport to the external circuit. The best TCOs usually have sheet resistance of about 10 Ω/□, however, EXEGER, at the 1st Dyenamo DSSC conference, Uppsala 10/2017, revealed that they have developed a TCO with sheet resistance of 0.1 Ω/□, thus allowing them to fabricate cells of large active areas with minimal effect on performance.

b. *The hole blocking layer (HBL):*

this is a thin compact layer of semiconductor electron transporting material (SC ETM) on the TCO to prevent short circuiting of the cell from a contact between the TCO and the hole conducting material (HCM) electrolyte. It should be as thin as possible to reduce electron

transport resistance through it to the minimum possible, but thick enough to prevent the penetration of the HCM through it.

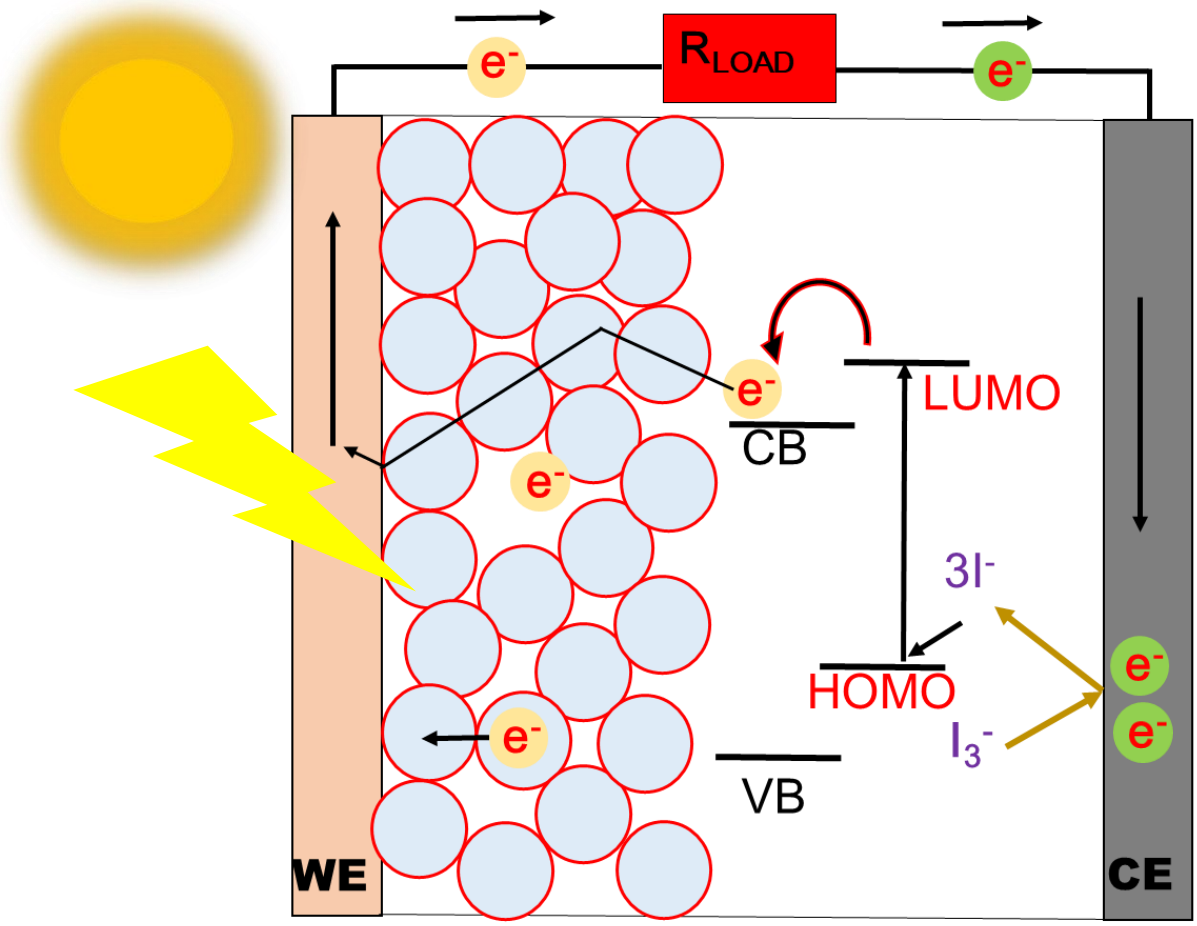

Fig. 1.9 Schematic of the structure and working principle of the *n*-type DSSC.

It can be prepared via a number of ways including, chemical bath deposition (eg sol-gel and aqueous $TiCl_4$ [68]), spin coating [69], spray pyrolysis [70], atomic layer deposition [71], electrochemical deposition [72], thermal deposition [73], pulse laser deposition [74], etc.

c. *The Photoanode:*

This is a nano/mesoporous layer of SCM that supports the dye/sensitizer, receives photogenerated electrons and transports them to the TCO substrate. The common SCMs used as ECMs include, ZnO, TiO_2, SnO_2, $SrTiO_3$, Nb_2O_5, Zn_2SnO_4, SnO_2@ZnO core-shell, WO_3,

In_2O_3, Ta_2O_5, ZrO2, etc. [75-83]; with NiO as the common *p*-type SCM for p-type DSSCs [84-86]. However, the best and most common SCM is TiO_2 with the key desirable properties of: large band gap; suitable band edge levels for charge injection and extraction; long lifetime of excited electrons; exceptional resistance to photocorrosion; non-toxicity and low cost [87-89]. Thus, further discussions on the ETM will be mainly in respect to TiO_2. The SCM can be prepared in the form of nanoparticles (NPs); nanotubes (NTs); nanorods (NRs); nanowires (NWs), etc. as shown in Fig. 1.10; or a composite or various modifications of them. The major differences between the 1D nanostructures (NTs, NRs and NWs) and the 3D NPs are that the 1 D NTs, NRs and NWs have superior electron transport efficiency due to minimal or absence of inter-grain boundaries, but suffer relatively lower surface areas. The NPs on the other hand have lower electron transport efficiency due to the presence of many grain boundaries, but have larger surface areas. However, the common and best performing DSSCs employ NPs. The ETM typically has a thickness around 10 µm and of various morphologies. In addition to conducting the photogenerated electrons, the ECM is expected to have a high surface area to be able to absorb maximum monolayer dye for maximum incident light absorbance. For efficient light harvesting (η_{LHE}), ECM structures that scatter light (which increases the mean path of light, hence its absorbance within the cell) are desirable and designed.

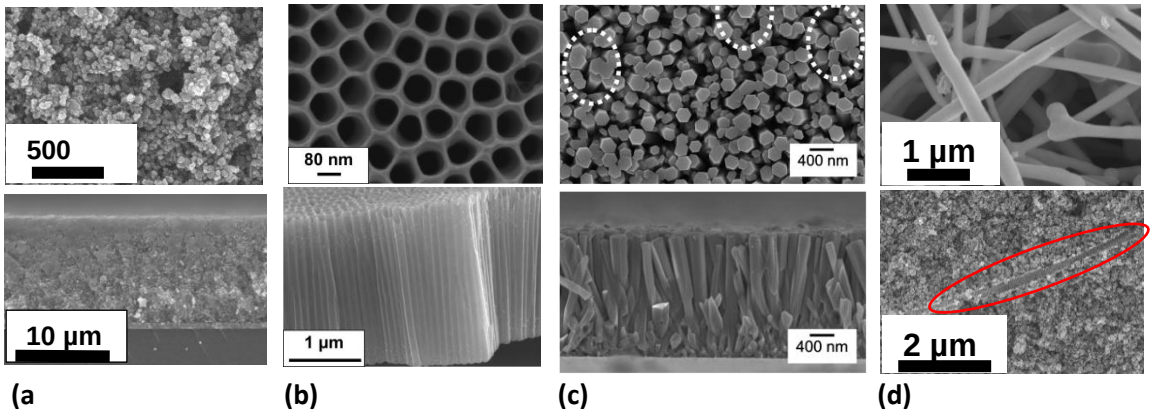

Fig. 1.10 FE-SEM images of various ECM structures for DSSC photoanodes: (a) Top: surface view of TiO_2 P25 NPs; Bottom: cross-sectional view; (b) Top: surface view of TNTs; Bottom: cross-sectional view; (c) Top: surface view of ZnO NRs; Bottom: cross-sectional view; and (d)Top: Ag@TiO_2 NWs; Bottom: Ag@TiO_2 NW located in a doped TiO_2 P25 photoanode.

Thus, various designs of the ECM include: high surface area nano/mesoporous layer; a hierarchical/scattering top layer morphology to increase light scattering and surface area; plasmonic layers which use the localized surface plasmon resonance (LSPR) effect of subwavelength NPs to increase the light absorbance of the dye; and photonic crystals-modified ECM which also increase the η_{LHE} via the control of the reflected, diffracted and refracted light through the cell. Reference [90] is a good resource for further information.

The ECM is deposited via many routes with some common techniques including:

doctor blade coating with a screen printer, spin coating, dip-coating, atomic layer deposition (ALD), electrophoretic deposition (EPD), electrochemical deposition, anodization and thermal oxidation.

1.3.1.2.1 A brief on TiO_2

TiO_2 has three natural crystalline forms: Anatase, Rutile (~ 98 %) and brookite; with brookite being the rarest of the three. Rutile is the thermodynamically most stable form at all temperatures with the metastable forms of anatase and brookite transitioning into rutile at temperatures around 500 and 750 °C, respectively, with other conditions such as pressure, reaction agents, catalysts, etc. sensitively affecting these transition temperatures. Anatase and rutile have tetragonal structure while brookite has an orthorombic structure. Anatase is preferred for DSSs because of its superior charge transport and relatively higher surface area. Anatase and rutile have different band structures, hence a mixture of them as ECM causes trapping of charge carriers and promote recombination processes. However, some studies have suggested that a little amount of rutile in anatase enhances performance [91-93]. Rutile as the ECM in DSSCs also gives a lower V_{oc} compared to anatase.

The band gap of n-type single crystal anatase is ~ 3.2 eV with a resistivity of 1015 Ω cm [94]. Its lower CB edge is made of vacant Ti^{4+} 3d bands and the upper VB edge made of filled O^{2-} p bands [95]. Bulk oxygen vacancies, Ti interstitials and reduced crystal surfaces generate shallow electron traps, enabling excess electrons that can enhance conductivity, giving TiO_2 its *n*-type SCM characteristics. However, at the same time, oxygen vacancies can also generate Ti^{3+} species that form a band about 0.5 eV below the CB of TiO_2, thus generating a deep trap states which enable charge recombination. Thus, defects can also work as charge traps causing recombination and thus, negatively affecting device performance [94, 96]. The amount of defects can be influenced by factors such as heating and UV irradiation or oxygen-depriving conditions (which are processes that cause oxygen desorption); or exposure to the atmosphere (oxygen-rich) or ozonation (which promote oxygen adsorption, resulting in passivation). Thus, these complex defect states with their consequent sub-band gap states create a complex electron transport system in TiO_2 and thus difficult to investigate. However,

theoretical and experimental evidence strongly support the notion that electrons are de-trapped from sub-band states that lie deep in the tail of density of states (DOS) into the conduction band [97-99]. This also agrees with the multiple-trapping model for charge transport [100-101].

The occupation of the sub-band gap states at energy E_A can be determined using the fermi-Dirac distribution function:

$$F(E_A\text{-}E_{Fn}) = 1/(1+e^{(E_A - E_{Fn})/K_BT}) \qquad \text{- (1.8)}$$

and the density of carriers at energy E_A (n_A) given by $n_A = N_A F_A$; N_A is the total number of trap sites. Using this, the density of electrons in the CB (n_{CB}) can be derived as a function of the quasi-Fermi level (E_{Fn}) as:

$$n_{CB} = N_{CB}\, e^{(E_A - E_{Fn})/K_BT} \qquad \text{- (1.9)}$$

and the conductivity of the film given by:

$$\sigma = n_{CB} e \mu \qquad \text{- (1.10)}$$

μ is electron mobility; given that electron conduction takes place only in the CB.

From these relations it can be deduced that conductivity increases with increase of (probability of) electrons in the CB, which in turn increases as the Fermi level moves closer to the CB. Thus, any modification that eliminates deep trap states increases conductivity of the TiO_2 ECM film.

Different studies suggest trap states are located in the bulk [98], at the inter-particle grain boundaries [102] and at the particle surfaces [103-104]. Charge recombination is an interfacial phenomenon [105], hence bulk trap states are not relevant [106]. However, it is difficult to distinguish, experimentally, between inter-particle grain boundaries trap states from interfacial trap states. The synthesis method heavily influences the type and location of

defect states, with the understanding that weakly reducing synthesis conditions and annealing at low temperatures favor the formation of oxygen vacancies; while strongly reducing conditions and high temperature annealing favor the formation of titanium interstitials as the main defects states [94, 107]. Trap states can also affect the V_{oc} of a DSSC device, since Voc can also be described as the energy difference between the quasi-Fermi level of the TiO_2 and the reduction potential of the HTM; with an increase in Voc resulting from reduction in deep trap states and a lower V_{oc} from enhanced deep trap states (lowering of quasi-Fermi level). In addition, when trap states act as recombination centers, it leads to a decrease in Jsc.

At the TiO_2-HTM interface, band bending occurs due to the formation of a space charge region (depletion layer) which provides an electric field that separates electrons and holes. The space charge region can be cancelled by an external voltage to eliminate the band bending. This specific external voltage is known as flat band potential, V_{FB} [108-109]. Because this is an interfacial phenomenon it means surface trap states can influence this VFB and thus affect effective charge separation. A negative shift in V_{FB} (upward shift of CB/Fermi level) will cause inefficient charge injection into the CB due to reduction in potential difference between the CB edge of TiO_2 and the LUMO of the dye's, leading to lower J_{sc}; and vice versa with the possible consequence of increased charge recombination.

Thus with such a complicated structure and electronic properties, electron transport in TiO_2 is quite complicated. However, a high-throughput characterization and analytical approach can reveal reliable results. In addition, since the sensitizer anchors to the TiO_2 surface, here again, it means the trap states can influence the dye adsorption depending on their distribution.

TiO_2 nanostructures for the ECM can be synthesized in many ways with some of these including, sol-gel, hydrothermal, solvothermal, anodization, micelle method, sonochemical,

microwave synthesis, etc. [108-109], mostly using titanium precursors like titanium alkoxides and titanium metal.

d. The Sensitizer/Dye:

The function of the dye is to absorb photons from the incident light to excite electrons and subsequently inject the photogenerated electrons into the CB of the *n*-type ECM. In the *p*-type SCM DSSC, holes are injected from the HOMO of the dye to the VB of the SCM. Thus, there are some essential characteristics a dye should have that include:

i. It should absorb light across the visible spectrum and if possible into the NIR region.

ii. It should be photostable, and also thermally and electrochemically stable.

iii. It should have an anchoring group(s) (RH_2PO_3, RCOOH, RCOOR, RCOCl, RCOR, etc) that should strongly bind the dye onto the charge conducting material surface.

iv. The energy of the excited LUMO level of the dye should be higher than that of the CB edge of the ECM for enough potential difference to drive efficient charge injection. While in the p-type the HOMO of the dye should be at a more positive potential than the VB of the SCM.

v. For efficient dye regeneration the oxidized state level of the photosensitizer should be more positive than the redox potential of the HCM.

vi. Dye aggregation should be avoided and this can be achieved by optimizing the molecular structure of the dye or by the use of co-adsorbers or optimizing the dyeing time period.

Thus, based on these requirements many sensitizers have been developed including metal complexes; porphyrins, pthalocyanines and metal-free organic dyes. The Ru-complex dyes have always been the best performing dyes in the order of N3 dye in the early 90s with the highest cell PCE around 10 %; black dye in the mid-90s with highest PCE of about 10.4 %

and N719 since the early 2000s with highest efficiency of about 11.2 %. However, by the early-to-mid-2000s high performing organic and porphyrin dyes had appeared on the scene with 11.5 % PCE using C259 + C239 organic dyes; and 11.9 % using YD2 + o-C8 porphyrin dyes + Y123 organic dyes. The highest PCE using porphyrin dye (SM 315) DSSC is 13.1 % and that of the organic dye (ADEKA-1 and LEG4 tandem sensitizers) is 14.3 %, which is also the record laboratory DSSC PCE. These achievements have been possible with the added advantage of the development of alternative HCMs such as the Co and Cu redox complexes to large-regeneration-driving-force (0.6 V) and corrosive iodine based HCM.

A common description of the organic dyes structure is Donor (D)-π/Linker-Acceptor (A) [D—*π*—A] structure. The donor component can be tuned to reduce dye aggregation, retard charge recombination, enhance light absorption of the dye and adjust the HOMO energy level of the dye which is related to the donor ability of the dye. The *π*-bridge or linker enhances the light absorbance efficiency of the dye, extends the major the major absorption band of the dye, maximizes light absorption and usually has a large planar *π*-conjugated system for the delocalization of charge electrons. The acceptor component, which usually contains the anchoring group of the dye, is responsible for accepting charges from the donor and injecting them into the charge conducting SCM (ECM for *n*-type DSSCs); strong anchoring of the dye to the charge conducting SCM and hence, contributes to the long term stability of the dye and by extension a contributory factor to the long term stability of the complete DSSC. It also tunes the LUMO energy level of the dye. Thus the dye exhibits intramolecular charge transfer from the donor to the π-bridge and then to the acceptor before final injection into the SCM, upon excitation. Which indicates that the acceptor component should be close to the SCM for efficient charge injection and the donor group away from it to prevent charge recombination but easily accessible to the HTM for efficient dye regeneration. However, a reverse structure is used in the *p*-type SCM/DSSC where holes are injected into the SCM and hence the

anchoring group is near or part of the donor component. The current target of *p*-type DSSCs is to increase the V_{oc} to the level of the n-type to combine them in a more efficient tandem structure DSSCs.

There are also natural sensitizers that are extracted from natural sources such as the leaves, fruits, flowers, roots, grains, husks, barks, etc of plants and algae, among others. They are classified, mainly, into carotenoids, betalains, flavonoids/chlorophylls, based on structure. Natural dyes have the main advantages of being low cost, wide absorption coefficients in visible region, abundance in nature, facile extraction and preparation, complete biodegradability and environmental friendliness. Their major disadvantages include, low PCEs around 1 % (although combinations of these dyes have given PCEs around 4 %) and unstable DSSCs/easy breakdowns. Some suggested reference papers on sensitizers include references [110-116].

e. The HCM/Electrolyte:

The HCM is responsible for receiving electrons from the CE to be reduced and in turn reduce the oxidized dye, effecting dye regeneration. It can be in the liquid or solid state. Although the solid state is preferred, mainly to prevent the evaporation and/or leakage of the solvent of the liquid state HTM. However, the best performing HTMs are in the liquid state. Another alternative is the use of ionic liquids (ILs) such as derivatives of imidazolium salts, which have negligible vapour pressure, high conductivity and low flammability, however they are viscous causing lower ionic diffusion and hence lowering J_{sc}s. Nevertheless, the discovery of binary ILs like 1-ethyl-3-methylimidazolium dicyanide and 1-propyl-3-methylimidazolium iodide seems to be subverting this challenge. The standard HTM has been the I^-/I_3^- redox couple, however, it has the severe disadvantage of loss of a significant part of the potential due to many intermediate reactions in the regeneration of the dye (high dye regeneration driving force). Hence a new class of HTMs, the colourless Co complex redox couples with

one electron reduction process and reduction potentials closer to the energy levels of the HOMO of dyes (thus, reduced dye regeneration driving force) were introduced to overcome this challenge [116-119]. A Co-complex HTM was used in the current record DSSC PCE of Kakiage et al. The latest high performance Cu-complex redox couples HTMs were developed with the main advantages of: faster dye regeneration, slow charge recombination, suitable redox potential, faster diffusion due to smaller size, earth abundant and faster electron self-exchange [120-123]. A typical performance of the three main high performance HTMs are shown in Table 1.1 [124] below:

Table 1.2: Comparison of the DSSCs performance of three HCMs

Electrolyte	J_{sc} **/mA cm^{-2}**	V_{oc} **/mV**	***FF***	η **/%**
$[Cu(dmbp)_2]^{2+/1+}$	14.4	1048	0.681	10.3
I^-/I_3^-	15.8	724	70.4	8.0
$[Co(bpy)_3]^{3+/2+}$	15.3	844	71.2	9.2

Other HCMs include Br^-/Br^{3-}; $SCN^-/(SCN)^{3-}$; SeCN-/$(SeCN)^{3-}$; and the organic TEMPO.

f. The CE:

This receives photogenerated electrons from the external circuit and use them to catalyze the reduction of the HTM. The commonest efficient CE is Pt coated on a TCO. However, with the advent of the non-corrosive HTMs the low cost and environmentally friendly carbon-based CE materials (graphite, carbon black, single-wall carbon nanotubes, multiwall carbon nanotubes, graphene, graphene oxide, etc.) have sprung up and some actually perform better than the traditional good performing Pt [125-127]. The record cell of Kakiage *et al.* employed graphene nanoplatelets (GNP).

The CE and WE are then sealed with either a hot-melt of plastic film (Surlyn® or Bynel®) or glass frits; usually between 25-50 µm to reduce internal resistance of the HTM but not too thin to cause short circuiting of the electrodes during the sealing. The cell is then filled with the HTM (especially for solid state HTMs) and the holes sealed.

1.3.1.3 Electron kinetics in an active DSSC

Figure 1.11 and the ensuing explanations show typical electron dynamics time constants in a TiO_2-N719 dye-I^-/I_3^- working DSSC cell.

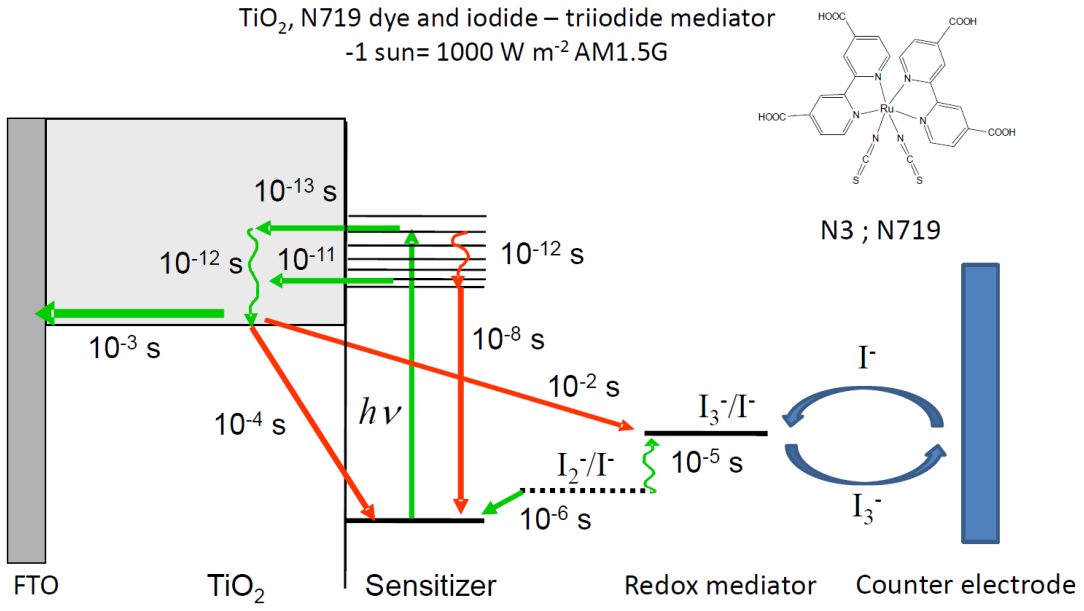

Fig. 1.11 Typical time constants in a DSSC. *[G. Boschloo, DSSC characterization methods, 1st Dyenamo conference, 2017]*.

i. Positive kinetics: charge injection from dye to CB of ECM:10^{-13} s (singlet state) and 10^{-11} s (from the triplet state); charge transport through the ECM to the TCO: 10^{-3} s; Charge

relaxation in LUMO of dye and CB of ECM:10^{-12} s; dye regeneration: 10^{-6} s; reduction of redox species: 10^{-5} s;

ii. Negative kinetics: electron-hole recombination in dye: 10^{-8} s; CB electron-HCM recombination – 10^{-2} s; CB electron-dye recombination: 10^{-4} s

Thus, it is these variant electron kinetics time constants between the positive and negative components that are responsible for the effective charge separation in DSSCs, unlike the electric field in conventional *p-n* junction solar cells.

The following are noteworthy points in the fabrication of DSSCs for efficient and stable cells:

- Use smaller cell areas (0.25 cm^2 is common)
- Avoid contamination; use dedicated equipment
- Avoid humidity which degrades dye from the surface of the ECM
- Test many cells and other repetitions to ensure repeatability
- Do extra treatments such as $TiCl_4$ (to increase surface area and charge transport) and ozonation (to reduce oxygen vacancy related negative trap states)
- Always wear gloves

A critical point to consider in the fabrication of DSSCs is that no particular component can be necessarily considered the best because DSSC is such a complex interaction of all components such that a change in one component will most often have to be optimized with all the other components to achieve high performance.

1.3.1.4 Characterization techniques for DSSCs

This section discusses the most common techniques and the information that can be obtained from the measurements [109, 128-129]:

a. Computational modelling

Computational modelling can be used to predict and design material properties. Density functional theory (DFT) is a popular method due to its low computational cost, making it possible to quickly screen dopants for their suitability to increase TiO_2 properties. However, this method often underestimates the band gap, leading to inaccurate predictions.

b. Morphological studies

The structure of TiO_2 can be studied via several techniques. Electron microscopy offers the possibility to image nanostructures; from X-ray diffraction average particle size and dopant distribution can be determined; and surface analysis quantifies the effect of doping on surface area and dye adsorption (for non-intrinsic WEs).

i. Electron microscopy

Electron microscopy makes it possible to visualize and characterize nanostructures. Scanning electron microscopy (SEM) is generally used to study the surface topography and to measure the average particle size and film thickness. The latter can also be measured by a profilometer. If equipped with an energy dispersive X-ray (EDX) spectrometer, the distribution of elements in the film can also be mapped. Transmission electron microscopy (TEM) yields a higher resolution than SEM, but requires extremely thin samples, which makes TEM less well suited for topographic investigations. Atomic resolution allows imaging of the TiO_2 lattice and typically gives a better measurement of the average crystallite size.

ii. X-ray diffraction

X-ray diffraction (XRD) is a precise method to determine the crystal structure of TiO_2. It is routinely used to determine the crystal structure and the presence of impurity phases. The Rietveld refinement method allows a more detailed analysis of XRD spectra by using a least squares fit to approximate the measured profile. This way it is possible to determine the average crystallite size, *D*, by using the Scherrer formula:

$$D = K\lambda/\beta \text{Cos } \theta \qquad \text{- (1.11)}$$

where K is a dimensionless shape factor which is dependent on the shape of the particle (0.9 for spherical particles); λ is the wavelength of the X-rays; β is the full width half-maximum (FWHM) of the peak, after subtracting the instrumental line broadening; and θ is the Bragg angle. It is important to note that β and θ are in radians, whereas the instrumental output is usually in degrees. Furthermore, the inter-planar spacing, d_{hkl}, can be calculated with Bragg's law:

$$d = \lambda/2\text{Sin } \theta \qquad \text{- (1.12)}$$

and using this interplanar spacing the lattice parameters a and c can be calculated using the Bragg formula for a tetragonal (a = b) lattice:

$$1/d^2 = (h^2 + k^2)/a^2 + l^2/c^2 \qquad \text{- (1.13)}$$

The change of the individual lattice parameters from impurities effect can be determined by calculating the distortion degree of the lattice using:

$$R = [2a\sqrt{(2/3)}]/c \qquad \text{- (1.14)}$$

Vegard's law provides an empirical method to assess the successful incorporation of a dopant. It states that there is a linear relation between the lattice distortion and the concentration of dopant. It requires that the crystal retains its lattice structure and the dopant and matrix form a solid solution.

c. Dye adsorption.

The amount of dye adsorbed on the TiO_2 surface is typically a good measure to determine how many photons will be absorbed. Dye adsorption depends on the porosity of the mesoporous TiO_2, which can be measured by gas adsorption. Gas adsorption isotherms are typically analyzed by the Brunauer–Emmett–Teller (BET) theory that yields the specific

surface area of the material or by the Barrett–Joyner–Halenda (BJH) analysis, which yields the pore size distribution. Doping however often affects the adsorption of the dye to TiO_2 (in relation to the dye affinity) implying differing the amounts of adsorbed dye for samples with the same surface area.

In a more direct measurement, the dye can be desorbed from TiO_2 using a nonreactive solvent such as a 1:1 ethanol: NaOH (1 M) solvent system or 0.1 M *tetra*-butyl ammonium hydroxide (TBAOH). By comparing the UV-Vis absorption of the extracted solvent to reference spectra, the amount of adsorbed dye can be estimated. A combination of the two methods can be used to calculate the average dye density.

d. Spectroscopic techniques

By studying the interaction between light and matter the electronic structure of the material can be determined. The band gap, presence of defect states and material composition can be found through these methods:

i. UV/Vis spectroscopy.

The main use for UV/Vis spectroscopy in DSSC is to measure sensitizer or photoanode/DSSC light absorbance; or SCM/TiO_2 doping studies to obtain the direct and indirect band gap by determining the position of the absorption band edge. Absorption and reflectance are recorded in the range of 300–800 nm. Absorption and the direct band gap E_g are related through:

$$\alpha E = C(E - E_g)^{1/2} \qquad \text{- (1.15)}$$

where α is the absorption coefficient, E the photon energy and C a proportionality constant. Sample reflectance, R, can be converted to the Kubelka–Munk function, $F(R)$, which is equivalent to the absorption coefficient in eqn (8)

$$F(R) = (1-R)^2/2R \qquad \text{- (1.16)}$$

Using a Tauc plot it is possible to extract the direct and indirect band gap. In a Tauc plot, $(F(R)E)^{1/r}$ is plotted versus E, where r = ½ for the direct band gap and r = 2 for the indirect band gap. Extrapolation of the linear part of the curve gives the band gap energy at the intercept.

ii. X-ray photoelectron spectroscopy.

In X-ray photoelectron spectroscopy (XPS) the sample is irradiated with X-rays and the number of escaping electrons and their energy are measured to gain information about the elemental composition and electronic state of the elements. For example, it is possible to quantify the amount of dopant in the sample and the Ti^{3+} to Ti^{4+} ratio.

iii. FTIR spectroscopy.

Fourier transform infrared (FTIR) spectroscopy measures optical absorption in a wide spectral range (4400–4000 cm^{-1}) and gives information about atomic bond vibrations. The intensity and position of the peaks of stretching vibrations of Ti–O–Ti and Ti–O bonds give information about the interaction between TiO_2 and the dopant since they are related to the number and strength of Ti–O bonds. By doping into interstitial sites the dopant directly decreases the number of Ti–O bonds. The size, electron affinity and valency of the dopant also influences the strength and orientation of neighbouring Ti–O bonds.

iv. Raman spectroscopy.

Raman spectroscopy is used to find rotational, vibrational and other low-frequency modes in a system. A laser beam interacts with the sample modes, resulting in an up- or down-shift of the photon energy. Each material has a distinct spectrum which allows the identification of impurity phases. Dopants alter the modes and in this way it is possible to measure the effect of the dopant on the TiO_2 crystal lattice. Raman spectroscopy is particularly useful to detect the formation of oxygen vacancies.

v. Material composition.

Several methods are able to determine the amount of dopant in TiO_2 with great precision such as EDX spectroscopy, XPS spectroscopy, mass spectroscopy or neutron activation analysis, which make use of unique ‘‘fingerprint’’ measurement spectra obtained upon sample irradiation.

e. Electromagnetic measurements

The interaction between magnetic fields and free charges in the sample makes it possible to determine the type of conduction, carrier concentration and detect trap states.

i. Hall effect measurement.

When a magnetic field is applied on a current-carrying semiconductor, the charge carriers experience a force perpendicular to the magnetic field and the current. This is called the Hall effect. And by measuring the strength of this effect the type of SCM (*p*- or *n*-type); and the carrier type and concentration can be determined.

ii. Electron paramagnetic resonance analysis.

In electron paramagnetic resonance analysis (EPR) the spins of unpaired electrons are excited by microwave radiation in a magnetic field. This makes it possible to detect trapped electrons, which are unpaired, and the corresponding trap states. The technique is similar to nuclear magnetic resonance analysis (NMR) with the exception that in NMR nuclear spins are excited.

f. (Photo-) electrochemical measurements

By simulating real world conditions the performance of the solar cell can be predicted through the determination of the photovoltaic properties such as J_{SC}, V_{OC} and *FF*. A wide range of measurements where the sample is subjected to periodic optical or electronic perturbations provide information about the concentration, diffusion length and lifetime of

electrons, CB position, density of trap states as well as transport and recombination processes. They include transient and decay measurements, electrochemical impedance spectroscopy (EIS), intensity modulated photocurrent spectroscopy (IMPS), intensity modulated photovoltage spectroscopy (IMVS) and open circuit voltage decay (OCVD).

i. Photovoltaic properties.

The power conversion efficiency of a solar cell is determined by measuring the current density as a function of applied voltage characteristics under illumination. The illumination spectrum and intensity should approximate that of the sun. To this end, a standardized light source of 100 mW cm^2 AM 1.5 solar simulator is used. From the photo current–voltage (I–V) curve J_{SC}, V_{OC} and *FF* are extracted. J_{SC} is the current in the absence of a net voltage, V_{OC} is the voltage in the absence of net current and *FF* is a measure for the ‘‘squareness’’ of the curve and is a good indication for the resistances in the device. *FF* is determined by dividing the maximum power output P_{max} of the device by (J_{SC} × V_{OC}). Parasitic resistances in the device lower *FF*; for low voltages shunt resistances are dominating, while for high voltages the series resistance is important. These are revealed by *I–V* curves measured in the dark. Under dark conditions, a solar cell behaves as an ideal diode, and deviations from the ideal diode behaviour arise from injected current leakage.

The quantum efficiency is defined as the ratio of incident photons of a certain energy to the charges collected. The external quantum efficiency (EQE) considers all the incident photons including those that are transmitted and reflected, whereas internal quantum efficiency (IQE) only takes the absorbed photons into account. From this, a correlation between the energy of the photon and the probability of charge collection can be found.

Lastly, the stability of the device can be tested by measuring the device efficiency over a long period of time.

ii. Electrochemical impedance spectroscopy.

By perturbing an applied voltage with a small sine wave modulation the impedance can be found through the sinusoidal current response. Impedance can be defined as the frequency domain ratio of the voltage with respect to the current. This ratio is in a complex number form and the resulting function can be visualised with a Nyquist plot, where the real part of the function is plotted on the x-axis and the imaginary part on the y-axis. The system can be described by an equivalent circuit consisting of parallel and series connected circuit elements. From this, charge transfer and transport processes and capacitance can be extracted.

iii. Electron transport.

Because electron transport and recombination processes respond non-linearly to different light intensities they can be studied using a small perturbation of light modulated onto a higher constant light intensity. The output can again be visualized with a Nyquist plot. In IMPS a sinusoidal modulation of light intensity is applied and the photo current is measured as a function of this modulation.

The photocurrent response τ_{pc} depends on both the electron transport and electron recombination according to, $(\tau_{pc})^{-1} = (\tau_{tr})^{-1} + (\tau_n)^{-1}$. Under short-circuit conditions, using I^-/I_3^-, electrolyte, the electron lifetime τ_n is usually much larger than the transport time τ_{tr}, implying $\tau_{pc} \asymp \tau_{tr}$.

The chemical diffusion coefficient, D_n, can be derived from the transport time

$$D_n = d^2/C\tau_{tr} \qquad \text{- (1.17)}$$

Where, d is the thickness of the TiO_2 layer and C is a constant which depends on the absorption coefficient and direction of illumination.

iv. Electron lifetime.

The measurement of the electron lifetime is similar to the electron transport, but the open circuit potential rather than the photo current is measured. Under these conditions, photo-generated electrons are not extracted and will eventually recombine with holes. Using a small intensity modulation, the response time of the potential corresponds to the electron lifetime τ_n. An alternative is the OCVD method, where V_{OC} is measured as a function of time after the light source is switched off. The electron lifetime is calculated from the slope of the transient as:

$$\tau_n = kT/e \, [dV_{OC}/dt]^{-1} \qquad \text{- (1.18)}$$

The advantage of this method is that the electron lifetime can be determined for a wide potential range in just one measurement.

A third method is time-dependent charge extraction, where the lifetime is given by

$$\tau_n = Q(t)[(dQ(t))/dt]^{-1} \qquad \text{- (1.19)}$$

$Q(t)$ is the extracted charge after decay in the dark for the time, t, assuming recombination follows first-order kinetics.

IMVS and OCVD give similar values, while charge extraction usually gives a value that is about 4 times higher. This can be explained by the fact that the former methods are based on the recombination of photo induced excess charges, whereas the latter method gives an average lifetime for all the electrons in the TiO_2.

v. Electron concentration.

The electron concentration can be measured through charge extraction methods, where the current is integrated over time after the light has been switched off. Alternatively, the capacity is measured. An open-circuit potential is established by a bias illumination after

which a light pulse is applied. The resulting voltage rise is measured, while the transient photo current is measured separately under short circuit conditions to calculate the injected charge. The capacity is given by the ratio of injected charge and voltage change. Lastly, the electron concentration can be estimated from the slope of a Mott–Schottky plot.

vi. Flat-band potential.

The flat-band potential, V_{FB}, can be derived from a Mott–Schottky plot, where the capacitance of the space charge region is measured as a function of voltage under depletion conditions. For a fit of the linear part of the curve, V_{FB} and electron density are given by the axis-intersect and the slope of the fit, respectively. The flat-band potential is usually referenced to a standardized electrode. A negative shift is indicative of an upward shift of CB, whereas a positive shift indicates a downward shift of CB.

vii. Charge collection efficiency.

The charge collection efficiency, η_{CC}, is an important parameter as it combines the results of electron transport and lifetime studies, enabling to find the ideal balance between the two. η_{CC} is given by:

$$\eta_{CC} = 1 - (\tau_{pc}/\tau_e) = 1/[1 - (\tau_{tr}/\tau_n)] \qquad \text{- (1.20)}$$

provided τ_{tr} and τ_n are measured at the same quasi-Fermi level. A similar parameter is the electron diffusion length, L:

$$L = \sqrt{(D_n\tau_n)} \qquad \text{- (1.21)}$$

which is the average diffusion distance of electrons before they recombine with holes.

1.4 Localized surface plasmon resonance (LSPR)

Sub-wavelength nano metallic structures (e.g. Ag, Au, Cu Pt and Pd) have delocalized CB electrons at their surface. These electrons are easily displaced to one section on the surface causing polarization of the nanostructure, and thus neutral particles of charged negative clouds of electrons and positive nuclei are form, referred to as plasma. The restoring coulombic force between the displaced electrons and nuclei causes the electrons to oscillate about the surface in the form of plasmons. If light of similar frequency as that of the oscillating plasmons interacts with them, then resonance occurs, creating the LSPR phenomenon, as shown in Fig. 3. The characteristics of the LSPR is affected by the size, shape, composition and environment of the metal NP.

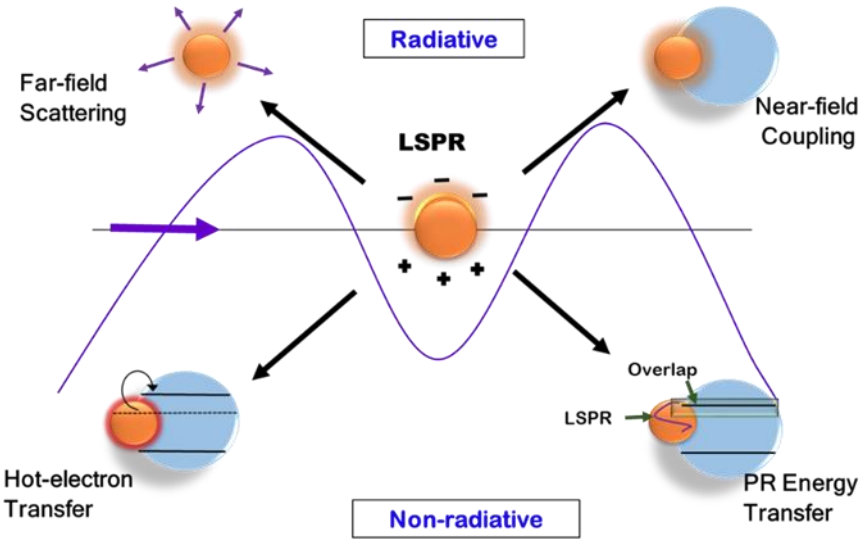

Fig. 1.12 Schematic of the LSPR phenomenon and various energy transfer mechanisms.

Since, electricity is the directional flow of charges this LSPR generates a huge electric field which can increase the DOS of vicinal materials. The DOS of materials can also be

understood as “channels” for storing and/or routing electromagnetic energy. Thus, enhancing the light trapping and tailored emission spectra of the materials [131]. In addition, the LSPR is not finite but decays over time, on the femtosecond scale [132]. When it decays, it can transfer energy in the form of photons, known as radiative transfer; or in the form of electron-hole pairs via Landau damping, known as non-radiative energy transfer [130, 133].

The radiative mechanism can be in the form of either scattering the incident, or secondary scattered light, known as far-field scattering (Fig. 3), thus increasing the path length of light within the cell and increasing its probability of being absorbed; or near-field coupling (Fig. 3) via coupling of the plasmon di-pole (or higher order-pole) with vicinal materials (especially the sensitizer) to transfer the photon energy. This second radiative mechanism gives rise to the enhanced DOS.

The non-radiative mechanism has two routes too: a) the Landau damping relaxation of the LSPR can lead to the generation of hot electron-hole pairs which can be injected to vicinal materials such as the SCM after Fermi level equilibration and with minimal separation of ~ 2 nm or less. This process is described as Hot-electron Transfer (Fig. 3); and b) via Plasmon Resonant Energy Transfer by dipole-dipole coupling with the SCM, generating electron-hole pairs below and near the SCM CB edge. Unlike in the hot-electron transfer mechanism, here, minimal separation between the plasmonic NP and SCM; band alignment and Fermi level equilibration; and the condition for a non-insulating layer around the plasmonic NP are not essential. However, the SCM should be within the near-field of the plasmonic NP and there should be a spectral overlap between the two components.

In addition, LSPR can generate surface plasmon polaritons which can cause similar effects as LSPR and also enhance light absorbance and cell performance in the NIR of the solar spectrum [128, 133-135].

All these LSPR mechanisms can occur at the same time in a single cell but with one or more dominating over the others.

References

1. K. K. Chattopadhyay and A. N. Banerjee, Introduction to nanoscience and nanotechnology, PHI Learning Private Limited, Delhi (2014).
2. R. P. Feynman, There's plenty of room at the bottom, *Eng. Sci.*, **23** (1960) 22-36.
3. N. Taniguchi, On the basic concept of 'Nano-Technology', *Proc. Intl. Conf. Prod. Eng. Tokyo, **Part II**, Japan Society of Precision Engineering*, 1974.
4. K. E. Drexler, Engines of creation, Fourth Estate, London (1990) 296.
5. T. Fischer, Materials science for engineering students, Elsevier, London, (2009) 516-525.
6. K. Koch and W. Barthlott, Superhydrophobic and superhydrophilic plant surfaces: an inspiration for biomimetic materials, *Phil. Trans. R. Soc. A*, **367** (2009) 1487–1509.
7. A. W. Adamson and A. P. Gast, Physical Chemistry of Surfaces, 6th Edt. (1997).
8. D. M. Lemal, Perspective on fluorocarbon chemistry, *J. Org. Chem.*, **69** (2004) 1–11.
9. D. O'Hagan, Understanding organofluorine chemistry - an introduction to the C–F bond, *Chem. Soc. Rev.*, **37** (2008) 308-319.
10. T. Nishino, M. Meguro, K. Nakamae, M. Matsushita and Y. Ueda, The lowest surface free energy based on $-CF_3$ alignment, *Langmuir*, **15** (1999) 4321-4323.
11. M. Ma and R.M. Hill, Superhydrophobic surfaces, *Current Opinion in Colloid & Interface Science*, **11** (2006). 193-202.
12. R. N. Wenzel, Resistance of solid surfaces to wetting by water, *Ind. Eng. Chem.*, **28** (1936) 988-994.
13. R. Cassie and S. Baxter, Wettability of porous surfaces, *Trans. Faraday Soc.*, **40** (1944) 546-551.
14. E. D. Branson, Master's Thesis, Dept. of Chemical Eng., The Univ. of New Mexico, Albuquerque, NM (2008).

15. M. Nosonovsky and B. Bhushan, Multiscale dissipative mechanisms and hierarchical surfaces: friction, superhydrophobicity, and biomimetics, Heidelberg, Germany: Springer-Verlag, (2008).
16. M. Nosonovsky and B. Bhushan, Patterned nonadhesive surfaces: superhydrophobicity and wetting regime transitions, *Langmuir*, **24** (2008) 1525-1533.
17. J. N. Israelachvili and M. L. Gee, Contact angles on chemically heterogeneous surfaces, *Langmuir*, **5** (1989) 288–289.
18. O. N. Tretinnikov, Wettability and microstructure of polymer surfaces: stereochemical and conformational aspects. In: Apparent and Mi- croscopic Contact Angles, edited by J. Drelich, J. S. Laskowski and K. L. Mittal (VSP, Utrecht 2000).
19. R. Shamai, D. Andelman, B. Berge and R. Hayes, Water, electricity, and between... On electrowetting and its applications, *Soft Matter*, **4**, (2008) 38-45.
20. M. Jarn, Q. Xu and M. Linden, Wetting Studies of Hydrophilic−Hydrophobic TiO_2@SiO_2 Nanopatterns Prepared by Photocatalytic Decomposition, *Langmuir*, **26** (2010) 11330 -11336.
21. C-K. Wu and L-J. Chen, The Pressure- and Temperature-Induced Wetting Transitions in the Binary Water + Ethylene Glycol Monoisobutyl Ether Mixture, J. *Phys. Chem. B*, **110**, 11907 – 11911 (2006).
22. E. Stratakis, A. Mateescu, M. Barberoglou, M. Vamvakaki, C. Fotakis and S. H. Anastasiadis, From superhydrophobicity and water repellency to superhydrophilicity: smart polymer-functionalized surfaces, *Chem. Commun.*, **46** (2010) 4136 - 4138.
23. B. Berge, Electrocapilarity and wetting of insulator film by water, *C. R. Acad. Sci.*, **317** (1993) 157-163.
24. F. Mugele and J-C. Baret, Electrowetting: from basics to applications, *J. Phys.: Condens. Matter*, **17** (2005) R705-R774.

25. V. Srinivasan, V. K. Pamula and R. B. Fair, Droplet-based microfluidic lab-on-a-chip for glucose detection, *Anal. Chim. Acta*, **507** (2004) 145-50.
26. M. W. J. Prins, W. J. J. Welters, J. W. Weekamp, Fluid control in multichannel structures by electrocapillary pressure, *Science*, **291** (2001) 277-280.
27. J. Zeng and T. Korsmeyer, Principles of droplet electrohydrodynamics for lab-on-a-chip, *Lab Chip*, **4** (2004) 265-277.
28. G. Lippmann, Relations entre les phénomènes électriques et capillaries, *Ann. Chim. Phys.*, **5** (1875) 494-459.
29. G. Beni and S. Hackwood, Electro-wetting displays, *Appl. Phys. Lett.*, **38** (1981) 207–209.
30. M. Vallet, M. Vallade and B. Berge, Limiting phenomena for the spreading of water on polymer films by electrowetting, *Eur. Phys. J. B*, **11** (1999) 583-591.
31. H. J. J. Verheijen, and M. W. J. Prins, Reversible electrowetting and trapping of charge: model and experiments, *Langmuir*, **15** (1999) 6616-6620.
32. B. Shapiro, H. Moon, R. L. Garrell and C. J. Kim, Equilibrium behavior of sessile drops under surface tension, applied external fields, and material variations, *J. Appl. Phys.*, **93** (2003) 5794-5811.
33. T. B. Jones, J. D. Fowler, Y. S. Chang and C. J. Kim, Frequency-based relationship of electrowetting and dielectrophoretic liquid microactuation, *Langmuir*, **19** (2003) 7646–7651.
34. A. G. Papathanasiou, and A. G. Boudouvis, Manifestation of the connection between dielectric breakdown strength and contact angle saturation in electrowetting, *Appl. Phys. Lett.*, **86** (2005) 164102-164103.
35. V. Peykov, A. Quinn and J. Ralston, Electrowetting: a model for contact-angle saturation, *Colloid Polym. Sci.*, **278** (2000) 789-793.

36. J. Buehrle, S. Herminghaus and F. Mugele, Interface profiles near three-phase contact lines in electric fields, *Phys. Rev. Lett.*, **91** (2003) 086101-086104.
37. A. Torkelli, Droplet Microfluidics on planar surface, *PhD Thesis*, Department of electrical engineering, Helsinki University of Technology, Espoo, Finland (2003).
38. R. E. Johnson and R. H. Dettre, Contact angle hysteresis: II. Contact angle measurements on rough surfaces, *Adv. Chem. Series*, **43**, (1964) 136-144.
39. M. S. Dhindsa, *Master's Thesis*, Division of Research and Advanced Studies, University of Cincinnati (2006).
40. E. Seyrat and R. A. Hayes, Amorphous fluoropolymers as insulators for reversible low-voltage electrowetting, *J. Appl. Phys.*, 90 (2001) 1383-1386.
41. J. Y. Yoon and R. L. Garrell, Preventing biomolecular adsorption in electrowetting-based biofluidic chips, *Anal. Chem.*, **75** (2003) 5097-5102.
42. A. Quinn, R. Sedev and J. Ralston, Influence of the electrical double layer in electrowetting, *J. Phys. Chem. B*, **107** (2003) 1163 - 1169.
43. T. N. Krupenkin, J. A. Taylor, E. N. Wang, P. Kolodner, M. Hodes, and T. R. Salamon, Reversible wetting−dewetting transitions on electrically tunable superhydrophobic nanostructured surfaces, *Langmuir*, **23** (2007) 9128 - 9133.
44. R. J. Vrancken, H. Kusumaatmaja, K. Hermans, A. M. Prenen, Olivier Pierre-Louis, Cees W. M. Bastiaansen and D. J. Broer, Fully Reversible Transition from Wenzel to Cassie−Baxter States on Corrugated Superhydrophobic Surfaces, *Langmuir*, 26 (2010) 3335-3341.
45. C. Quilliet and B. Berge, Investigation of effective interface potentials by electrowetting, *Europhys. Lett.*, **60**, (2002) 99-105.

46. V. Srinivasan, V. Pamula, and R. Fair, An integrated digital microfluidic lab-on-a-chip for clinical diagnostics on human physiological fluids, *Lab Chip*, **4**, (2004) 310-315.
47. M. Bienia, F. Mugele, C. Quilliet and P. Ballet, Droplets profiles and wetting transitions in electric fields, *Physica A*, **339** (2004) 72–79.
48. M. Bienia, Ph.D. Thesis, Universite Joseph Fourier Grenoble, (2005).
49. T. Roques-Carmes, R. A. Hayes, B. J. Feenstra, and L. J. M. Schlangen, Liquid behavior inside a reflective display pixel based on electrowetting, *J. Appl. Phys.*, **95**, (2004) 4389-4396.
50. A. Staicu and F. Mugele, Electrowetting-induced oil film entrapment and instability, *Phys. Rev. Lett.*, **97** (2006) 167801-167804.
51. *IEA* - Key world energy statistics, 2017.
52. N. Lewis, Toward cost-effective solar energy use, *Science*, **315** (2007) 798-801.
53. *International renewable energy agency*, **1** (2012).
54. A-E. Becquerel, Mémoire sur les effets électriques produits sous l'influence des rayons solaires, *C. R. Acad. Sci. Paris*, **9** (1839) 561–567.
55. J. Moser, Notiz fiber versti rkung photoelektrischer strSme durch optische sensibilisirung, *Mh. Chem.*, **8** (1887) 373.
56. H. Rigollot, Memoires et communications, C.R. Acad. Sci. Paris, 116 (1893) 878.
57. A. W. Copeland, O. D. Black, A. B. Garett, The photovoltaic effect, *Chem. Rev.*, **31** (1942) 177-226.
58. T. Kuwana, In electroanalytical chemistry, A. J. Bard Ed., New York; *Marcel Dekker*, **Vol. 1** (1966) 197.
59. M.D. Archer, Electrochemical aspects of solar energy conversion, *J. Appl. Electrochem.*, **5** (1975) 17-38.

60. A. K. Jana, Solar cells based on dyes, *Journal of Photochemistry and Photobiology A: Chemistry*, **132** (2000) 1–17.
61. H. Gerischer, M. E. Michel-Beyerle, F. Rebentrost and H. Tributsch, Sensitization of charge injection into semiconductors with large band gap, *Electrochim. Acta.*, **13** (1968) 1509-1515.
62. H. Tributsch and M. Calvin, Electrochemistry of excited molecules: photo-electrochemical reactions of chlorophylls, *Photochem. Photobiol.*, **14** (1971) 95-112.
63. A. Fujishima and K. Honda, Electrochemical photolysis of water at a semiconductor electrode, *Nature*, **238** (1972) 37-38.
64. M. S. Matsumura, S. Matsudaira, H. Tsubomura, M. Takata and H. Yanagida, Dye-sensitization and surface structures of semiconductor electrodes, *Ind. Eng. Chem. Prod. Res. Dev.*, **19** (1980) 415–421.
65. B. O'Regan and M. Gratzel, A low-cost, high-efficiency solar cell based on dye sensitized colloidal TiO2 films, *Nature*, **353** (1991) 737-740.
66. Best research-cell efficiencies. NREL *https://www.nrel.gov/pv/assets/images/efficiency-chart.png* (2017).
67. K. Kakiage, Y. Aoyama, T. Yano, K. Oya, J. Fujisawa and M. Hanaya, Highly-efficient dye-sensitized solar cells with collaborative sensitization by silyl-anchor and carboxy-anchor dyes, *Chem Commun (Camb)*, **51** (2015) 15894-15897.
68. P. Nbelayim, G. Kawamura, W. K. Tan, H. Muto and A. Matsuda, Systematic characterization of the effect of Ag@TiO_2 nanoparticles on the performance of plasmonic dye-sensitized solar cells, *Sci. Rep.*, **7** (2017) 15690(1-12).
69. P. Vivo, A. Ojanper, J-H. Smått, S. Sand, S. G. Hashmi, K. Kaunisto, P. Ihalainen, M. T. Masood, R. Osterbacka, P. D. Lund and H. Lemmetyinen, Influence of TiO_2

compact layer precursor on the performance of perovskite solar cells, *Organic Electronics*, **xxx** (2016) 1-7.

70. D. Xiaoyan, S. Chengwu, Z. Yanru and W. Ni, Hydrolysis preparation of the compact TiO_2 layer using metastable $TiCl_4$ isopropanol/water solution for inorganic-organic hybrid heterojunction perovskite solar cells, *J. Semicond.*, **36** (2015) 074003(1-4).
71. L. Kavan, N. Te´treault, T. Moehl and M. Gra¨tzel, Electrochemical characterization of TiO_2 blocking layers for dye-sensitized solar cells, *J. Phys. Chem. C*, **118** (2014) 16408–16418.
72. Y. Wu, X. Yang, H. Chen, K. Zhang, C. Qin, J. Liu, W. Peng, A. Islam, E. Bi, F. Ye, M. Yin, P. Zhang and L. Han, Highly compact TiO_2 layer for efficient hole-blocking in perovskite solar cells, *Appl. Phys. Express*, **7** (2014) 052301(1-4).
73. L. Kavan, B. O'Regan, A. Kay and M. Gra¨tzel, Preparation of TiO_2 (anatase) films on electrodes by anodic oxidative hydrolysis of $TiCl_3$, *J. Electroanal. Chem.*, **346** (1993) 291–307.
74. W. Ke, G. Fang, J. Wang, P. Qin, H. Tao, H. Lei, Q. Liu, X. Dai and X. Zhao, Perovskite solar cell with an efficient TiO_2 compact film, *ACS Appl. Mater. Interfaces*, **6** (2014) 15959–15965.
75. W. K. Tan, Z. Lockman, K. Abdul Razak, G. Kawamura, H. Muto and A. Matsuda, Enhanced dye-sensitized solar cells performance of ZnO nanorod arrays grown by low-temperature hydrothermal reaction, *Int. J. Energy Res.*, **37** (2013) 1992-2000.
76. S. Lee, J. H. Noh, H. S. Han, D. K. Yim, D. H. Kim, J.-K. Lee, J. Y. Kim, H. S. Jung and K. S. Hong, Nb-doped TiO_2: a new compact layer material for TiO2 dye-sensitized solar cells, *J. Phys. Chem. C*, **113** (2009) 6878–6882.

77. W. K. Tan, Z. Lockman, K. Abdul Razak, G. Kawamura, H. Muto and A. Matsuda, Enhanced dye-sensitized solar cells performance of ZnO nanorod arrays grown by low-temperature hydrothermal reaction, *Int. J. Energy Res.*, **37** (2013) 1992-2000.
78. Y. Qiu, W. Chen and S. Yang, Facile hydrothermal preparation of hierarchically assembled, porous single-crystalline ZnO nanoplates and their application in dye-sensitized solar cells, *J. Mater. Chem.*, **20** (2010) 1001–1006.
79. S. H. Ko, D. Lee, H. W. Kang, K. H. Nam, J. Y. Yeo, S. J. Hong, C. P. Grigoropoulos and H. J. Sung, Nanoforest of hydrothermally grown hierarchical ZnO nanowires for a high efficiency dye-sensitized solar cell, *Nano Lett.*, **11** (2011) 666–671.
80. A. Kay and M. Gra¨tzel, Dye-sensitized core−shell nanocrystals: improved efficiency of mesoporous tin oxide electrodes coated with a thin layer of an insulating oxide, *Chem. Mater.*, **14** (2002) 2930–2935.
81. B. O’ Regan and D. T. Schwartz, Efficient dye-sensitized charge separation in a wide‐band gap *p-n* heterojunction, *J. Appl. Phys.*, **80** (1996) 4749-4754.
82. W. T. Hamann, R. A. Jensen, A. B. F. Martinson, H. Van Ryswyk and J. T. Hupp, Advancing beyond current generation dye-sensitized solar cells, *Energy EnViron. Sci.*, **1** (2008) 66-78.
83. M. Pagliaro, G. Palmisano, R. Ciriminna, and V. Loddo, Nanochemistry aspects of titania in dye-sensitized solar cells, *Energy EnViron. Sci.*, **2** (2009) 838-844.
84. Y. Farré, M. Raissi, A. Fihey, Y. Pellegrin, E. Blart, D. Jacquemin and F. Odobel, A Blue diketopyrrolopyrrole sensitizer with high efficiency in nickel-oxide-based dye-sensitized Solar Cells, *ChemSusChem, 10* (2017) 2618-2625.
85. N. Marinakis, M. Willgert, E. C. Constable and C. E. Housecroft, Optimization of performance and long-term stability of p-type dye-sensitized solar cells with a

cycloruthenated dye through electrolyte solvent tuning, *Sustainable Energy Fuels*, **1** (2017) 626-635.

86. R. Brisse, R. Faddoul, T. Bourgeteau, D. Tondelier, J. Leroy, S. Campidelli, T. Berthelot, B. Geffroy, and B. Jousselme, Inkjet printing NiO-Based p-type dye-sensitized solar cells, *ACS Appl. Mater. Interfaces*, **9** (2017) 2369–2377.
87. R. Jose, V. Thavasi and S. Ramakrishna, Metal oxides for dye-sensitized solar cells, *J. Am. Ceram. Soc.*, **92** (2009) 289-301.
88. D. Leung, X. Fu, C. Wang, M. Ni, M. Leung, X. Wang and X. Fu, Hydrogen production over titania-based photocatalysts, *ChemSusChem*, **3** (2010) 681–694.
89. M. Rauf, M. Meetani and S. Hisaindee, An overview on the photocatalytic degradation of azo dyes in the presence of TiO2 doped with selective transition metals, *Desalination*, **276** (2011) 13–27.
90. M. S. Ahmada, A.K. Pandeya,, N. Abd Rahima, Advancements in the development of TiO_2 photoanodes and its fabrication methods for dye sensitized solar cell (DSSC) applications. A review, *Renewable and Sustainable Energy Reviews*, **77** (2017) 89–108
91. H. Park, Y. Park, W. Kim and W. Choi, Surface modification of TiO_2 photocatalyst for environmental applications, *J. Photochem. Photobiol. C*, **15** (2013) 1–20.
92. G. Li, C. P. Richter, R. L. Milot, L. Cai, C. A. Schmuttenmaer, R. H. Crabtree, G. W. Brudvig and V. S. Batista, Synergistic effect between anatase and rutile TiO_2 nanoparticles in dye-sensitized solar cells, *Dalton Trans.*, **45** (2009) 10078–10085.
93. B.-M. Kim, S.-G.Rho and C.-H. Kang, Effects of TiO2 structures in dye-sensitized solar cell, *J. Nanosci. Nanotechnol.*, **11** (2011) 1515–1517.
94. D. O. Scanlon, C. W. Dunnill, J. Buckeridge, S. A. Shevlin, A. J. Logsdail, S. M. Woodley, C. R. A. Catlow, M. J. Powell, R. G. Palgrave, I. P. Parkin, G. W. Watson,

T. W. Keal, P. Sherwood, A. Walsh and A. A. Sokol, Band alignment of rutile and anatase TiO_2, *Nat. Mater.*, **12** (2013) 798–801.

95. H. Ardakani, Electrical and optical properties of in situ “hydrogen-reduced” titanium dioxide thin films deposited by pulsed excimer laser ablation, *Thin Solid Films*, **248** (1994) 234–239.
96. R. Asahi, Y. Taga, W. Mannstadt and A. Freeman, Electronic and optical properties of anatase TiO_2, *Phys. Rev. B: Condens. Matter Mater. Phys.*, **61** (2000) 7459–7465.
97. A. Paxton and L. Thien-Nga, Electronic structure of reduced titanium dioxide, *Phys. Rev. B: Condens. Matter Mater. Phys.*, **57** (1998) 1579–1584.
98. J. Nelson, Continuous-time random-walk model of electron transport in nanocrystalline TiO2 electrodes, *Phys. Rev.*, B, **59** (1999) 15374-15380.
99. J. Bisquert, Chemical diffusion coefficient of electrons in nanostructured semiconductor electrodes and dye-sensitized solar cells, *J. Phys. Chem. B*, **108** (2004) 2323-2332.
100. L. Dloczik, O. Ileperume, I. Lauermann, L. M. Peter, E. A. Pono-marev, G. Redmond, N. J. Shaw and I. Uhlendorf, Dynamic response of dye-sensitized nanocrystalline solar cells: characterization by intensity-modulated photocurrent spectroscopy, *J. Phys. Chem. B*, **101** (1997) 10281–10289.
101. J. Orenstein and M. Kastner, Photocurrent Transient Spectroscopy: Measurement of the Density of Localized States in a -As_2Se_3, *Phys. Rev. Lett.*, **46** (1981) 1421-1424.
102. T. Tiedje and A. Rose, A physical interpretation of dispersive transport in disordered semiconductors, *Solid State Commun.*, **37** (1981) 49-52.
103. M. Adachi, Y. Murata, J. Takao, J. Jiu, M. Sakamoto and F. Wang, Highly efficient dye-sensitized solar cells with a titania thin-film electrode composed of a network

structure of single-crystal-like tio2 nanowires made by the “oriented attachment” mechanism, *J. Am. Chem. Soc.*, **126** (2004) 14943–14949.

104. G. Schlichtho¨rl, N. G. Park and A. J. Frank, Evaluation of the charge-collection efficiency of dye-sensitized nanocrystalline TiO_2 solar cells, *J. Phys. Chem. B*, **103** (199) 782–791.
105. G. Franco, J. Gehring, L. M. Peter, E. A. Ponomarev and I. Uhlendorf, Frequency-resolved optical detection of photoinjected electrons in dye-sensitized nanocrystalline photovoltaic cells, *J. Phys. Chem. B*, **103** (1999) 692–698.
106. J. Bisquert and V. S. Vikhrenko, Interpretation of the time constants measured by kinetic techniques in nanostructured semiconductor electrodes and dye-sensitized solar cells, *J. Phys. Chem. B*, **108** (2004) 2313–2322.
107. N. Kopidakis, N. R. Neale, K. Zhu, J. van de Lagemaat and A. J. Frank, Spatial location of transport-limiting traps in TiO2 nanoparticle films in dye-sensitized solar cells, *Appl. Phys. Lett.*, **87** (2005) 202106.
108. X. Chen and S. S. Mao, Titanium dioxide nanomaterials: synthesis, properties, modifications and applications, *Chem. Rev.*, **107** (2007) 2891–2959.
109. B. Roose, S. Pathak and U. Steiner, Doping of TiO_2 for sensitized solar cells, *Chem. Soc. Rev.*, **44** (2015) 8326-8349.
110. M. Gratzel, Photoelectrochemical cells, *Nature*, **414** (2001) 338-344.
111. A. Hagfeldt, G. Boschloo, L. Sun, L. Kloo and H. Pettersson, Dye-sensitized solar cells, *Chem. Rev.*, **110** (2010) 6595–6663.
112. P. Qin *et al.*, Design of an organic chromophore for p-type dye-sensitized solar cells, *J. Am. Chem. Soc.*, **130** (2008) 8570-1871.

113. P. Qin et al, High incident photon-to-current conversion efficiency of p-type dye-sensitized solar cells based on NiO and organic chromophores, *Adv. Mater.*, **21** (2009) 2993-2996.

114. N.T.R.N. Kumara, A. Limb, C. M. Lim, M. I. Petra and P. Ekanayake, Recent progress and utilization of natural pigments in dye sensitized solar cells: A review, *Renewable and Sustainable Energy Reviews*, **78** (2017) 301-317.

115. N. Santhanamoorthi, C.-M. Lo and J.-C. Jiang, Molecular Design of Porphyrins for Dye-Sensitized Solar Cells: A DFT/TDDFT Study, *J. Phys. Chem. Lett.*, **4** (2013) 524−530.

116. M. Freitag, J. Teuscher, Y. Saygili, X. Zhang, F. Giordano, P. Liska, J. Hua, S. M. Zakeeruddin, J.-E. Moser, M. Grätzel and A. Hagfeldt, Dye-sensitized solar cells for efficient power generation under ambient lighting, *Nature Photonics*, **11** (2017) 372-378.

117. J. Hua, S. M. Zakeeruddin, J.-E. Moser, M. Grätzel and A. Hagfeldt, Dye-sensitized solar cells for efficient power generation under ambient lighting, *Nature Photonics*, **11** (2017) 372-379.

118. S. M. Fedlt, E. A. Gibson, E. Gabrielsson, L. Sun, G. Boschloo and A. Hagfedlt, Design of organic dyes and cobalt polypyidine redox mediators for high-efficiency dye-sensitized solar cells, *J. Am. Chem. Soc.*, **132** (2010) 16714-16724.

119. S. Yanagida, Y. Yu, and K. Manseki, Iodine/Iodide-free dye-sensitized solar cells, *Accounts of chemical research*, **42** (2009) 1827-1838.

120. G. Boschloo and A. Hagfeldt, Characteristics of the Iodide/triiodide redox mediator in dye-sensitized solar cells, *Accounts of chemical research*, **42** (2009) 1819-1826.

121. S. Hattori, Y. Wada, S. Yanagida and S. Fukuzumi, Blue copper model complexes with distorted tetragonal geometry acting as effective electron-transfer mediators in dye-sensitized solar cells, *J. Am. Chem. Soc.*, **127** (2005) 9648-9654.

122. Y. bai, Q. Yu, N. Cai, Y. Wang, M. Zhang and P. Wang, High-efficiency organic dye-sensitized mesoscopic solar cells with a copper redox shuttle, *Chem. Commun.*, **47** (2011) 4376-4378.

123. J. Cong, D. Kinschel, Q. Daniel, M. Safdari, E. Gabrielsson, H. Chen, P. H. Svensson, L. Sun and L. Kloo, Bis(1,1-bis(2-pyridyl)ethane) copper(I/II) as an efficient redox couple for liquid dye-sensitized solar cells, *J. Mater. Chem. A*, **4** (2016) 14550–14554.

124. M. Frietag, Q. Daniel, M. Pazoki, K. Sveinbjornsson, J. Zhang, L. Sun, A. Hagfeldt and G. Boschloo, High-efficiency dye-sensitized solar cells with molecular copper phenanthroline as a solid hole conductor, *Energy Environ. Sci.*, **8** (2015) 2634-2637.

125. J. Li, X. Yang, Z. Yu, G.G. Gurzadyan, M. Cheng, F. Zhang, J. Cong, W. Wang, H. Wang, X. Li, L. Kloo, M. Wang and L. Sun, Efficient dye-sensitized solar cells with [copper(6,6′ -dimethyl-2,2′ -bipyridine)$_2$]$^{2+/1+}$ redox shuttle, *RSC Adv.*, **7** (2017) 4611-4615.

126. M. J. Ju, J. C. Kim, H. J. Choi, S. G. Kim, K. Lim, J. Ko, J. J. Lee, I. Y. Jeon, J. B. Baek and H. K. Kim, N-doped graphene nanoplatelets as superior metal-free counter electrodes for organic dye-sensitized solar cells, *ACS Nano*, **7** (2013) 5243-5250.

127. M. J. Ju, I. Y. Jeon, J. C. Kim, K. Lim, H. J. Choi, S. M. Jung, I. T. Choi, Y. K. Eom, Y. J. Kwon, J. Ko, J. J. Lee, H. K. Kim and J. B. Baek, Graphene nanoplatelets doped with N at its edges as metal-free cathodes for organic dye-sensitized solar cells, *Adv. Mater.*, **26** (2014) 3055-3062.

128. Y. H. Jang, Y. J. Jang, S. Kim, L. N. Quan, K. Chung and D. H. Kim, Plasmonic solar cells: from rational design to mechanism overview, *Chem. Rev.*, **116** (2016) 14982-15034.

129. X.-D. Gao, X.-M. Li, & X.-Y. Gan, Enhancing the light harvesting capacity of the photoanode films in dye-sensitized solar cells. *InTech doi https://doi.org/10.5772/51633* (2013)169–202.

130. W. R. Erwin, H. F. Zaricka, E. M. Talbert & R. Bardhan, Light trapping in mesoporous solar cells with plasmonic nanostructures, *Energy Environ. Sci.*, **9** (2016) 1577–1601.

131. S. V. Boriskina, H. Ghasemi & G. Chen, Plasmonic materials for energy: From physics to applications, *Materials Today*, **16** (2013) 375–386.

132. K. Ueno, T. Oshikiri, Q. Sun, X. Shi and H. Misawa, Solid-state plasmonic solar cells, Chem. Rev., *DOI: 10.1021/acs.chemrev.7b00235* (2017).

133. X.-C. Ma, Y. Dai, L. Yu and B.-B. Huang, Energy transfer in plasmonic photocatalytic composites, *Light: Science & Applications*, **5** (2016) 1-13.

134. V. E. Ferry, L. A. Sweatlock, D. Pacifici and H. A. Atwater, Plasmonic nanostructure design for efficient light coupling into solar cells, *Nano Lett.*, **8** (2008) 43914397.

135. I. K. Ding, J. Zhu, W. Cai, S.-J. Moon, N. Cai, P. Wang, S. M. Zakeeruddin, M. Gratzel, M. L. Brongersma, Y. Cui and M. D. McGehee, Plasmonic dye-sensitized solar cells, *Adv. Energy Mater.*, **1** (2011) 52-57.

136. C. E. Fritts, "On a New Form of Selenium Photocell", *American J. of Science*, **26** (1883) 465.

137.H. Nusbaumer, J.-E. Moser, S. M. Zakeeruddin, M. K. Nazeeruddin and M. Gratzel, CoII(dbbip)22+ Complex Rivals Tri-iodide/Iodide Redox Mediator in Dye-Sensitized Photovoltaic Cells, *J. Phys. Chem. B*, **105** (2001) 10461-10464.

138.S. Hattori, Y. Wada, S. Yanagida and S. Fukuzumi, Blue copper model complexes with distorted tetragonal geometry acting as effective electron-transfer mediators in dye-sensitized solar cells, *J. Am. Chem. Soc.*, **127** (2005) 9648-9654.

139.D. P. Hagberg, T. Edvinsson, T. Marinado, G. Boschloo, A. Hagfeldt and L. Sun, A novel rganic chromophore for dye-sensitized nanostructured solar cells, *Chem. Commun.*, **0** (2006) 2245–2247.

140.A. Kojima, K. Teshima, Y. Shirai, and T. Miyasaka, Organometal halide perovskites as visible-light sensitizers for photovoltaic cells solar, *J. Am. Chem. Soc.*, **131** (2009) 6050–6051.

Chapter 2

Preparation of thermally and chemically robust superhydrophobic coating from liquid phase deposition and low voltage reversible electrowetting

2.1 Introduction

Wetting is the ability of a liquid to maintain contact with a solid surface, when brought together. The phenomena of surface wetting and surface wetting tuning are of high interest in both academic and commercial application fields [1, 2]. Applications of superhydrophobic surfaces (SHSs) include self-cleaning surfaces [3] and separation of liquid mixtures [4]. In the area of surface wetting tuning or electrowetting on dielectric (EWOD), they have applications in: digital microfluidics; liquid lens; micro-electricity generators and pixel units for electronic display units like TV sets, computers and e-paper; with typical actuation voltages in the range of 50–200 V [1, 2, 5–9].

2.1.1 Quantitative wetting

Wetting is quantified by contact angle (CA), Θ, given by the Young equation, eqn. (2.1), derived by the balance of interfacial energies around a liquid droplet on an ideal smooth surface:

$$\gamma_{LA}\text{Cos}\Theta = \gamma_{SA} - \gamma_{SL} \qquad \text{— (2.1)}$$

where, γ_{LA}, γ_{SA} and γ_{SL} are the liquid-air (or surrounding environment), solid-air and solid-liquid interfacial free energies per unit area, respectively.

Conventionally, the wetting states of surfaces are classified into: *superhydrophilic*, *hydrophilic*, *hydrophobic* and *superhydrophobic*, when Θ is $< 10°$; $10° < \Theta < 90°$; $90° < \Theta < 150°$; and $\Theta > 150°$, respectively [11]. A non-wetting solid surface (i.e., $\Theta \geq 90°$) is normally obtained by coating it with a low surface free energy material,

however, the maximum CA attained by this approach on a smooth surface is 119° [11]. Thus, obtaining a SHS involves a different approach of a combination of an appropriate surface roughness and low surface energy topography. For such surfaces, two models have been proposed for the quantification of the CA:

(1) the Wenzel model with CA, Θ_W, given by,

$$\mathrm{Cos}\Theta_W = r(\gamma_{SA} - \gamma_{SL}) / \gamma_{LA} = r\mathrm{Cos}\Theta \qquad \text{— (2.2)}$$

r = (actual area of the rough surface) / (the projected area of the surface); thus r is > 1.

This model proposes that the droplet fills the spaces of the rough structures and forms a homogeneous wetting of the surface [12]; and

(2) the Cassie-Baxter model, with CA, Θ_C, given by eqn. (2.3),

$$\mathrm{Cos}\Theta_C = f\mathrm{Cos}\Theta + (1\text{-}f)\mathrm{Cos}\Theta_f = f(\mathrm{Cos}\Theta + 1) - 1 \qquad \text{— (2.3)}$$

Where f is the fraction of the solid surface area in contact with the droplet, i.e. $f < 1$.

The component *(1-f)* is the fraction of fluid medium within the rough structures on which the droplet sits; and Θ_f is the CA between the droplet and the fluid medium (for a fluid medium of air, Θ_f = 180 °, which gives the third component of eq. 3]. This model has been proposed, with the assumption that the droplet sits on top of a composite of rough structures and fluid medium to form a meta-stable wetting state [13].

2.1.2 Electrowetting

Electrowetting (EW) [14] or EWOD [2, 15, 16], refers to the application of electric voltage to change the wettability of a polar or conductive droplet on a surface.

There are three major approaches to describing the EW phenomenon: classical thermodynamics, energy minimization, and electromechanical [1]. Jean Berthier [17],

explaining from the electromechanical view point, writes that, in the presence of a DC or AC electric field, electric charges gather at the interfaces between the conductive and dielectric components of the set-up. The same electric field that induces these charges then couples with the interfacial charges to exert an interfacial force, and if the interface is deformable (such as the interface of a liquid and its gaseous surrounding), this force can distort the interface, thus, causing EW. These induced interfacial electric forces are especially strong on the liquid-gas interface at the vicinity of the triple contact line points (where the three adjacent phases (the droplet, the surrounding medium and the substrate) meet), due to the sharp wedges present at these points.

By the energy minimization approach, a built up electrostatic capacitive field destabilizes the Young's equilibrium forces acting on a droplet and the liquid droplet adjusts itself to restore a new balance. Based on this understanding, Berge [15] added an electrostatic capacitive energy component to the Young equation to obtain the basic EW equation, the Lippmann-Young equation, eqn. (2.4), for EWOD:

$$\mathrm{Cos}\Theta_v = \mathrm{Cos}\Theta + \varepsilon_o\varepsilon_r V^2 / 2d\gamma_{LA} \qquad \text{— (2.4)}$$

Θ_v is the CA after voltage application; Θ is the Young's CA; $\boldsymbol{\varepsilon_o}$ is the permittivity of free space; $\boldsymbol{\varepsilon_r}$ is the dielectric constant of the insulating material; V is the applied voltage; d is the thickness of the dielectric component.

Equation (2.4) is found to hold true until a threshold voltage, called CA saturation, beyond which CA does not change, but leads to dielectric material break down [5]. This observation has been reported in many research results [18-23].

Equation (2.4) is for smooth surfaces. Torkelli [24] modified it for SHSs to obtain eqn. 2.5:

$$\mathrm{Cos}\Theta_v = \mathrm{Cos}\Theta_c + \varepsilon_o\varepsilon_r f V^2 / 2d\gamma_{LA} \qquad \text{— (2.5)}$$

Where, f is the fraction of solid surface in contact with the liquid droplet.

Equations (2.4 and 2.5) suggest that when the voltage supply is turned off the wetted droplet should reverse back to its original state. However many research results show that EW in an air medium is usually irreversible. This has been explained to be due to both physical and chemical surface heterogeneity. Krupenkin et al. [25] explained that, during the electrowetting process, a sizable energy is dissipated for the system to attain a new minimum energy equilibrium state and part of this energy is consumed to pin the droplet to the surface supporting it. Thus, preventing spontaneous reversibility when the voltage supply is removed. Halim et al. [26] reported that a solid-gas-liquid composite interface is replaced with a solid-liquid interface, i.e. indirectly inferring to dissipation of energy to form the new solid-liquid interface state.

Based on the above understanding, there are three proposed approaches to attaining reversible electrowetting (REW): a) engineering roughening nanostructures, such as to minimize the energy dissipation in order to eliminate the energy barrier for transitioning back to the original state [26]; b) providing energy to the system to replace the dissipated energy [25]; and c) competitive two liquid wetting approach; where one liquid provides a lubricating effect to prevent the other from being pinned to the solid surface during EW. In our work we have used the competitive two liquid wetting approach.

2.1.3 Research motivation and hypothesis

In the field of SHSs and EWD, two of the major desires are, obtaining robust surfaces, and low actuation voltage, respectively.

For chemical modification to achieve SHSs, low surface energy organic polymers are commonly used. Materials with C-F bonds are the most effective for lowering the surface free energy because the F atom has the highest electronegativity and forms a stable covalent

bond with carbon. Hare et al. [27] reported that the surface free energy increases when fluorine is replaced by other elements such as H and C, in the order, $–CF_3$<$–CF_2H$<$–CF_2–$<$–CH_3$<$–CH_2$. Therefore, fluorocarbon polymers make excellent hydrophobic films and coatings; however, the adhesion between the substrate and the fluorine-based hydrophobic coating is via van der Waals forces and, thus, relatively weak [28]. Hence, we anticipated that Nafion®, with –CF, $–CF_2$ and $–CF_3$ groups (for low surface energy) and a sulfonyl group ($–SO_3^-$), will form a good hydrophobizing coating with strong ionic bonds to the pseudoboehmite substrate's reactive hydroxyl groups, with some preliminary treatment, to give a robust SHS.

For low actuation voltage for EW, silicon dioxide and parylene C are the commonly used dielectric materials used [29, 30]: with examples of 60 – 70 V actuation voltages for 60 nm Teflon low surface energy coating on 800 nm parylene C [31, 32]; and 25 V for a 20 nm Teflon coating on 100 nm silicon dioxide [30]. Ultrathin coatings have been avoided because they are more susceptible to electrical breakdown and have poor reliability [33]. Recently M. F. Samad et al. [3] have demonstrated an actuation voltage of 14.8 V, using a dielectric layer of polyvinylidene difluoride (PVDF) (1 μm) and a very thin layer (50 nm) of Teflon as the hydrophobizing coating.

In this chapter, we have used ~ 300 nm of Au-rough alumina pseudoboehmite-FAS (fluoroalkyl silane; 1H, 1H, 2H, 2H-perfluorodecyltrimethoxysilane), coating to obtain a very low actuation voltage of 3 V, without dielectric material breakdown. In addition, we have employed facile and low-cost techniques such as sol-gel coating, hot-water treatment (HWT) and layer-by-layer (LBL) coating, unlike commonly used complex and expensive techniques like chemical vapor deposition, lithography, electrospinning, and specialty coating equipment [34, 35].

2.2 Experimental details

2.2.1 Al_2O_3 sol preparation

The alumina sol preparation was adopted from Tadanaga et al. [36] as follows: typically, 6.0 g of aluminium *s*-butoxide (Al(O-*sec*-Bu)$_3$) [Wako, 324-22475] was mixed with 10.98 g of iso-propyl alcohol (IPA) [Wako®, min. 99.5 %] and stirred at room temperature for 10 min at 700 rpm. A 4.76 g of ethyl acetoacetate (EAcAc) [Wako®, min. 98.0 %] in 5.49 g IPA was added, as a chelating agent, with continuous stirring for 1 h. Finally, 0.88 g of water [from AQUARIUS Equipment: RFD 230NA, ADVANTEC; ~ 0.07 μS] diluted in 5.49 g IPA, was added for hydrolysis with continued stirring for another 2 h to obtain the final sol. A sol of molar ratio of 15, 1.5 and 2 of IPA, EAcAc and H_2O to Al(o-sec-Bu)$_3$) , respectively, was obtained. The reagents used were all of analytical grade.

2.2.2 Soda-lime glass coating and hot-water treatment

A soda-lime glass substrate [MATSUNAMI Micro slide glass S1112; size = 38 x 26 mm; thickness = 1.0 ~ 1.2 mm] was cleaned by two rounds of 10 min ultrasonication in water and a final round with IPA. One face of the glass substrate was masked with a scotch tape and dip-coated with the sol at a withdrawing speed of 1 mm/s, using a sol-gel coater [Aiden Dip Coater]. This was dried on a hot plate at 100 °C for 10 min, and then heat treated in a furnace at 500 °C for 1 h. The calcined film was hot-water treated at 92 °C for 1 h on a Teflon support in a beaker of water to form pseudo-crystallized rough alumina structures. The sample was heat-treated again at 500 °C to consolidate the formation of the pseudo-crystallized rough structures, pseudoboehmite.

2.2.3 Hydrophobization via LBL coating

The low surface energy material, Nafion® [ALDRICH®, Nafion® perfluorinated ion-exchange resin, 5 wt.% solution in lower aliphatic alcohols/H_2O mix; contains 15 – 20 % H_2O], was

coated on the rough alumina pseudoboehmite structures via a single round of LBL coating. This was achieved by first soaking the sample in a solution of Poly(diallyl di-methylammonium chloride) (PDDA) [ALDRICH®; High molecular, weight 20 wt% in water; Mw = 400,000 – 500,000] (1 mg ml^{-1} in 0.5 mol L^{-1} NaCl) for 10 min, rinsed with distilled water, blow-dried with $N_{2(g)}$ and heat-dried with a blow dryer. The films were then soaked in a solution of Nafion® chains (1 mg ml^{-1} in a 9 : 1; methanol : water solvent system) for 10 min. The sample was again rinsed with water, blow-dried with $N_{2(g)}$. It was finally dried in an oven at 100 °C for 1 h, to obtain the SHS.

2.2.4 Sample preparation for electrowetting

The sample for EW was similarly prepared as for the SHS sample in section 2.2.2 with three changes: a) an initial Au conductive layer coating before the Al_2O_3 sol coating; b) a reduced Al_2O_3 coating heat treatment temperature to 120 °C to protect the Au conductive film which aggregates into a non-conductive particulate-clusters layer at ≥ 150 °C; and c) replacement of Nafion® with 1H, 1H, 2H, 2H-perfluorodecyltrimethoxysilane (FAS) [ALDRICH; 97 %], because Nafion® coated SHS was adhesive and had a flip-flop nature, with a consequent reducing water CA over time [37, 38], hence we thought these factors will interfere with the electrowetting evaluation.

2.2.4.1 Conductive Au coating

The thin Au conductive layer (60 nm) was coated on the soda-lime glass substrate using a Quick Coater (SC – 701, SANYU DENSHI). The substrate was first etched with an Al target at 5 mA for 3 min and the Au subsequently coated, using a Au target, at 5 mA for 3 min.

2.2.4.2 Hydrophobizing FAS coating

To obtain a superhydrophobic surface for electrowetting evaluation, the soda-lime glass-Au-rough pseudoboehmite coating was hydrophobized with FAS by dipping the sample into a

FAS solution (2 vol.% in ethanol) for 1 h, rinsed with ethanol, blow-dried with $N_{2(g)}$ and heat treated at 120 °C for 2 h.

2.2.5 Characterization

The microscopic structural changes due to various coatings and process treatments of the samples were observed by a field emission scanning electron microscopy (FE-SEM) [HITACHI S–4800]. Samples were coated with a thin layer of Pt/Pd [HITACHI E–1030; at 15 mA for 60 s] before observation under the microscope. The elemental composition was determined using an energy dispersive X-ray (EDX) spectroscope [EMAX Energy, HORIBA] attached to the FE-SEM microscope. The microstructural evaluation of the final samples was complemented with atomic force microscopy AFM [SFT-3500, Shimadzu] to ascertain the surface roughness. The crystallinity of the coated alumina was investigated by a field emission transmission electron microscope (FE-TEM) [JEOL JEM-2100 F FE-TEM], using samples of coatings scraped from the surface of the glass substrates. The optical transparency of the sample at various stages of preparation was measured using an optical spectrophotometer [Jasco V–560].

The thermal stability of the SHS was evaluated using a furnace; from 150 to 400 °C, at 50 °C incremental intervals and for 1 h test duration at each test temperature. This was complemented with a thermogravimetric-differential thermal analysis (TG-DTA) [Rigaku Thermo plus EV02, TG 82121] evaluation, in an air atmosphere at 50 ml min^{-1} and at a heating rate of 10 °C min^{-1}, using scraped coatings from the SHS samples.

The chemical stability was tested in two major forms: (1) dipping in a) a polar organic solvent (Ethanol) and b) a relatively non-polar organic solvent (Toluene), for 1 h each, respectively; and (2) dipping in a) an inorganic acid (H_2SO_4; 1 mol L^{-1}) and b) an inorganic base (NaOH; 1 mol L^{-1}), for 1 h each, respectively. After each stability test samples were

washed with IPA (but initially with water in the cases of the acid and base tests) and dried at 100 °C for 1 h in an oven. The robustness was evaluated via CA measurement, laser microscope and FE-SEM observations, before and after the various treatments, for surface degradation.

2.2.5.1 Water contact angle evaluation

The water CA of the samples at various stages of preparation of the SHS was evaluated by a sessile droplet method, using a CA equipment [DropMaster 300; Software: FAMAS 3.1.3 by Kyowa Interface Science Co. Ltd]. Using deionized water droplets, 3 µL, the CA at five different spots on a sample surface was measured and the average value taken. For EW and REW, the liquid droplet was composed of 79.93 wt.% water, 0.06 wt.% KCl [Wako, min. 99.5 wt.%] and 20.01 wt.% glycerin [Chameleon Reagent, min. 99.0 wt.%] (to suppress evaporation). The liquid system was sonicated for about 30 min. to remove possible gas bubbles.

2.2.5.2 EW evaluation in air

The EW behavior of the prepared sample was evaluated according to the following setup: the negative terminal was connected to the metallic Au coating layer of the glass substrate and the positive terminal to the Au wire [ALDRICH, min. 99.99 %, diameter = 0.1 mm] that would be inserted into the conducting liquid droplet. Measurement was done over a continuous period of 120 s as follows: the droplet (3 µL) was placed on the sample surface and the CA measured for the first 10 s, to ensure equilibration; the Au wire was then inserted into the droplet and after another 10 s equilibration period the voltage [voltage supplier: KIKUSUI PCR 500L] was switched on. The changes in CA over time and at various applied voltages were recorded.

2.2.5.3 REW evaluation in dodecane

The setup and evaluation for REW was as described for EW in air under section 2.2.5.2 above, but with the sample in a dodecane [Wako, min. 99.0 wt%] bath contained in a rigid transparent plastic container. The measurement duration was 2000 s. The droplet (3 µL) was put on the sample surface, in the dodecane bath, and the CA for the first 20 s was monitored for equilibration. The Au wire was then inserted into the droplet and after another equilibration period the voltage was switched on at 85 s. The CA change with time was recorded and the voltage was switched off at 220 s, to observe the reversible wetting for the remaining 1780 s.

2.3 RESULTS AND DISCUSSION

2.3.1 FE-SEM, Optical, AFM and CA

Figure 2.1 shows the SEM and CA characterizations of the surface of the soda lime glass substrate at various stages of coatings and treatments to obtain the SHS. Fig. 2.1 a) is the cross-sectional image of the porous alumina coating of 107 nm thick, after heat treatment (HT) at 500 °C. The surface of this sample exhibited hydrophilicity, Fig. 1 (b), with a CA of 41.7 ± 1.2 °. Fig. 1 c) is the cross-sectional image after HWT. A drastic change in the surface microstructure is observed by the development of ~140 nm long rough nanostructures, from the porous alumina. The growth of these rough structures is attributed to the formation of pseudo-crystallites by Oswald ripening and this is supported by the observed remnant undissolved porous alumina layer between the rough structures and the glass substrate; and the increase in thickness, from 107 nm of porous alumina in Fig. 2.1 a) to 200 nm of porous alumina-rough alumina structures. The HWT is also thought to remove residual organic components and other impurities after the HT, by their dissolution into the water.

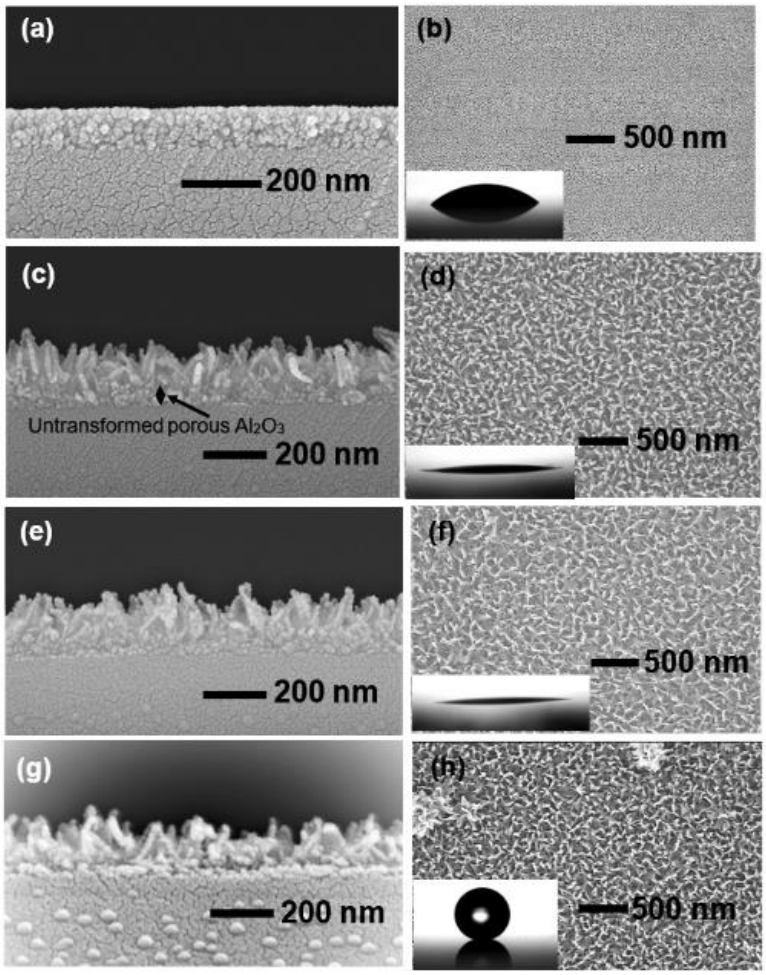

Fig. 2.1: FE-SEM images and corresponding contact angle images (insets) of 3 µL water droplets on the surface, at various stages of the preparation of the SHS showing different wetting states: **a)** and **b)** cross-section and surface of porous alumina (~ 107 nm) on the glass substrate after HT with a CA of 41.7 ± 1.2 °; **c)** and **d)** cross-section and surface of rough pseudoboehmite structures (~ 140 nm long) on untransformed porous alumina (~ 60 nm) with a CA of 6.6 ± 0.4 °; **e)** and **f)** cross-section and surface of the rough pseudoboehmite structures after the 2nd HT, with a CA of 5.7 ± 0.4 °; **g)** and **h)** cross-section and surface of LBL-coated rough surface of the finished SHS with CA of 167.2 ± 0.8 °.

The gradient microstructuring of the coating of rough structures-porous alumina-glass substrate, caused a moth-eye antireflective coating effect, increasing the sample's transmittance of visible light by about 4 %, with an overall transparency of 95 % (Fig. 2.2).

Fig. 2.1 d) shows the sample surface after HWT of the precipitated flower-like rough structures, with an inset of a water droplet on it showing superhydrophilicity, CA = 6.6 ± 0.4 °. This is the Wenzel wetting, based on the reasoning that the surface texture changes from the relatively smooth porous alumina to a rough surface (arithmetic average roughness, R_a, = 33.8 nm; maximum valley depth, R_v, = 155.9 nm, from AFM measurements of Fig. 2.3). This increases the roughness factor, ***r***, in eqn. 2.2, and hence, the consequent decrease in CA, given that the intrinsic CA, Θ**,** of the porous alumina is < 90 ° (41.7 °). This was further corroborated by the sharp increase in, and high, CA obtained after the thin hydrophobizing LBL coating, shown in Fig. 2.1 h). The second HT, after HWT, was to enhance the formation of the precipitated rough structures; burn off remnant organic component; and remove non-chemically bound water. It slightly enhanced the superhydrophilicity of the surface from 6.6 ° to 5.7 ± 0.4 °, Fig. 2.1 f), which suggests either a chemical or textural modification; or both. In Fig. 2.3 the R_v, value of 155.9 nm is comparable to the estimated rough structures height of 140 nm, from the SEM images of Fig. 2.1 c, e and g).

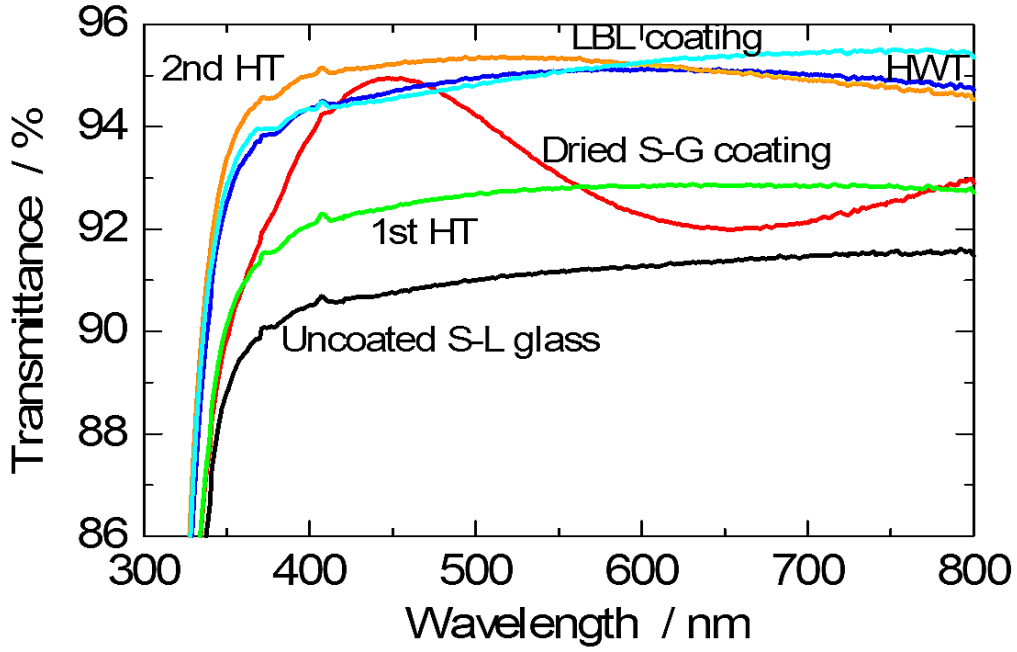

Fig. 2.2 UV-Visible spectra of SHS sample at various stages of preparation showing enhanced transmittance.

The alumina coating was scraped and analyzed for its crystalline structure. The X-ray powder diffraction pattern showed no crystalline peaks, however, the TEM evaluation, as shown in Fig. 4, shows some level of crystallinity. Fig. 4 (a) shows the bright field image of cubic-like structures but not the typical rhombic, nor hexagonal nor lentil-like/plate-like microcrystals of boehmite [39]. Fig. 4 (b) is the high resolution image showing some level of crystalline fringes, however they are not well developed; and Fig. 4 (c) is the selected area electron diffraction pattern of the sample also showing some crystalline spots, but also poorly developed. Thus the sample shows partially disordered crystal structure. The term "pseudoboehmite" was basically coined to differentiate between well-crystallized boehmite

and pseudocrystallized or gelatinous boehmite [39]. Hence, the rough structure coating is hereby referred to as pseudoboehmite.

The absence of the pseudoboehmite peaks in the classical XRD measurement is attributed to the limiting effect of its wide field of focus vis-à-vis the nanoscale texture and structure of the pseudoboehmite structures, in addition to its detection limit of 5 %.

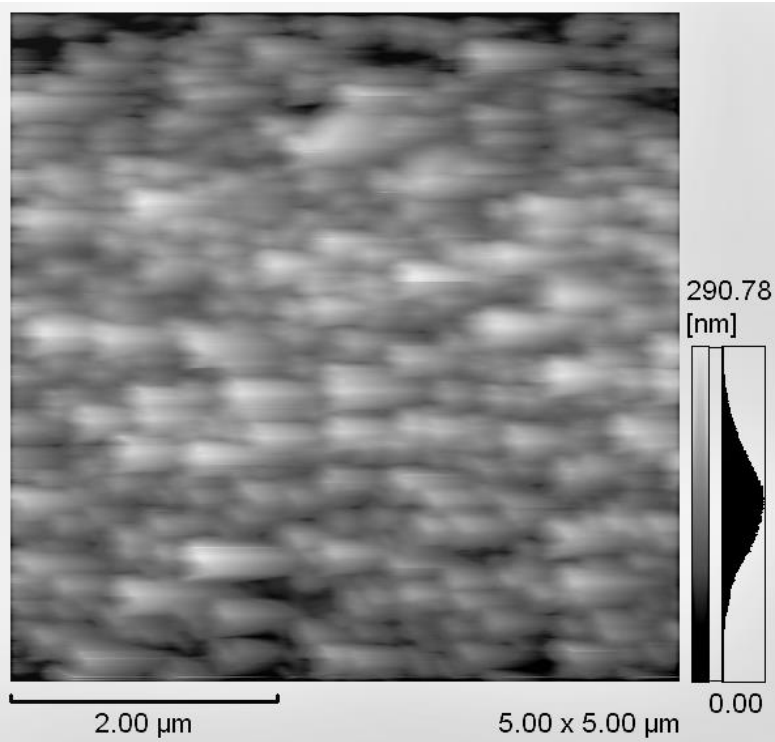

Fig. 2.3 AFM image of the SHS sample after preparation of rough pseudoboehmite structures; with average roughness, R_a, of 33.8 nm and maximum valley depth, R_v, of 155.9 nm.

Fig. 2.1 g) shows a cross-sectional image of the final SHS sample after the hydrophobizing LBL coating. There is no observed significant change in the texture or microstructure in the SEM image because of the thinness of one-layer PDDA-Nafion® film. The thicknesses of these films were estimated with a Quartz Crystal Microbalance with Au-metallized electrode

and a resonance frequency of 9 MHz. A combined thickness of 3.7 nm was obtained: 2.0 nm (= 325.5 ng cm^{-2}) of Nafion®; and 1.7 nm (= 188.4 ng cm^{-2}) of PDDA. However, the presence of the thin hydrophobizing coating is observed in the drastic change in CA, shown in Fig. 1 h); in the robustness tests results of Table 1; and TG-DTA results of Fig. 2.5. Fig. 2.1 h) shows the surface of the finished SHS with rough flower-like pseudoboehmite structures. The inset image is a water droplet on it showing the superhydrophobicity of the surface with a very high CA of 167.2 ± 0.8 °. The untreated soda-lime glass substrate has a CA of 15.2 ± 0.5 ° (after 500 °C HT, CA = 5.4 ± 1.2 °), and when it was coated with the PDDA-Nafion® it became hydrophobic with a CA of 93.2 ± 0.5 °. Coating only PDDA on the rough structures gave a superhydrophilic surface, CA= 6.5 ± 0.4 °, ascribed to unneutralized ammonium ionic groups of the PDDA interacting with the polar water molecules. Thus, a combination of the roughness (rough pseudoboehmite structures) and low surface energy (induced by Nafion®) resulted in a Cassie-Baxter state SHS.

We think it is significant to note here that, although the Wenzel and Cassie-Baxter models were proposed using regular or uniformly defined rough structures, such as rectangular pillars, nevertheless, they serve as good guides, for all other rough structure morphologies, such as our irregularly rough pseudoboehmite structures, to help predict the outcome of wettability results of SHSs without necessarily using the absolute values of the variables of the equations from these models.

Our SHS obtained was however, adhesive such that when a water droplet on it was tilted, and further turned upside down the droplet remained attached to the surface. This indicated a very high CA hysteresis, which is a measure of the difference between the maximum advancing CA and minimum receding CA of a droplet on a tilted substrate, and which is a factor to be considered when dealing with motion of droplets on surfaces, as described in eqn. 2.6 below:

$$F_s = \gamma_{LA} W(\text{Cos}\,\Theta_r - \text{Cos}\,\Theta_a) \quad [40, 41] \quad (2.6)$$

F_s is the force needed to move the droplet; W is the width of the droplet bottom on the surface; Θ_r is the receding CA; and Θ_a is the advancing contact angle.

This high adhesiveness is attributed to unneutralized —NR_4^+ groups from PDDA, and/or —SO_3^- groups from Nafion®, interacting with the polar water molecules of the droplet. The randomly distributed rough structures could also be a contributory factor to this adhesiveness.

2.3.2 SHS Robustness

For the various possible areas of applications, the SHS was tested for its robustness in terms of stability at various temperatures and in various solvents. The results are shown in Table 2.1. The SHS was stable up to a temperature of 300 °C without any significant change in CA or surface degradation, via a laser microscope and FE-SEM observations. However, at 350 °C and above, the SHS became completely wetting, with CA < 5 °, although there was no observed change in the surface microstructure, under FE-SEM observation. These results were comparable to Fig. 2.1 (e and f), that is before the hydrophobization coating, which indicate the combustion of the hydrophobizing coating of PDDA-Nafion. This was corroborated by a TG-DTA analysis of the scraped coating of the SHS sample, as shown in Fig. 2.5. An exothermic peak can be observed around 318 °C with a corresponding weight loss, which are attributed to the combustion energy and loss of the PDDA-Nafion, respectively. A starting mass of 21.599 mg of the scraped coating was used, and from the TG curve, less than 0.5 wt. % loss was observed. Considering that both PDDA and Nafion have molecular masses of at least a thousand times greater than alumina, suggests it is a minute proportion of the SHS coating, and hence, an indication of how thin the LBL coating of these components are.

The SHS was stable in 1 mol L^{-1} inorganic acid ($H_2SO_{4(aq)}$); 1 mol L^{-1} inorganic base ($NaOH_{(aq)}$); polar solvent (ethanol); and non-polar organic solvent (toluene), as shown in Table 2.1. In addition, it was stable to UV irradiation for 1 h. From Table 2.1, there seem to be an apparent small increase in CA after each test. This is thought to be due to a slight chemical or physical modification of the

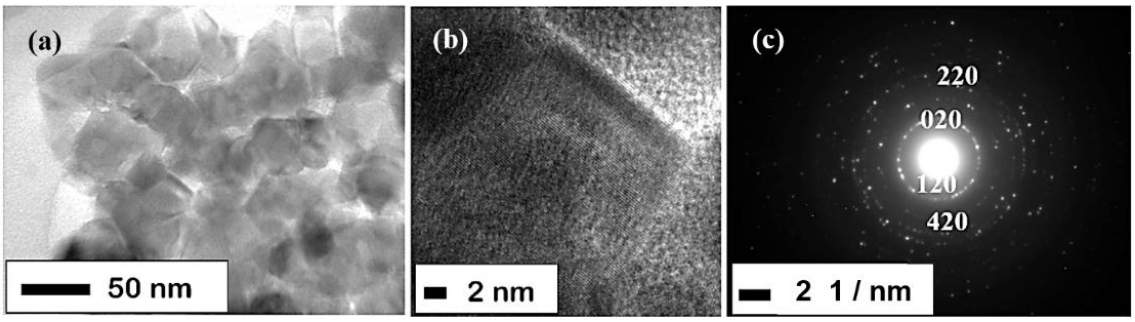

Fig. 2.4 TEM images of Al_2O_3 scraped coating on S-L glass after HWT and 500 ^oC HT: **a)** bright field image showing cubic-like structures; **b)** high resolution image showing poor crystallinity of poorly developed crystalline fringes; and **c)** corresponding selected area electron diffraction pattern showing poorly developed crystalline spots.

SHS by the removal of chemically or physically bound polar inclusions such as water molecules via the high temperature HT or organic solvent treatment; or capping of free ionic ammonium groups of PDDA or sulfonyl groups of Nafion® by the acid or base treatments, respectively. Thus, a robust thin film SHS was prepared. Also, for a very thin hydrophobizing film to remain stable under these tests conditions indicates a very uniform layering coating by the LBL technique and a strong bonding to the alumina coating.

2.3.3 EW in Air

2.3.3.1 Microstructure of EW SHS

A change in only the hydrophobizing coating, from PDDA-Nafion® to the FAS material, gave a similar SHS wetting as the PDDA-Nafion® sample, with a CA of 166.4 ± 0.6 °. However, this new SHS was not adhesive and water droplets easily rolled off its surface, indicating a low CA hysteresis. The change to a lower HT temperature of 120 °C of the alumina gel coating, produced a thicker remnant porous alumina, of about 130 nm (Fig. 2.6 (a)), after HWT, compared to 60 or 50 nm in the 500 °C heat-treated sample (Fig. 2.1 (c or g), respectively). This was attributed to a large amount of remnant organic component (low alumina per unit area) in the coating before HWT. That is, more time and energy was used to dissolve the remnant organic component, obtaining less amount of alumina per unit area for the Oswald ripening growth of the rough structures. This resulted in shorter rough structures of about 110 nm (Fig. 2.6 a)), compared to about 140 or 150 nm of the 500 °C heat-treated sample, Fig. 2.1 (c or g, respectively). These findings were corroborated by AFM roughness evaluation, shown in Fig. 2.7. The surface shows a similar profile as that of the 500 °C treated sample, but with lower R_a and R_v values of 24.8 and 88.4 nm, respectively. For this reduction in roughness, a consequent reduction in the apparent CA was expected, deducing from eqn. 2.2, since r will decrease. Thus, the lower CA of 155.4 ± 0.6 ° (Fig. 2.6 b) i)) obtained.

The XRD and TEM results of scrapings of this SHS showed similar results as for the 500 °C heat-treated sample, section 2.3.1, with no pseudoboehmite peaks observed in the XRD pattern but the characteristic spike morphology of pseudoboehmite [42] was observed in the bright field TEM image, Fig. 2.8 (a). In addition, the high resolution image (Fig. 2.8 b)) showed poorly formed crystalline fringes with the corresponding selected area electron diffraction pattern (Fig. 2.8 c)) showing poorly developed crystalline spots.

Table 2.1: CA results showing thermal and chemical robustness of the SHS.

		CA / °	
		Before treatment	**After treatment**
Stability test Treatment condition	Thermal	167.2 ± 0.8	166.7 ± 0.7 (300 °C)
		167.2 ± 0.8	< 5 (350 °C)
	UV	167.2 ± 0.8	168.3 ± 0.5
	Ethanol	167.2 ± 0.8	166.2 ± 0.9
	Toluene	167.2 ± 0.8	168.8 ± 0.7
	1 mol L^{-1} H_2SO_4	167.2 ± 0.8	168.3 ± 0.9
	1 mol L^{-1} NaOH	167.2 ± 0.8	168.6 ± 0.9

Thus, the rough structures are considered to be pseudoboehmite structures. These results also indicate that the attained pseudo-crystallinity was mainly due to the low temperature HWT; with additional enhancement from the post HWT HT, seen in the relatively higher crystallinity of the 500 °C heat-treated sample than that of the 120 °C heat-treated sample.

2.3.3.2 EW and dielectric breakdown

The added KCl in the water for EW evaluation was to render it a perfect conductor by reducing the Debye length, which reduces the separation of conducting charges (mainly the K^+ and Cl^- ions in this situation) in the droplet, caused by applied voltage. Glycerin was added to suppress evaporation of the droplet. In all measurements, after insertion of the Au

electrode into the droplet, the setup was allowed a time period of 2 min to ensure equilibration before the voltage supply was turned on.

Table 2.2 and Fig. 2.6 b) show the results of the EW evaluation in air. The CA measurements were taken continuously at a rate of CA (in degrees) per second over a total measuring time period of 2 min, with the voltage supply switched on at 12 s. Although the response to the voltage application was immediate, the total CA change and equilibration periods were usually in the range of 15 to 20 s. This relatively long equilibration time is thought to be due to the random nature of the rough structures; such that the wetting droplet takes some time to

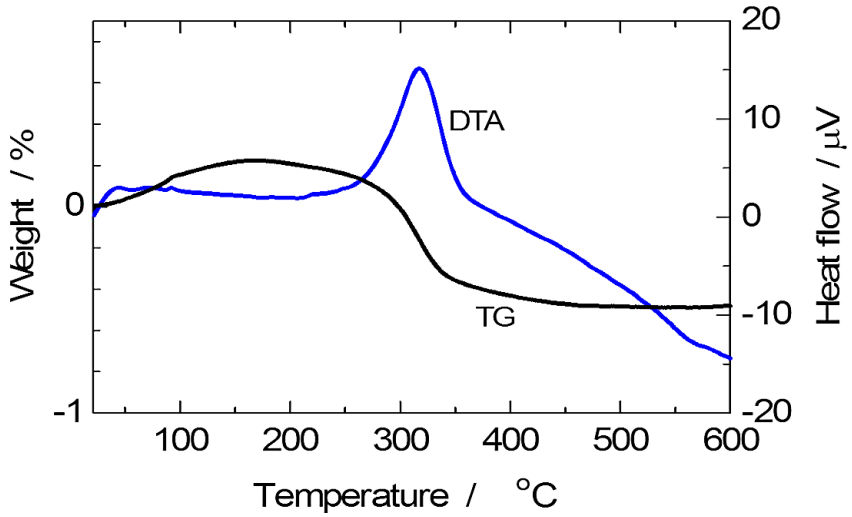

Fig. 2.5 TG-DTA curves of the scraped superhydrophobic coating showing the combustion of the hydrophobizing LBL coating of PDDA-Nafion® at 318 ˚C, with an exothermic peak and corresponding weight loss.

percolate through the random structures to transition from the Cassie-Baxter state [13] to the Wenzel state [12].

From Table 2.2, the actuation voltage, V_a, at which EW begins can be estimated to be in the range of $2 < V_a \leq 3$ V, with 3 V giving a CA change of 2 °. The low actuation voltage was predicted from eqn. 2.5, in terms of a reduced dielectric thickness, *d*. This compares well with reported works [40, 41], who used thicker (in the micrometer-scale range) dielectric-hydrophobizing material coatings, thus, reporting 10's to 100's magnitude values of actuation voltages. Our dielectric coating is < 300 nm (~ 240 nm, Fig. 2.6 (a)), hence the low actuation voltage. This is an extremely low actuation voltage in the EW field [1-3].

Considering the magnitude of CA change in response to applied voltage, a drastic change is observed after 4 V (at 4.5 and 5 V), compared to those observed at 3 and 4 V. This is explained to be due to the onset and breakdown of the dielectric coating, exposing the hydrophilic substrate. Droplet spot areas on the SHS were observed by both laser optical microscope and FE-SEM EDX to monitor for possible surface coating degradation, due to possible dielectric breakdown when the saturation voltage is exceeded. This droplet spot disc was reported by Verheijen et al [19] that, in DC experiments charge trappings in the insulator cause a hydrophilic disk, observed a posteriori, at the exact location of the droplet. This was observed in our sample after 4.5 V. From these observations and the results obtained in Table 2.2, the saturation voltage for our system was found to be ~ 4 V, with a working CA change of 2 °. The FE-SEM result in Fig. 2.9 shows the droplet spot disc after the dielectric breakdown, and Table 2.3 is the corroborating FE-SEM EDX results by the difference in the elemental distribution of key elements (Al, Au Si, O, Na and Ca) of the inside and outside of the droplet spot disc. From Table 2.3, Al and Au are not recorded inside the droplet disc (taken from the region labelled "Edge" in Fig. 2.9) but recorded outside (about 1 mm from the droplet spot disc). This indicates a complete peeling off of the alumina and conducting Au coatings. In addition, Si, O, Na and Ca (the main constituents of the S-L glass substrate) recorded higher values inside the droplet disc than the outside; a confirmation of the exposure

of the hydrophilic glass substrate. No Ca is recorded outside the droplet disc; this is attributed to either the relatively low concentration of Ca, or probably, the migration of Ca ions away from the glass surface, as a result of the various treatments to obtain the SHS, with regards to the limiting effect of the low penetration depth of the electron beam probe of the EDX technique.

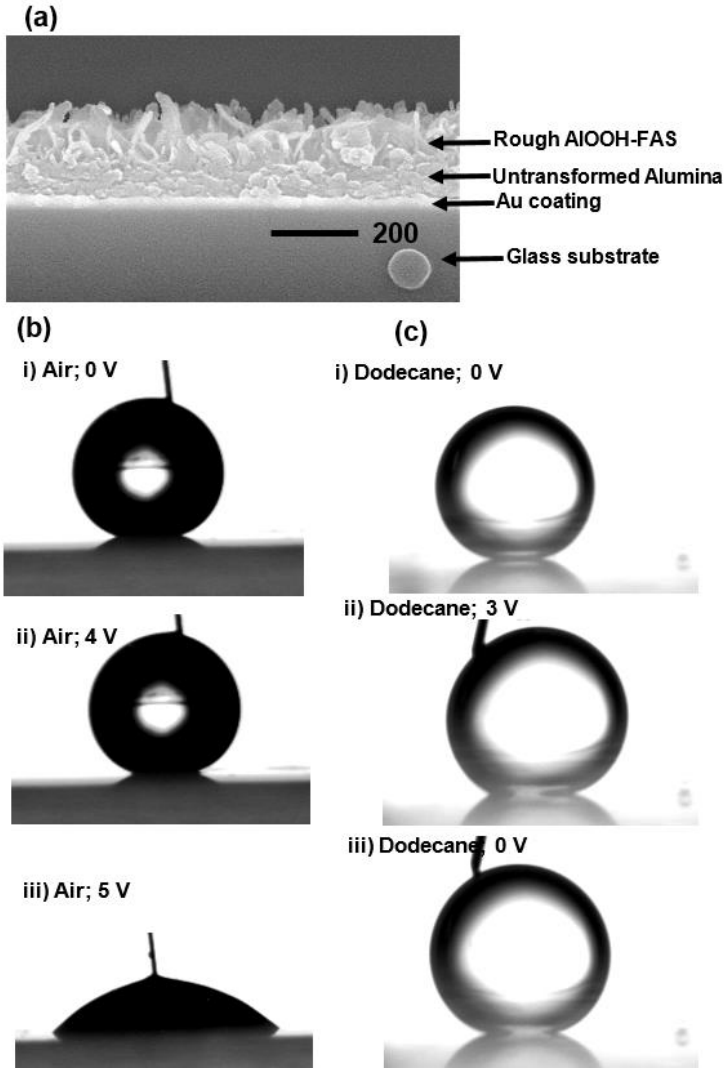

Fig. 2.6 a) FE-SEM cross-sectional image of sample for EW & REW; droplet images of **b)** EW in air and (**c)** REW in dodecane medium. **b) i)** sessile droplet with an inserted Au conductor with 0 V supply, CA = 155.4 ± 0.6 °; **b) ii)** 4 V supply, CA = 153.3 ± 0.4 °; **b) iii)** 5 V supply, CA = 48.5 ± 1.2 °. **c) i)** droplet with 0 V, CA = 161.3 ± 0.4 °; **c) ii)** droplet with 3 V supply, CA = 152.4 ± 0.6 °; **c) iii)** reversed electrowetted droplet when voltage was turned off, CA = 157.3 ± 0.8 °.

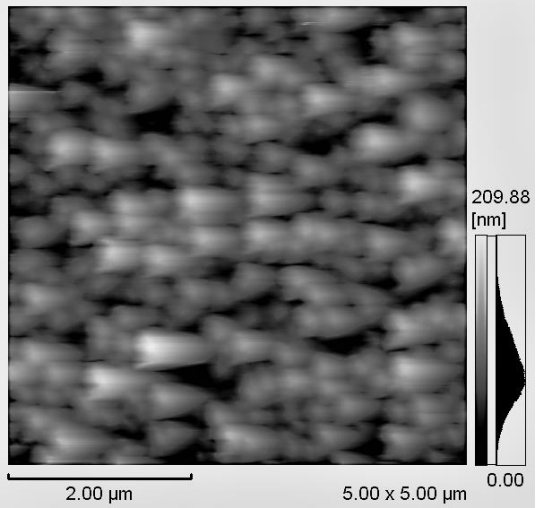

Fig. 2.7 AFM image of the rough sample surface for EW & REW with average roughness, R_a, of 24.8 nm and maximum valley depth, R_v, of 88.4 nm.

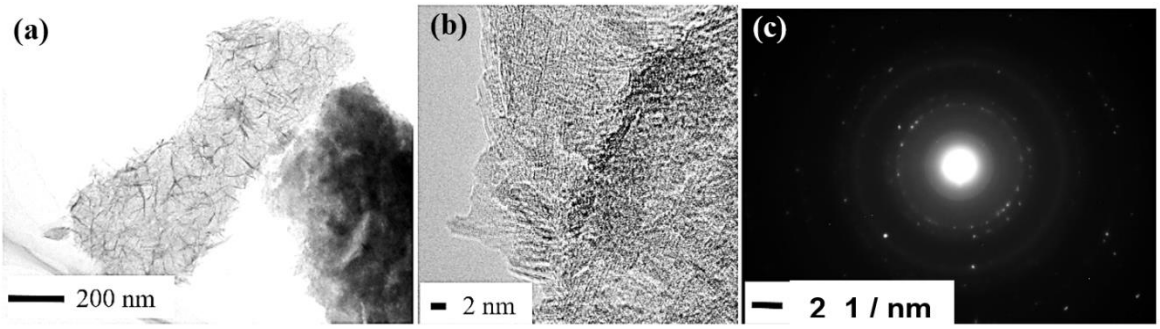

Fig. 2.8 TEM images of scraped Al_2O_3 coating on S-L glass after HWT and 120 ^oC HT: **a)** bright field image showing the characteristic spike morphology of pseudoboehmite; **b)** high resolution image showing poor crystallinity of the attempted development of crystalline fringes; and **c)** corresponding selected area electron diffraction pattern showing poorly developed crystalline spots.

The relatively short EW working CA range of 2 ° is attributed to the lower starting CA of 155 °, Fig. 2.6 b). This is supported by the observation that during the REW measurement in dodecane oil medium (which is discussed later), the starting CA, of the same sample, increases to 161° in the oil medium, giving an increased EW working CA change of 9 ° with the same 3 V. Thus, with appropriate modification, like a longer HWT or a thermally stable conductive layer to allow for a higher HT temperature to obtain longer rough structures, a higher starting CA could be obtained to give a wider EW working CA range.

Table 2.2: Electrowetting in air and the stability of the dielectric coating to the applied voltage.

Initial CA (θ) / °	**Applied voltage / V**	**Final CA (θ_v) / °**	**Surface degradation / Dielectric breakdown**
154.4 ± 0.6	0	155.2 ± 0.6	-
154.4 ± 0.6	1.0	155.2 ± 0.6	-
154.4 ± 0.6	2.0	155.2 ± 0.6	-
154.4 ± 0.6	3.0	153.3 ± 0.5	-
154.4 ± 0.6	4.0	153.4 ± 0.7	-
154.4 ± 0.6	4.5	78.7 ± 0.8	Bump at droplet spot
154.4 ± 0.6	5.0	48.7 ± 1.2	Coatings peeled off

2.3.4 REW in dodecane

The REW was similarly done as for EW, but in a dodecane bath, measuring CA every second and for a total measuring time of 33 min (2000 s), shown in Figs 2.6 (c) and 2.10. The voltage, 3 V, was switched on at 85 s, and turned off at 220 s. Fig. 2.6 (c) i) shows a droplet on the EW SHS sample in dodecane oil with no applied voltage, showing a CA of 161.3 ± 0.4 °. This CA is higher than the CA in air of 155 °. This increase is attributed to the hydrophobic dodecane bath, which reduces the interfacial tension between the droplet and the surrounding medium, that is γ_{LA} in eqn. 2.5, from ~ 73 mN m^{-1} to ~ 50 mN m^{-1}; and it also decreases CA hysteresis, by ~ 1 ° [38]. The CA was fairly constant until when the 3 V was applied. It decreased sharply to 157 ° in ≤ 1 s, and subsequently took about 10 to 15 s to equilibrate to 152.4 ± 0.6 °, Fig. 2.6 (c) ii), indicating EW. When the voltage was turned off at 220 s, the CA increased to 157.3 ± 0.8 °, Fig. 2.6 (c) iii), within 15 s; and remained approximately constant for the rest of the test period, indicating REW. A graphical presentation of the full process of EW and REW is shown in Fig. 2.10. The ~ 15 s EW CA equilibration is attributed to the time taken by the droplet to percolate through the rough structures, transitioning from the Cassie-Baxter state [13] to the Wenzel [12] (or partial Cassie-Baxter) state. A similar explanation is given for the relatively slow 15 s time period for the REW as due to the resistance offered by the randomly oriented rough structures, as the wetted fraction of droplet is being displaced by refilling dodecane oil. The larger EW CA change of 9 °, compared to 2 ° in air, is attributed to the higher starting CA of 161 °.

The REW in the dodecane occurred on the principle that during the wetting transition from Cassie-Baxter state to the Wenzel state, the droplet displaces dodecane from the rough structures, but a thin film of the dodecane remains on the surface of the rough structures, preventing the droplet from pinning onto the rough structures; and when the voltage supply is

removed, the dodecane refills into the rough structures, via capillary action, returning the droplet to the original Cassie-Baxter state.

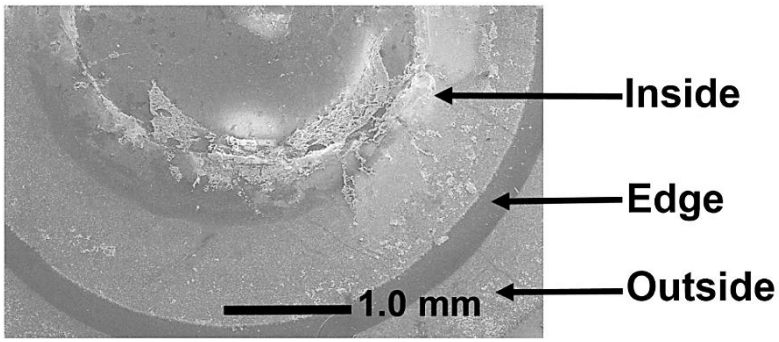

Fig. 2.9 FE-SEM image of the EW droplet disc spot showing the damaged coating surface after exceeding the saturation voltage at 5 V.

The inability of the electrowetted droplet to fully return to the starting CA of 161° is presumed to be due to the effect of gravity and/or the thermodynamic consequence of the metastable nature of the Cassie-Baxter state. The CA evaluation of small droplets is based on the assumption that the shape of the droplet is governed by surface tension with no (or a minimal) effect of gravity, by reason of the bond number, B_o, eqn. 2.7,

$$B_o = \rho g R^2 / \gamma \quad (2.7)$$

ρ is the density of droplet; g is the acceleration due to gravity; R is the dimension of the order of the radius of the droplet; γ is the surface tension of the droplet (= γ_{LA}).

B_o is dimensionless and measures the strength of gravity relative to surface tension. If $B_o < 1$, the droplet would be spherical; otherwise the droplet would have a shape within: less-than-

spherical to nonspherical, depending on the magnitude of the value. Usually, a droplet of a size of 1 mm or less is appropriate [10]; our droplet was 3 µL (~ 2 mm). Thus, the larger droplet size means a larger *R*, with a consequent large B_o, which would thus, increases the effect of gravity. This will cause a suppressive effect on the capillary rise of the dodecane. The added thermodynamic reason is that, a system would not normally spontaneously return to its metastable state, and hence could be one of the effects on our system. Thus, we tried using relatively larger and smaller droplets for the REW evaluation. When a larger droplet, 4 µL, was used, no REW was observed; and when an attempt was made to use a smaller droplet, 2 µL, it was found to be completely non-wetting, and would easily roll away each time an attempt was made to insert the Au wire conductor into it.

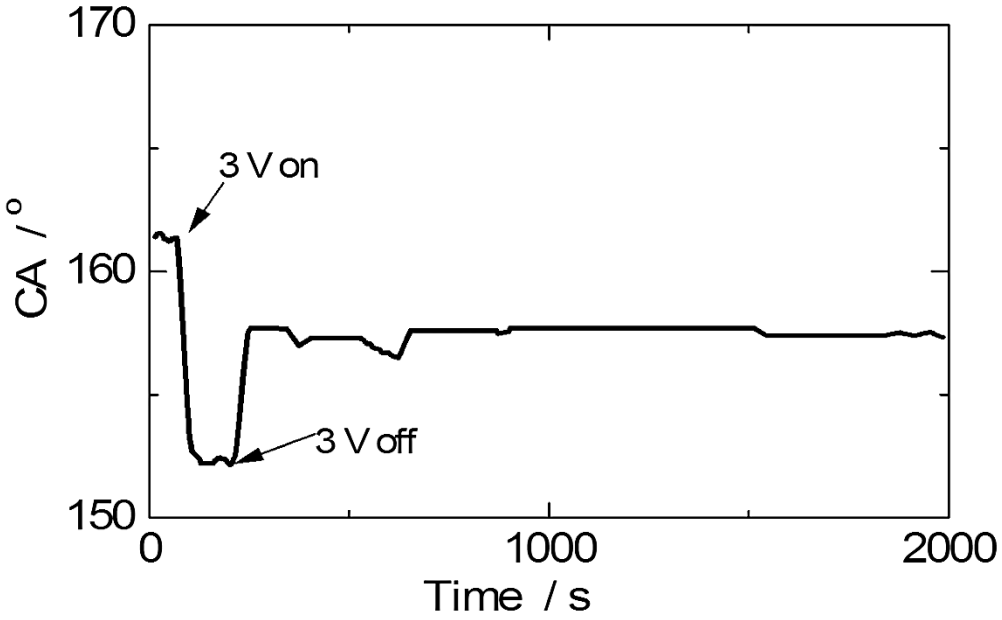

Fig. 2.10 Graph of the reversible electrowetting in dodecane medium showing a decrease in CA at 85 s when the voltage is turned on; and the rise in CA at 220 s when the voltage is turned off.

No electrolysis effects were observed in both the EW and REW evaluations. When the REW was repeated 10 times at the same spot, with a fresh droplet each time, similar REW results of 161 ° → 152 ° → 157 ° were obtained. An FE-SEM observation of the droplet spot confirmed that there was no degradation of the SHS.

2.4 Conclusion

A superhydrophobic coating was prepared on a soda-lime glass by the use of pseudoboehmite alumina rough structures and Nafion® hydrophobizing coatings, using facile and low cost techniques of sol-gel, HWT and LBL coating. The SHS showed a high water CA of 167.2 ± 0.8 ° with high adhesiveness. It was highly transparent and thermally stable up to 300 °C. It was also stable in sulphuric acid, sodium hydroxide, toluene, ethanol, and stable to UV irradiation. For EW evaluation, and to avoid the possible complex effect(s) of the adhesive nature of the Nafion® coating, it was replaced with FAS (1H, 1H, 2H, 2H-perfluorodecyltrimethoxysilane). Also, a thin Au conductive layer was coated before the alumina coating, causing a reduction in the HT temperature of the alumina coating to 120 °C, to protect the Au layer from aggregating. This resulted in relatively shorter rough structures, with a consequent relatively lower CA of 155.4 ± 0.6 °. Nevertheless, it showed an extremely low dc actuation voltage of 3 V, with a corresponding CA change of 2 °; a threshold voltage of about 4 V; and dielectric breakdown at 4.5 V. A REW was achieved with this sample in a dodecane bath, using 3 V. A higher corresponding CA change of 9 ° was obtained. These stable nano-scale coatings with low actuation voltage are unique preliminary achievements and can easily be integrated into current desired nano-devices fabrications. The results of this research suggest these unique and good preliminary achievements can, nevertheless, be improved upon with further research.

REFERENCES:

1. F. Mugele, J-C. Baret, Electrowetting: from basics to applications, J. *Phys.: Condens. Matter*, **17** (2005) R705–R774.

2. Y-P. Zhao, Y. Wang, Fundamentals and applications of electrowetting: a critical review, *Rev. Adhesion Adhesives*, **I** (2013) 114-173.

3. M. F. Samad, A. Z. Kouzani, M. M. Rahman, K. Magniez, A. Kaynak, Design and fabrication of an electrode for low-actuation-voltage electrowetting-on-dielectric devices, *Procedia Technology*, **20** (2015) 20-25.

4. A. Tuteja1, W. Choi, M. Ma, J. M. Mabry, S. A. Mazzella, G. C. Rutledge, G. H. McKinley, R. E. Cohen, Designing superoleophobic surfaces, *Science*, **318** (2007) 1618-1622.

5. T. Krupenkin, J. A. Taylor, Reverse electrowetting as a new approach to high-power energy harvesting, *Nature Communications*, **2** (2011) 1-7.

6. H. You, A. J. Steckl, Three color electrowetting display device for electronic paper, *Appl. Phys. Lett.*, **97** (2010) 023514(1-3).

7. R. B. Fair, Digital microfluidics: is a true lab-on-a-chip possible?, *Microfluid. Nanofluid.*, **3** (2007) 245-281.

8. B. Berge, J. Peseux, Variable focal lens controlled by an external voltage: an application of electrowetting, *Eur. Phys. J. E.*, **3** (2000) 159-163.

9. S. Chevalliot, J. Heikenfeld, L. Clapp, A. Milarcik, S. Vilner, Analysis of nonaqueous electrowetting fluids for displays, *J. Display Technol.*, **7** (2011) 649-656.

10. K. Koch, W. Barthlott, Superhydrophobic and superhydrophilic plant surfaces: an inspiration for biomimetic materials, *Phil. Trans. R. Soc. A*, **367** (2009) 1487–1509.

11. T. Nishino, M. Meguro, K. Nakamae, M. Matsushita, Y. Ueda, The lowest surface free energy based on $-CF_3$ alignment, *Langmuir*, **15** (1999) 4321–4323.

12. R. N. Wenzel, Resistance of solid surfaces to wetting by water, *Ind. Eng. Chem.*, **28** (1936) 988-994.

13. R. Cassie, S. Baxter, Wettability of porous surfaces, *Trans. Faraday Soc.*, **40** (1944) 546-551.

14. G. Beni, S. Hackwood, Electro-wetting displays, *Appl. Phys. Lett.*, **38** (1981) 207–209.

15. B. Berge, Electrocapillarity and wetting of insulator films by water, *C. R. Acad. Sci.*, **317** (1993) 157–163.

16. W. C. Nelson, C-J. Kim, Droplet actuation by electrowetting-on-dielectric (EWOD): A review, *J. Adhesion Sci. Technol.*, **26** (2012) 1747-1771.

17. J. Berthier, Micro-Drops and Digital Microfluidics, second ed., *Elsevier (William Andrew Inc.)*, USA (2013) 161-222.

18. M. Vallet, M. Vallade, B. Berge, Limiting phenomena for the spreading of water on polymer films by electrowetting, *Eur. Phys. J. B.*, **11** (1999) 583-591.

19. H. J. J. Verheijen, M. W. J. Prins, Reversible electrowetting and trapping of charge: model and experiments, *Langmuir*, **15** (1999) 6616-6620.

20. B. Shapiro, H. Moon, R. L. Garrell, C-J. Kim, Equilibrium behavior of sessile drops under surface tension, applied external fields, and material variations, *J. Appl. Phys.*, **93** (2003) 5794-5811.

21. T. B. Jones, J. D. Fowler, Y. S. Chang, C-J Kim, Frequency based relationship of electrowetting and dielectrophoretic liquid microactuation, *Langmuir*, **19** (2003) 7646–7651.

22. A. G. Papathanasiou, A. G. Boudouvis, A manifestation of the connection between dielectric breakdown strength and contact angle saturation in electrowetting, *Appl. Phys. Lett.*, **86** (2005) 164102-164103.

23. V. Peykov, A. Quinn, J. Ralston, Electrowetting: a model for contact-angle saturation, *Colloid Polym. Sci.*, **278** (2000) 789-798.

24. A. Torkelli, Droplet Microfluidics on planar surface. Ph D Thesis, Department of Electrical Engineering, Helsinki University of Technology, Espoo, *VTT Technical Research Centre, Finland* (2003) 53-57.

25. T. N. Krupenkin, J. A. Taylor, E. N. Wang, P. Kolodner, M. Hodes, T. R. Salamon, Reversible wetting-dewetting transitions on electrically tunable superhydrophobic nanostructured surfaces, *Langmui*r, **23** (2007) 9128-9133.

26. R. J. Vrancken, H. Kusumaatmaja, K. Hermans, A. M. Prenen, O. Pierre-Louis, C. W. M. Bastiaansen, D. J. Broer, Fully reversible transition from Wenzel to Cassie−Baxter states on corrugated superhydrophobic surfaces, *Langmuir*, **26** (2010) 3335-3341.

27. E. F. Hare, E. G. Shafrin, W. A. Zisman, Properties of films of adsorbed fluorinated acids, *J. Phys. Chem.*, **58** (1954) 236-239.

28. H. M. Shang, Y. Wang, S. J. Limmer, T. P. Chou, K. Takahashi, G. Z. Cao, Optically transparent superhydrophobic silica-based films, *Thin Solid Films*, **472** (2005) 37-43.

29. S. K. Cho, S-K. Fan, H. Moon, C-J. Kim, Towards digital microfluidic circuits: creating, transporting, cutting, and merging liquid droplets by electrowetting-based actuation, 15th *IEEE Int. Conf. MEMS*, **11** (2002) 32-35.

30. S. K. Cho, H. Moon, C-J. Kim, Creating, Transporting, cutting, and merging liquid droplets by electrowetting-based actuation for digital microfluidic circuits, *J. of Microelectromech. Syst.*, **12** (2003) 70–80.

31. M. G. Pollack, A. D. Shenderov, R. B. Fair, Electrowetting-based actuation of droplets for integrated microfluidics, *Lab Chip*, **2** (2002) 96-101.

32. M. G. Pollack, A. D. Shenderov, R. B. Fair, Electrowetting-based actuation of liquid droplets for microfluidic applications, *Appl. Phys. Lett.*, **77** (2000) 1725-1727.

33. Y-Y. Lin, R. D. Evans, E. Welch, B-N. Hsu, A. C. Madison, R. B. Fair, Low voltage electrowetting-on-dielectric platform using multi-layer insulators, *Sensors and Actuators B*, **150** (2010) 465-470.

34. A. Nakajima, K. Hashimoto, T. Watanabe, Recent studies on super-hydrophobic films, *Monatshefte für Chemie*, **132** (2001) 31-41.

35. Y-Y. Yan, N. Gao, W. Barthlott, Mimicking natural superhydrophobic surfaces and grasping the wetting process: A review on recent progress in preparing superhydrophobic surfaces, *Adv. Colloid Interface Sci.*, **169** (2011) 80-105.

36. K. Tadanaga, N. Katata, T. Minami, Super-water-repellent Al 2O 3 coating films with high transparency, *J. Am. Ceram. Soc.*, **80** (1997) 1040-1042.

37. G. Kawamura, T. Ema, H. Sakamoto, X. Wei, H. Muto, A. Matsuda, Spontaneous changes in contact angle of water and oil on novel flip–flop-type hydrophobic multilayer coatings, *Applied Surface Science*, **298** (2014) 142–146.

38. X. Wei, I. Mogami, G. Kawamura, H. Muto, A. Matsuda, A wettability tunable surface of Nafion® with controlling the flip-flop property by dc applied voltage, *Key Engineering Materials*, **616** (2014) 77-81.

39. P. S. Santos, A. C. V. Coelho, H. S. Santos, P. K. Kiyohara, Hydrothermal synthesis of well-crystallised boehmite crystals of various shapes, *Mat. Res.*, **12** (2009) 437-445.

40. J. Heikenfeld, M. Dhindsa, Electrowetting on superhydrophobic surfaces: present status and prospects, *Journal of Adhesion Science and Technology*, **22** (2008) 319-334.

41. C. G. L. Furmidge, Studies at phase interfaces I – The sliding of liquid drops on solid surfaces and a theory of spray retention, *J. Colloid Sci.*, **17** (1962) 309-324.

42. J. Zárate, G. Rosas, R. Pérez, Structural transformations of the pseudoboehmite to α-alumina, *AZojomo*, **1** (2005) 1-11.

Chapter 3

Systematic characterization of the effect of uniformly sized and shaped Ag@TiO_2 nanoparticles on the performance of plasmonic dye-sensitized solar cells

3.1 Introduction

Dye-sensitized solar cells (DSSCs) have evolved as credible alternative to conventional solid state p-n junction photovoltaics, with their core advantages of facile & low-cost fabrication, environmentally friendly, and good performance under lowlight conditions [1-4]. The highest power conversion efficiency (PCEs) of the DSSC is between 11 and 13 % [5-6], since its research boom in 1991, when M. Gratzel & B. Oregon obtained an unprecedented PCE of about 7 %, using a nanoporous TiO_2 photoanode [7]. Although groups like G24, Sony and Aisin Seiki have commercialised DSSC for niche markets [8, 9], however, an estimated PCE ≥ 20 % is necessary for commercial high-power applications and utility-scale power generation [2]. A key factor to increase the PCE is to increase the light absorbance of the photoanode of the DSSC. This approach includes designs such as: large surface area mesoporous photoanodes; hierarchically nano-structured & scattering top-layer photoanodes; design of new panchromatic absorbing dyes; photonic crystal photoanodes and plasmonic photoanodes [10]. Among these, the plasmonic photoanodes have the critical advantages of: a) facile preparation; b) use of less photoanode materials; and c) the high potential of extremely enhanced light absorbance via the localized surface plasmon resonance (LSPR) effect [2, 3, 11], through radiative and non-radiative mechanisms of plasmon energy transfer [2]. However, the highest enhanced plasmonic DSSC PCE is still < 11% [2]. This is mainly because of the secondary effects of plasmonic nano-structures on the electron dynamics of the DSSC, apart from their light absorbance enhancement effect. Thus, the need for the

understanding of these secondary effects for the optimal application of plasmonic nano-structures to significantly increase the PCE of the DSSC.

Villanueva-Cab et al. [12] investigated the assumption that bare plasmonic metal NPs work as recombination centres in plasmonic DSSCs with the intention to improve the lack of clear understanding of the charge transfer kinetics in plasmonic DSSCs. They used 3.6 µm-thick TiO_2 photoanodes with different amounts of ~ 2 mM colloidal Au (~ 20 nm) solution impregnation (Au1, Au4 & Au5; which are 1, 4 and 5 rounds of 20 µL of the colloidal Au treatments, respectively). They observed that the dyed photoanodes recorded lower light absorbances than the reference, except for Au1, in the visible region, but recorded higher absorbances in the near-infrared region. Their current-voltage (I-V) characterization showed lower and decreasing short-circuit current density (J_{sc}) and lower open-circuit voltage (V_{oc}) than the reference, although Au5 showed higher values than Au4. Small perturbation measurements showed lower and decreasing recombination constant, charge transfer resistance (R_{ct}) and electron life time (τ_n) than the reference sample. Charge collection efficiency (η_{cc}) was said to be constant. They concluded that Au NPs acting as recombination centres cannot fully explain photovoltaic behaviours of DSSCs; and that variations in J_{sc} and V_{oc} were caused by decreasing charge injection efficiency (η_{inj}) due to upward conduction band (CB) shift in TiO_2 from the effect of the Au NPs.

Choi et al. [13] reported that plasmonic NPs in DSSCs have two effects: the plasmonic (light absorbance enhancement) and charging (electron dynamics) effects. They used Au NPs with two different cappings: SiO_2 (an insulator to prevent electron charging of the Au core) and TiO_2 (a semiconductor that would allow transfer of electrons to charge the Au core). They observed enhanced absorbance with a consequent increase in J_{sc} in both samples, with accompanying increase in V_{oc} in the TiO_2-capped sample. There was no significant change in V_{oc} in the SiO_2-capped sample, although it recorded the higher J_{sc}. The increase in V_{oc} was the

result of the Au NPs accepting electrons from TiO_2 shell and TiO_2/dye and undergoing fermi level equilibration (charging effect). They also studied the plasmonic effects on the cell performance parameters with five loading concentrations (0.2 – 1%). Their results showed no significant effect on fill factor (*FF*) but an effect of decreasing J_{sc} at loading concentrations > 0.7 %, which they suggest was probably due to filtering effects of the Au core.

Qi et al. [14] observed the enhancement effect on light absorbance, and a resultant enhanced J_{sc} and PCE. They observed the major plasmonic NPs enhancement effect on incident photon-to-current efficiency (IPCE) in the wavelength region of 400-500 nm, where the LSPR peak of their NPs is located. They were also able to reduce photoanode thickness and still obtained a higher PCE. They did not observe any significant difference between the *FF* and V_{oc} values of the pristine and plasmonic DSSCs. They however, observed decreased J_{sc} and PCE at higher (> 0.6 %) plasmonic doping conc., which they suggested was probably due to increased trapping of photogenerated electrons by Ag and conversion of part of the incident solar power into heat.

In our laboratory, using bare Ag NPs-filled TiO_2 nanotube plasmonic DSSCs, fabricated with various growth techniques and NPs-loading approaches [15, 16, 17], we observed enhanced light absorption, J_{sc} and PCE. We also observed increased V_{oc} and *FF*, but in one study with electrochemical impedance spectroscopy (EIS) evaluation, we observed a reduction in R_{ct} and τ_n [15].

From the above review, there are significant variations in these reported results on the effects of plasmonic NPs in DSSCs, barring the differences in the DSSC types employed; and somewhat inconclusive results, suggesting the need for more systematic studies on the effects of plasmonic NPs on the performance of DSSCs. We think this is because of the use of limited characterizations with fewer and short-range doping plasmonic concentrations.

In this work of chapter 3 we have used extended characterizations (optical absorption; photoluminescence spectroscopy (PL); I-V; EIS and IPCE); and wider range of plasmonic NPs doping concentrations (0.1, 0.25, 0.5, 1 and 5 %), offering a high dynamic range. In addition, we employed a systematic approach, to obtain a more in-depth understanding of the effects of plasmonic NPs on the performance DSSCs, in addition to the synergistic effect of these effects. We used Ag@TiO_2 core-shell (C-S) NPs-doped TiO_2 pastes and a pristine un-doped paste as a reference, for the fabrication of our photoanodes/DSSCs. We observed two optimally enhanced PCEs: at 0.1 and 1 % doping concentrations, with the dominant plasmonic enhancement effects of optimal band alignment for efficient charge injection on one hand; and an optimal balance of the charge carrier intercalation/dynamics on the other hand, respectively. We also observed some various general effect-trends of the plasmonic NPs on the various cell performance parameters.

3.2 Experimental

3.2.1 Synthesis of Ag@TiO_2 NPs.

The C-S NPs were prepared using a facile solution process with Pluronic P123 as a dispersing agent, in an air-tight 1 L polyethylene terephthalate container covered with an Al foil. In a typical reaction 3.11 g of Pluronic P-123 (Aldrich; PEG-PPG-PEG, avg. M_n ~ 5800) was dissolved in 215.25 ml 1-butanol (Wako; dehydrated, 99.0 %) by stirring on a hot plate with a magnetic stirrer, at ambient temperature, at 500 rpm for 10 min. A 3.585 ml of 0.5 mol L^{-1} $AgNO_3$ (Wako; 99.8 wt.%) was added, in drops, with continuous stirring for another 1 h. The solution was sonicated for about 5 min and 3.585 ml of 1 mmol L^{-1} of L(+)-Ascorbic acid (Wako; 99.6 wt.%) was added with continuous stirring for another 1 h. A second solution of made of 1.02 g of titanium tetraisopropoxide (Wako; 95.0 %) in 322.5 ml 1-butanol, chelated with 0.234 ml acetylacetone (Wako; 99.0 wt.%) in 18 ml 1-butanol, was

added and stirred for a further 10 min An extra solution of 3.75 g of Pluronic P-123 in 37.5 ml 1-butanol was then added and stirred for 20 min, with a subsequent 5 min sonication. The temperature of the hot plate was set to 70 °C and the reaction mixture stirred at this temperature for 1h. After this, Ag@TiO_2 NPs sol was aged at 60 °C for 1 week, by which time the C-S NPs had settled at the bottom of the container. The supernatant solution was decanted off and the residue heat-treated at 80 °C into a gel. The gel residue was further heat-treated at 350 °C for 1 h, based on thermogravimetric-deferential thermal analysis (TG-DTA) results, to obtain the pure Ag@TiO_2 NPs. This is the result of an optimized synthesis process to obtained a desired ~ 20 nm size C-S NPs.

3.2.2 Pastes & photoanodes preparation.

The pastes for the photoanodes fabrication were prepared using a planetary ball miller (Fritsch pulverisette 7) with alumina mortar and balls. For the pristine, *n*-doped, paste (0 %), 1.74 ml of ethylene glycol (dehydrated, Wako; 99.5% min.) was added to 1.0 g of TiO_2 P25 (Sigma-Aldrich; 21 nm; ≥ 99.5%) and then milled at 500 rpm for 1 h. After that 1.69 g Citric acid (Chameleon reagent; anhydrous, ≥ 99.5%) was added and milled again for another 1 h. For the Ag@TiO_2 C-S NPs-doped pastes, the same preparation procedure was used with the appropriate mass of Ag@TiO_2 replacing the appropriate amount of TiO_2 P25 to obtain the doped pastes (0.1, 0.25, 0.5, 1 & 5 %).

The photoanodes were prepared via a doctor blade coating on fluorine-doped tin oxide (FTO)-on-glass substrates (85% T, 9 Ω/□; 3 x 2 cm). The FTO substrates were first cleaned by RCA treatment and coated with a TiO_2 buffer layer via treatment in 0.04 mol L^{-1} $TiCl_4$ (Wako; 99.0% min.) solution at 70 °C for 30 min (with 2 cm^2 active area masking), washed with water and heat-treated at 450 °C for 1 h. The pastes were coated on the FTO substrates using 60 μm scotch tape masks with a circular active area of 0.785 cm^2 (10 mm diameter) each. For uniformity and reproducibility, the doctor blade was kept at a constant distance

over the substrate and an 80 g weight of a 5 x 5 cm steel blocked applied on it to make contact with the substrate. The blade was drawn at a rate of 2.5 mm s^{-1} to spread the paste. The samples were dried sequentially on a hot plate at ambient temperature, 60 °C &120 °C, for 5 min each, and finally heat-treated at 500 °C for 1 h. The calcined samples were washed with ethanol and dried with a hot blower. For dye sensitization, the dried samples were immersed in a 0.3 mmol L^{-1} of N719 dye (ALDRICH; 65 mol% dioxole), in a 1:1 solvent system of acetonitrile (Wako; 99.5 m/m%)-tert-butyl alcohol (Wako; 99.0 %), for 24 h. The dye-sensitized photoanodes were rinsed with acetonitrile to remove excess dye, and dried using a hot blower.

3.2.3 Assembling of DSSCs.

Sandwich-type cells were prepared using a 50 μm plastic spacer (DuPont, Himilan) with an open area of 1.13 cm^2 (12 mm diameter). The dye-sensitized photoanodes were sealed to platinized counter electrodes by heating on a hot plate at 105 °C, with a 1 kg weight load, for about 5 min. The counter electrodes were prepared using RCA-cleaned FTO substrates with drilled holes, 12 mm apart, with Pt coating using a sputter coater (Hitachi E-1030 ion sputter) at 15 mA for 600 s. An acetonitrile solvent based electrolyte, composed of 0.05 mol L^{-1} iodine (Aldrich; ≥ 99%), 0.1 mol L^{-1} lithium iodide (Strem Chemicals; anhydrous, 98 % min.), 0.6 mol L^{-1} 1, 2-dimethyl-3-propylimidazolium iodide (TCI; > 98 %), and 0.5 mol L^{-1} 4-tert-butylpyridine (Aldrich; 96 %), was injected into the cell and sealed with a piece of the spacer and scotch tape. DSSCs with Ag@TiO_2 plasmonic NPs doping concentrations of 0.1, 0.25, 0.5, 1 & 5 %, in addition to a reference un-doped DSSC, 0 %, were obtained.

3.2.4 Characterization.

The optical absorption characteristics of the plasmonic NPs and photoanodes were evaluated using a JASCO V-670 UV-Vis-NIR spectrophotometer. The particle size, size distribution and core-shell structure of the Ag@TiO_2 C-S NPs were observed using a JEOL JEM-2100 F

TEM. A Rigaku Ultima IV R285S XRD was used to study the composition and crystallinity of the Ag@TiO_2 C-S NPs. PL spectroscopy of the photoanodes was evaluated using a He-Cd laser (325 nm) as the excitation source. The luminescence was evaluated by a multi-channel CCD spectrometer. The PL properties were measured using a single monochromator containing a grating and a CCD-array. The I-V characteristics of the cells were evaluated using ADCMT 6244 DC Voltage/Current Source/Monitor and an HAL-320 W solar simulator (Asahi spectra) with a 300 W xenon lamp and an air-mass 1.5 global filter. The solar simulator was calibrated to an intensity of 100 mW/cm^2 (1 sun), using a 1 SUN checker (Asahi CS-40). The IPCE characterization was done via a DC method, using Bunkoukeiki SM-250KB spectrometer with a Keithley 2401 source meter with an irradiation flux of 2.0 x 10^{15} photons, with masking active area of 1 cm^2. A Hitachi S-4800 FE-SEM was used to study the morphology and thickness of photoanode coatings. The electron transport dynamics of the photogenerated electrons was evaluated via an EIS equipment (Solartron SI 1287 Electrochemical Interface and Solartron1255B Frequency Response Analyzer) under bias of the open circuit voltage, V_{oc}, within a frequency range of 0.1 Hz to 1 MHz, and an ac amplitude of 40 mV; and under a light irradiation of 100 mW/cm^2.

3.3. Results and discussion:

3.3.1 Morphology & composition of Ag@TiO_2 C-S NPs.

We synthesized the Ag@TiO_2 NPs via a sol process, using Pluronic P-123 as a dispersing agent. Fig. 3.1 a) shows the TEM image of uniformly sized NPs of about 20 nm, after 350 °C heat treatment (HT). The targeted 20 nm particle size achieved was to closely match that of the main photoanode material of TiO_2. This was to minimize the effect of doping NPs on the surface area of the mesoporous photoanodes. Thermal analysis of the C-S NPs gel and that of Pluronic P-123 showed combustion of the Pluronic P-123 dispersant at ~ 264 °C, and hence, the HT at 350 °C to obtain the pure Ag@TiO_2 C-S NPs. Figure 1(b) is the HRTEM image

showing the TiO_2 shell with an avg. thickness of ~ 2 nm, which is essential for the protection of the plasmonic Ag core from the high temperature processing of the photoanode; corrosive effect of the cell electrolyte; as well as allow for the transmittance of the LSPR effect of the Ag core to vicinal dye and TiO_2 NPs.

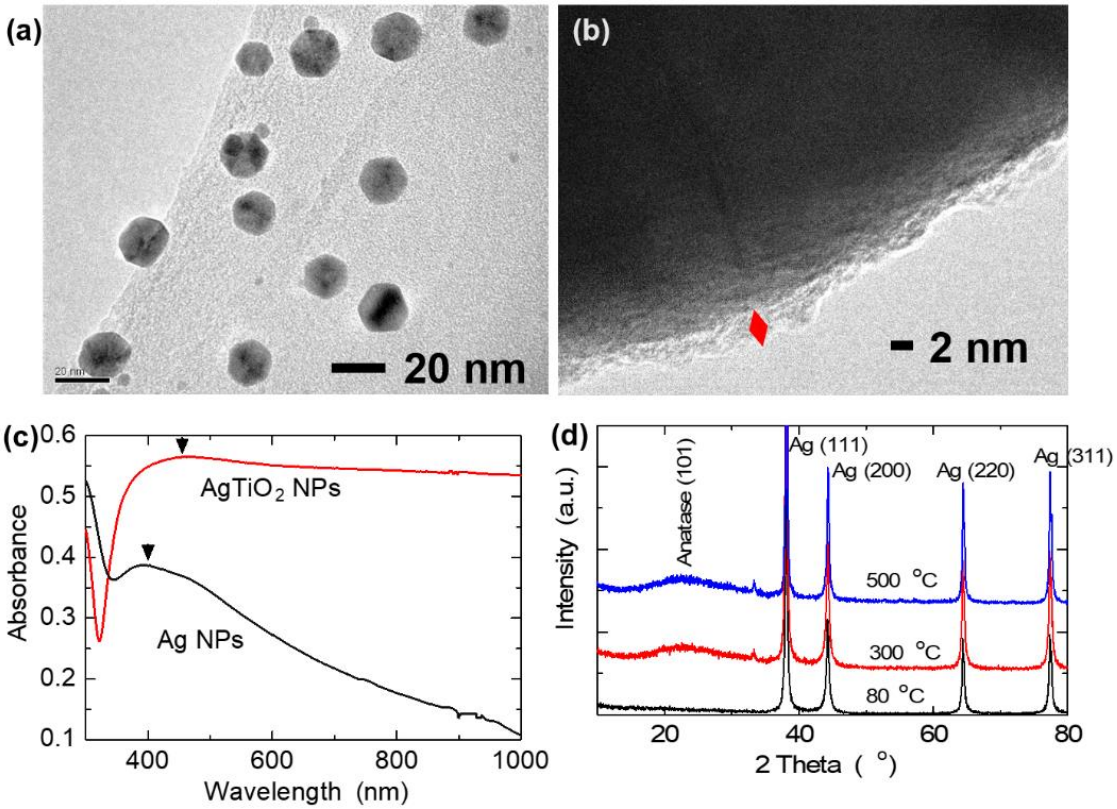

Figure 3.1 a) TEM image of Ag@TiO_2 NPs after 350 °C HT. **b)** HRTEM of the Ag@TiO_2 NPs showing the thin TiO_2 shell. **c)** Optical absorption spectra of Ag and Ag@TiO_2 NPs showing a red-shift in the LSPR peak position, indicating the formation of the C-S structure. **d)** XRD patterns of the Ag@TiO_2 NPs at various HT temperatures showing an amorphous shell, as prepared, and crystallization into the anatase phase after 350 °C.

To investigate the formation of the plasmonic Ag and Ag@TiO_2 NPs, we studied the optical absorption characteristics of these NPs, Fig. 3.1 c). We observed the characteristic red-shift in

LSPR peak position, from 404 nm of the Ag NPs to an estimated peak at 472 nm of the broadband spectrum of the Ag@TiO_2 NPs. The peak shift and enhanced absorbance, with extended absorbance into the near-infrared (NIR) region, are attributed to the higher refractive index of the TiO_2 shell with undulating structure. This anisotropic shell structure would increase polarizability, ultimately resulting in different LSPR modes and multiple plasmon resonances [2]. Typically, a broadband light absorbance is achieved by using bimetallic or rod-like structures [2, 18]. However, we have achieved this using a single capped metal nanosphere. We investigated the composition and crystalline structure of our C-S NPs using X-ray diffraction (XRD) characterization. The as-prepared C-S NPs after the first HT at 80 °C showed diffraction patterns of cubic Ag (111), (200), (220) & (311) planes (JCPDS no. 04-0783), Fig. 3.1 d). There were no observed TiO_2 peaks, suggesting an amorphous TiO_2 shell in the as-prepared C-S NPs.

At 350 °C HT and beyond, the diffraction pattern from the (101) and (004) planes of anatase phase TiO_2 were observed, with additional peaks of the (103) and (112) planes observed after 500 °C HT (JCPDS no. 21-1272), Fig. 3.1 d). The broad (101) anatase plane peak is attributed to the small crystallite size and/or crystalline strain.

3.3.2 Corrosion stability and optical enhancement effect of the plasmonic Ag@TiO_2 NPs.

One of the functions of the TiO_2 shell is to protect the Ag core from the corrosive effect of the I^-/I_3^- electrolyte. To investigate this, we performed an acid stability test via optical absorbance spectroscopy. The results are shown in Fig. 3.2 a & b). Comparing the absorbance spectra of the Ag NPs solutions in Fig. 3.2 a), the LSPR peak disappears in the spectrum of the acid treated sample, with accompanying drastic decrease in absorbance intensity, indicating the dissolution of the Ag NPs. This is confirmed visually in the inset image, which shows a light brown colloidal solution of the Ag NPs, of the sample without acid treatment (left), but a clear solution of the acid treated sample (right). However, in the case of the

Ag@TiO_2 NPs, the inset image of Fig. 3.2 b), there is no observed difference between the sample without acid treatment (left) and the acid-treated sample (right).

Comparing their optical spectra, there is no loss of absorbance intensity in the acid-treated sample, indicating that the TiO_2 shell protects the Ag core from corrosive effects. The apparent increase in absorbance in the acid-treated sample is probably due to a dilution effect of the acid treatment causing a constructive interaction effect of the different plasmon modes [19]. To further consolidate these results we also tested the stability of the C-S NPs in the I^-/I_3^- electrolyte (2.2 mg PNPs in 3 mL electrolyte). The results are shown in Fig. 3.2 c), with spectra of the electrolyte and C-S PNPs only (2.2 mg in 3 mL acetonitrile (solvent for the electrolyte)) for comparison. As can be seen, there is no significant change in absorbance of the C-S PNPs-electrolyte mixture spectrum, even after 24 h, especially in the NIR region where the spectrum of the mixture matches that of the C-S NPs only. That is, if there were dissolution of the PNPs, the absorbance of the mixture would have been lower than the spectrum of the C-S NPs only.

Recombination of photogenerated electrons during their transport within the mesoporous nanocrystalline TiO_2 network of DSSCs is one of the major factors that contributes to the inefficient performance of DSSCs. Metalic nanoparticles have been reported to exhibit electron-sink (or photocharging) effect [13, 20-22], and thus, the potential to minimize charge recombination. A suitable technique for investigating this electron-sink effect is PL spectroscopy, which studies photon emissions resulting from electron-hole recombination. Anatase is an indirect band gap material and hence, should not exhibit PL. However, it has intrinsic oxygen vacancies (responsible for its *n*-type semiconducting properties) [22], which generate different kinds of electron and hole traps, randomly distributed within its forbidden band gap. This creates various transitions, resulting in the typical broadband visible PL spectrum of TiO_2 [23], as observed in our results in Fig. 3.3 a).

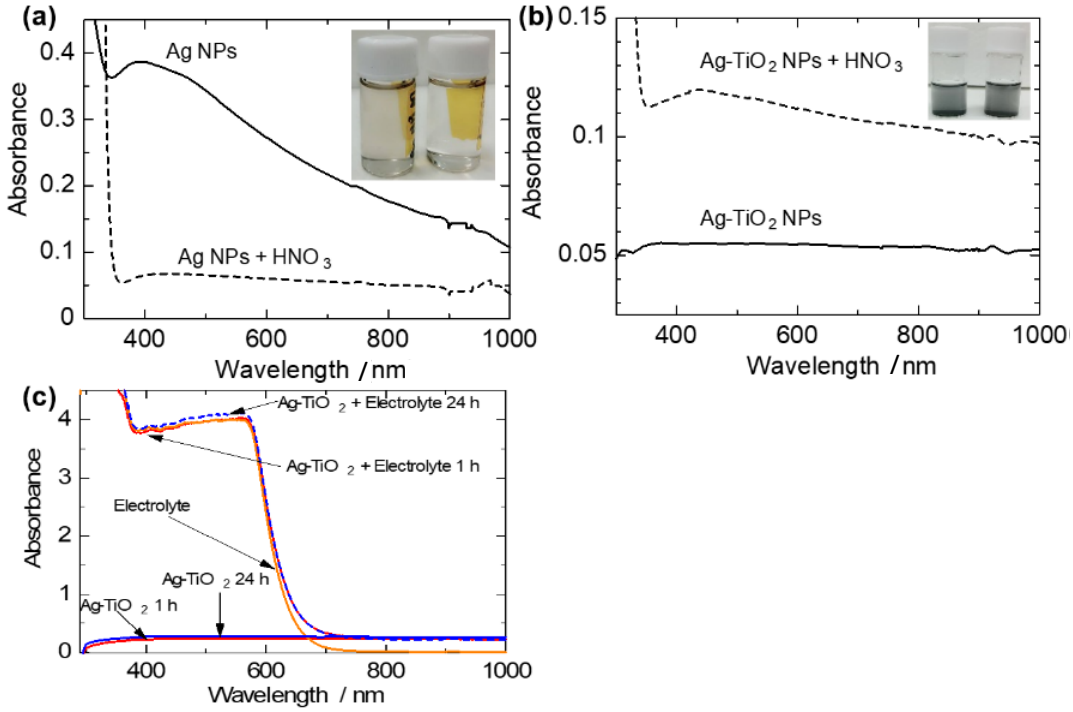

Figure 3.2 a) Optical absorption spectra showing the dissolution of Ag NPs in acid; inset is a visual image of the test samples; without acid (left) & with acid (right) treatment. **b)** Optical absorption spectra showing corrosion stability test of Ag@TiO_2 NPs via acid treatment; inset is a visual image of the test samples; without acid (left) & after acid (right) treatments. **c)** Absorbance spectra showing stability of the Ag@TiO_2 C-S PNPs in I^-/I_3^- electrolyte.

The generally low PL intensity observed in our samples is attributed to the mesoporous and thin film (6.5 μm) characteristics of our samples, as reported by Mercado et al. [24]. In Fig. 3.3 a) the PL intensity decreases with increasing amount of Ag@TiO_2 doping, indicating that the excited electrons are captured by the core Ag NPs before they recombine, causing the so called electron-sink effect. This causes the accumulation of electrons on the Ag NPs, which improves electron life time and can thus, reduce charge recombination, ultimately, improving electron transport.

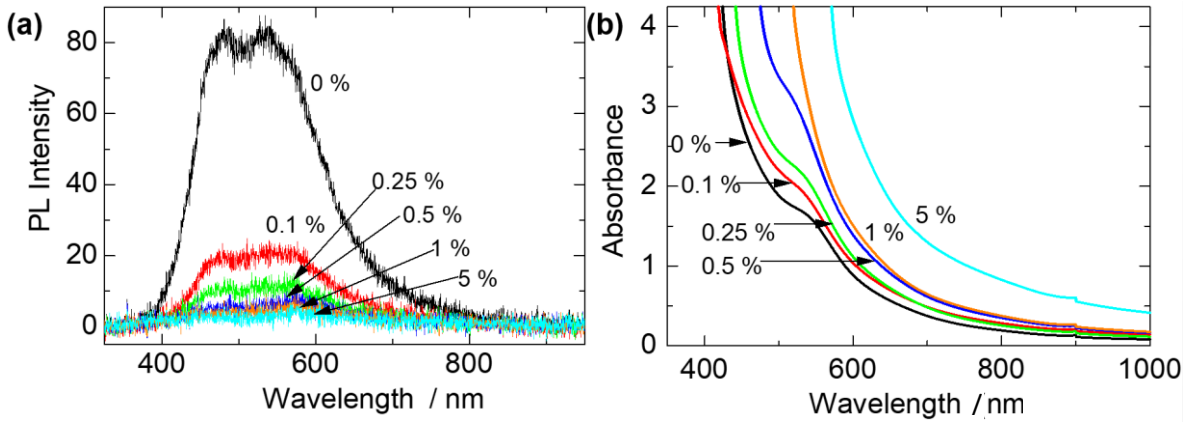

Figure 3.3 a) PL spectra of photoanodes showing the electron-sink effect via decreasing PL intensity with increasing amount of Ag@TiO_2 NPs doping. **b)** Optical absorption spectra showing enhanced broadband light absorbance in the Ag@TiO_2-doped photoanodes.

To investigate the LSPR effect on the light absorption enhancement of dye molecules of the DSSC photoanode, we measured the optical absorbance of dye-sensitized plasmonic photoanodes and compared them to that of the reference un-doped photoanode. The results are shown in Fig. 3.3 b). The plasmonic photoanodes recorded higher absorbances than the pristine photoanode. This is a typical result in many reported works on plasmonic DSSCs. The absorbance increased with increasing amount of doping, with an analogous increasing effect in the NIR region. All photoanodes were of the same average thickness of 6.6 ± 0.1 µm. Thus, the increasing absorbance could only be attributed to the LSPR effect of the plasmonic NPs.

To further investigate the light absorbance enhancement effect of the plasmonic NPs on the dye, we studied the optical absorption patterns of various dye-plasmonic NPs compositions in solution. This was to simulate the plasmonic enhancement effect of the PNPs on the dye

without the possible interference effects of other components of the photoanode or complete DSSC. The results are shown in Fig. 3.4. As can be observed in Fig. 3.4 a), the plasmonic NPs-spiked dye solutions (green and blue spectra) both showed enhanced light absorption over the pristine dye and plasmonic NPs (black and red spectra, respectively).
The quantum of enhancement further increased with the increase in amount of plasmonic NPs, indicating the LSPR light absorption enhancing effect on the dye.

We also studied the synergistic effect of the dye-plasmonic NPs in the enhancement by comparing the absorption spectra of an arithmetic addition of the separate absorbances of the pristine dye and plasmonic NPs on one hand (orange spectrum), to the absorption spectra of the plasmonic NPs-spiked dye solutions. The spectra of the spiked dye solutions matched each other, with blue-shift in absorption peaks, compared to the pristine dye, whiles they differed from the spectrum of the arithmetic sum (orange spectrum), which matched that of the pristine dye. This spectrum also showed lower absorbance than the spiked dye spectra, although it had much higher plasmonic NPs concentration. These results show a synergistic effect between the dye and plasmonic NPs, on the light absorption enhancement effect. This peak shift has been observed in the reported works of Qi et al. [14] and Choi et al. [13]. Whiles Qi et al. studied the enhanced absorbance with respect to time, where they observed increasing absorbance over time, but without further peak shift. They did not explicitly state the cause of the peak shift, but attributed the enhanced absorbance over time to increasing layering of the dye molecules on plasmonic

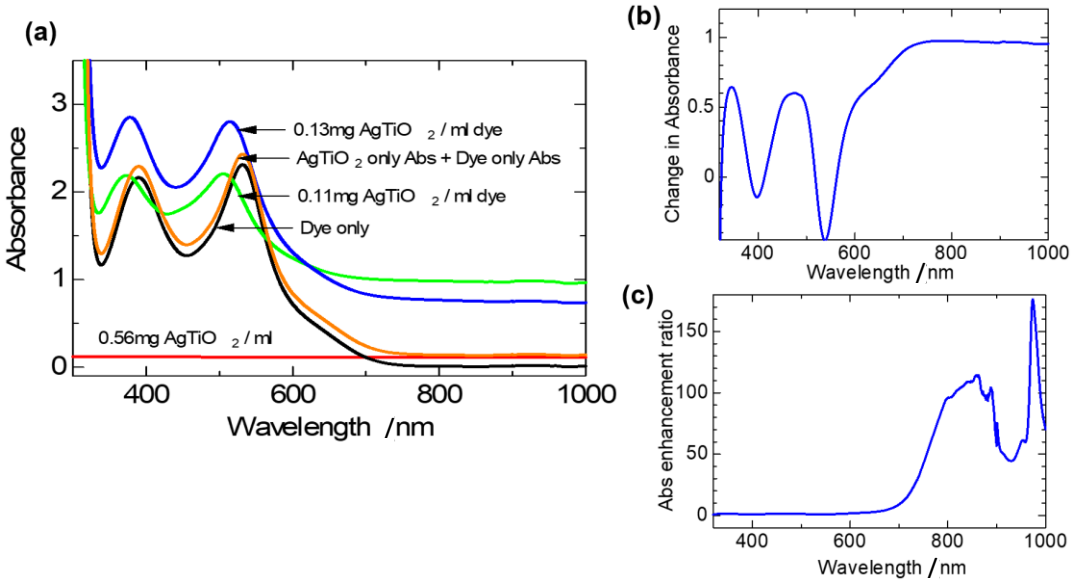

Figure 3.4 Optical absorption spectra showing enhanced broadband light absorbance of the N719 dye: **a)** separate dye and plasmonic NPs; dye plus plasmonic NPs mixtures; and arithmetic addition of dye and plasmonic NPs absorbances. **b)** Absorbance of [0.12 mg ml^{-1} dye] – absorbance of [dye-only]. **c**) Absorbance of [0.12 mg ml^{-1} dye] ÷ absorbance of [dye-only].

NPs, with consequent increase in proximity of layered dye molecules to neighbouring plasmonic NPs. Choi et al. attributed their observed peak shift to excitation of the TiO_2 semiconductor shell. Their results showed no peak shift in SiO_2-capped Au NPs (SiO_2 is an insulator) but a continuous peak shifting, in the TiO_2-capped Au NPs (TiO_2 is a semiconductor). Also there was no peak shift in aerated solution but peak shift in de-aerated solution. In our work, we sonicated the solutions for about 15 min and measured the optical absorbance within 30 min to1 h, storing our samples mainly in the dark. Thus, we attributed our observed peak-shift to layering of dye molecules on the plasmonic NPs, modifying the

LSPR of the NPs by coupling with the plasmon and causing the observed blue-shift, analogous to the red-shift effect of TiO_2 capping.

We also studied the effective enhancement effect of the plasmonic NPs by deducting the absorbance of the pristine dye from that of the spiked dye (Fig. 3.4 b)), and also dividing the absorbance of the spiked sample over that of the pristine dye (Fig. 3.4 c)). From Fig. 3.4 b) it can be observed that the enhancement effect is complementary, enhancing the dye absorbance in its poorly absorbing regions of the electromagnetic spectrum. In Fig. 3.4 c) a similar trend is observed, with an average of x100 enhancement in the NIR region. Thus, our plasmonic NPs achieved a broadband optical absorption effect with the major enhancement effect in the regions where the dye exhibits weak absorbance.

3.3.3 Effect of plasmonic NPs on DSSC performance.

To investigate the effect of these plasmonic NPs on the performance of the DSSC we assembled the prepared photoanodes into plasmonic DSSCs and evaluated their I-V characteristics to compare their performance to the pristine reference cell (0 %), and to each other. Figure 3.5 shows the results of their effects and effect trends on the Brunauer–Emmett–Teller surface area (BET SA) and photovoltaic performance parameters of the cells. The first 6 columns of Table 3.1 is a quantitative summary of these results. From Fig. 3.5 a) we observe nominal and consistent decrease in SA with increasing amount of plasmonic NPs doping, from 3.7 % decrease at 0.1 % doping to 25.5 % decrease at 5 % doping. We think that this decreasing SA is due to the initially amorphous state of the TiO_2 shell of the plasmonic NPs; such that during the heat treatment there is increased necking between the TiO_2 shell and TiO_2 P25 NPs, decreasing SA. This decrease in SA was expected to obviously reduce dye loading in the photoanodes, with a consequent decrease in light harvesting.

However, we obtained (3.50, 3.51, 3.51, 3.53 and 3.54) * 10^{-8} moles cm^{-2} dye loadings for the photoanode samples of 0, 0.1, 0.25, 0.5, 1 and 5 % plasmonic NPs loadings, respectively.

Thus, the decreasing SA effect of the plasmonic NPs do not significantly affect the amount of dye absorbed for the thickness of the coated photoanodes in this work. This apparent deviation from what was expected is explained to be due to one or two reasons: a) possible minute amount of leaching of plasmonic NPs into the soaking dye causing higher absorbance reading than should be, and a resultant false higher dye loading; b) the modification of trap states on the surface of the TiO_2 NPs catalyzing enhanced dye absorption. However, the verification of these explanations is beyond the scope of this work. The dye loading results were obtained via optical spectroscopy by deducting the absorbance of the 10 mL dye solution in which each photoanode was soaked from the absorbance of the dye before the soaking. A repeat of this analysis using the more common "1 mol L^{-1} NaOH dye desorption method" was also used and very similar results were obtained.

Figure 3.5 b) is the I-V spectra of the cells, with sample 0.1 % recording the highest J_{sc} and the lowest V_{oc}, whiles sample 5 % records the lowest J_{sc} and the highest V_{oc}. Figure 3.5 c-f) are the extracted I-V parameters. In Fig. 3.5 c) we observe an increase in J_{sc} at 0.1 % doping, a decrease afterwards, and then a slight increase again at 1 % doping, and a return to the decreasing trend. The general observation trend in many reported plasmonic DSSC works (e.g. review work of Erwin et al. [2] and works of Qi et al. [14] and Lim et al. [22]) is an increase in J_{sc} to an optimal value and a decrease afterwards. Nevertheless, Ramakrishna *et al.*'s simulation work on electron injection in plasmonic metal@semiconductor C-S-dye DSSCs [25] predicted the possibility of multiple optimal performances in charge injection.

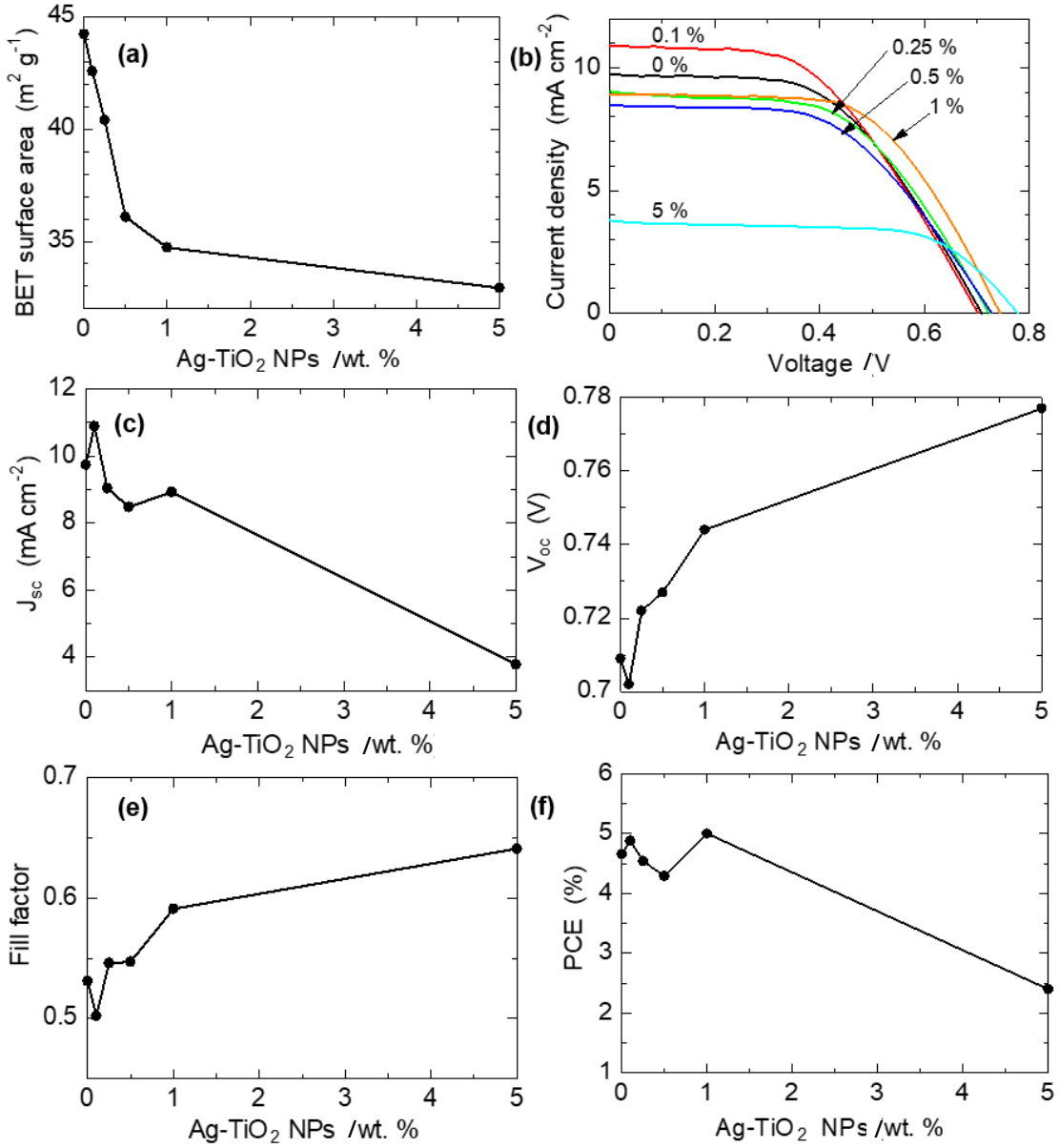

Figure 3.5 Plots of plasmonic NPs doping effects on the surface area and photovoltaic performance parameters on DSSCs: **a)** Surface area; **b)** I-V; **c)** J_{sc}; **d)** V_{oc}; **e)** *FF*; (f) PCE.

The main factors that contribute to high J_{sc} are good light absorbance to generate charge carriers, their efficient injection and transport in the photoanode. From Fig. 3.1 d), we observed increased light absorbance of the plasmonic photoanodes over the pristine

photoanode, with increasing intensity as plasmonic NPs content increased, despite their reducing SA. This indicates an overshadowing effect of the LSPR effect over the reducing SA effect.

Table 3.1: Effect of plasmonic NPs on the photoanode surface area and extracted I-V & EIS parameters.

Amt. of Ag@TiO_2 /wt. %	BET SA /$m^2\ g^{-1}$	J_{SC} /mA cm^{-2}	V_{OC} /V	*FF*	PCE /%	R_S /Ω	R_{CT} /Ω	τ_n /ms	η_{CC} /%
0	44.2	9.74	0.709	0.531	4.66	20.1	4.8	5.04	19.3
0.1	42.6	10.89	0.702	0.502	**4.88**	20.8	4.2	4.00	16.8
0.25	40.4	9.04	0.722	0.546	4.54	20.6	7.1	5.04	25.6
0.5	36.1	8.48	0.727	0.547	4.29	22.1	10.4	6.34	32.0
1	34.7	8.93	0.744	0.591	**5.00**	20.0	7.1	6.34	26.2
5	32.9	3.78	0.777	0.641	2.40	21.7	15.8	12.63	42.1

Thus, the highest J_{sc} obtained at 0.1 % doping can be attributed to efficient generation, injection and transport of charge carriers. Most significantly, it reveals that the most significant enhancement is efficient charge injection, as evidenced in its reduction in V_{oc} value in Fig. 3.5 d) and Table 3.1, compared to that of the pristine sample. This is further explained as follows: there is a minimal threshold energy gap between the LUMO of a sensitizer and the CB edge of a semiconducting material, below which there is poor charge injection efficiency [27, 28]. In addition, the V_{oc} can be described simply as the difference between the fermi level of the photoanode and the redox potential of the electrolyte, and hence, the observed V_{oc} change is from the plasmonic NPs-modified photoanode. Thus, at the

0.1 % plasmonic NPs doping of the 6.5 µm thick TiO_2 photoanode, there is a plasmon-photoanode material coupling that induces a lowering of the fermi level of the photoanode, to an optimal level, for efficient charge injection, that ultimately produced the highest J_{sc}. For the rest of the plasmonic NPs-doped samples, we observed a continuous increase in V_{oc} with increasing plasmonic NPs doping, attributed to an upward shift of the fermi level of the photoanode, as a result of the electron-sink effect of charge accumulation by the Ag core NPs, and/or a Bursten-Moss shift effect, from abundantly generated charges. This rising fermi level would lead to poor charge injection efficiency, and hence would account for the decreasing J_{sc} values in the higher doped plasmonic samples. However, at 1 % doping a slight increase in J_{sc} is observed, which is attributed to the positive plasmonic NPs effects on electron kinetics. Thus, although at this relatively higher percentage of plasmonic doping with resultant high light absorbance, Fig. 3.3 b), the poor charge injection efficiency due to the rising fermi level, would lead to lower J_{sc}. Nevertheless, we predicted that due to the electron-sink effect of the core Ag NPs, observed in Fig. 3.3 a), we expected a reduction in charge recombination and improved charge transport, evidenced in the improving *FF* value with increasing plasmonic NPs doping. Thus, this would account for the slight increase in J_{sc}; an optimal concentration for the balance of the negative and positive effects of the plasmonic NPs. In Fig. 3.5 e) and Table 3.1, there is a decrease in *FF* at 0.1 % doping, this is attributed to exponential charge recombination due to either high density of charge carriers in the CB of the photoanode TiO_2 NPs [28] and/or closeness of the CB edge (fermi level) of the TiO_2 to the redox potential, favoring easy charge transfer to the I^-/I_3^- redox couple [30].

The PCE is described as, PCE = (J_{sc} * V_{oc} * *FF*) / P_{in}; where P_{in} is the incident light power per unit area. Thus, the observed variations in the PCEs are from the variations in the values of J_{sc}, V_{oc} & *FF*, which have been discussed above, and hence, explains the analogous PCE results trend observed in Fig. 3.5 f) and Table 3.1.

However, of noteworthy is that although sample 0.1 % generated the highest J_{sc} (due to, mainly, efficient charge injection), it is sample 1%, that records the highest PCE, mainly from the enhanced charge transport kinetics and the optimal balancing of the negative and positive effects of plasmonic NPs on the performance of DSSCs. This is interesting because it would suggest that tuning plasmonic NPs incorporation into DSSCs for efficient light harvesting should not be the only desired effect for enhanced DSSC PCE, but also tuning for the optimal balancing of the positive and negative effects of plasmonic NPs can also achieve enhanced PCE, and should be considered in plasmonic DSSCs.

We also measured the I-V characteristics of the samples 5 days after the first measurement of the prepared DSSCs to study the protective effect of the TiO_2 shell against the corrosive electrolyte in the complete DSSCs. The results for the key parameters are shown in Table 3.2. As can be observed there is no significant difference between the first measurement and the measurement after 5 days, but with the maintenance of the plasmonic effect trend. Thus, our thin TiO_2 shell coating served as an effective protection of the plasmonic Ag core against the corrosive electrolyte. This is significant because other works have suggested the need for thicker shells for effective protection at the expense of significantly reducing the LSPR reach, or the use of complex composite shells coatings [31-33]. This may be due to a very compact layering of the thin shell.

The I-V characterization technique reveals the performance of the solar cell but does not explain the "why" of that performance. EIS is one of the characterization techniques used to study the electron kinetics and charge recombination within the cell, which are responsible for the PCE of the cell. Thus, we evaluated the EIS characteristics of our DSSCs to ascertain the effect of the plasmonic NPs on the electron kinetics of the cells that resulted in the observed I-V characteristics. The results are shown in Table 3.1 and Fig. 3.6.

Table 3.2: Key I-V characterization parameters to show plasmonic DSSC stability after 5 days.

Sample	*Jsc* /mA cm^{-2}	*Voc* /V	*FF*	PCE /%
0%	9.76	0.714	0.530	4.70
After 5 days	9.74	0.709	0.531	4.66
0.1%	10.90	0.696	0.501	4.84
After 5 days	10.89	0.702	0.502	4.88
0.25%	9.00	0.719	0.549	4.52
After 5 days	9.04	0.722	0.546	4.54
0.5%	8.42	0.724	0.537	4.17
After 5 days	8.48	0.727	0.547	4.29
1%	8.96	0.741	0.589	4.98
After 5 days	8.93	0.744	0.591	5.00
5%	3.80	0.774	0.640	2.39
After 5 days	3.78	0.777	0.641	2.40

Figure 3.6 a) is the Nyquist plots of the DSSCs. Basically, there are three semicircles in the Nyquist plots of DSSCs [34] as observed in our results in Fig. 3.6 a). These represent the charge transfer kinetics at the counter electrode, photoanode and electrolyte, corresponding to the high (left), mid and low frequency regions, respectively [35-37]. Our DSSC system has the mid-frequency region at 2.51-631 Hz. From Fig. 3.6 a) it can be seen that there is no

significant difference in the two extreme semicircles (electron kinetics at the counter electrode and I^-/I_3^- species diffusion in the electrolyte) of the DSSC samples, indicating that the plasmonic NPs do not affect the charge kinetics of these components of the DSSCs. In addition, the intercept of the Nyquist plots of the DSSCs at the Z'-axis, at the high frequency end, are almost the same, fluctuating randomly in the range of 20-22 Ω. This intercept point represents the series resistance, R_s, of the cells, arising from the FTO substrates and the external circuit wires.

Thus, their approximately constant value among the samples is understandable because the plasmonic NPs are not in direct contact with these components, and thus, not expected to affect them. However, Lim et al. [21] reported varying R_s in different Ag NPs-doped DSSC samples. This could be due to their use of bare Ag NPs and relatively high amounts of doping (5-40 %). From Fig.3. 6 a), the diameter of the mid-semicircle, generally, increases with increasing amount of plasmonic NPs. This diameter represents the charge transfer resistance against recombination, R_{ct}, at the TiO_2-Dye/electrolyte interface. The plasmonic effect trend on this parameter is shown in Fig. 3.6 b) and Table 1. This general trend of increasing R_{ct} with increasing amount of plasmonic NPs is attributed to the electron-sink effect, which reduces the amount of electrons recombining with electrolyte hole species at the interface. Thus, the electron-sink effect has both a negative and positive effect of reducing charge injection efficiency via upward shift of fermi level and reduction of charge recombination via electron capture, respectively.

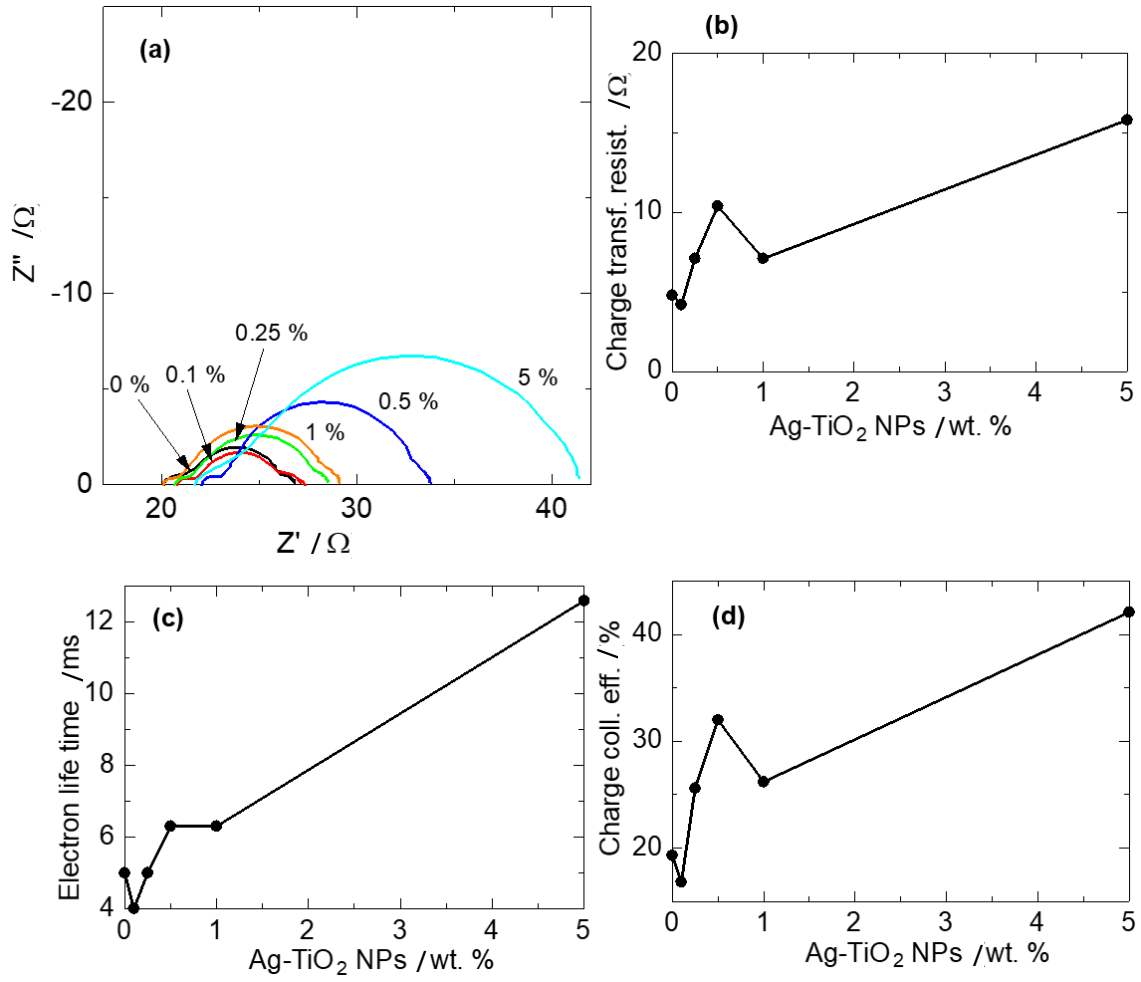

Figure 3.6 Extracted parameter plots from EIS measurement of DSSCs: **a)** Nyquist plots. Change in: **b)** charge transfer resistance, **c)** electron lifetime and **d)** charge collection efficiency, with respect to amount of plasmonic NPs doping.

The two deviations from the general effect trend at 0.1 and 1 % dopings are attributed to increased charge recombination from high charge densities in the CB of TiO_2, as discussed above. Figure 3.6 c) shows the effect of the plasmonic NPs on electron lifetime of charge carriers, τ_n, a measure of charge recombination. It, generally, increased with increasing

plasmonic NPs content, attributed to the electron-sink effect of capturing excited charges by the core Ag NPs. Thus, these plasmonic NPs improved the lifetime of excited charge carriers to improve the recombination characteristics of the cells, as observed in the R_{ct} results. The drop in τ_n at 0.1 % is attributed to the increased recombination as a result of high charge carrier density, in addition to the relatively low amount of plasmonic NPs doping. At 1 % doping, although there is an enhancement of τ_n, the lack of the anticipated increase in value is also attributed to increased recombination as a result of high electron density in TiO_2. The electron lifetime values were obtained from the relation, $\tau_n = 1 / (2\pi f)$ [38], where f is the frequency at the peak point of the mid-frequency semicircle. We also extracted the charge collection efficiency, η_{cc}, to investigate how efficiently the plasmonic NPs affect charge carriers transported from the conduction band of TiO_2 to the back contact FTO. The results are shown in Fig. 3.6 d) and Table 3.1. The values were obtained using the relation, $1 / [1 + (R_s / R_{ct})]$ [38]. Generally, the trend is that, η_{cc} enhanced with an increase in amount of plasmonic NPs. This is also attributed to the electron-sink effect of the core Ag NPs capturing electrons and protecting them from recombination. These captured electrons are released subsequently, in an analogous fashion as the trapping-detrapping electron diffusion transport model of DSSCs. However, there is a deviation to the increasing η_{cc} trend at samples 0.1 % and 1 % by their lower values, compared to those of their immediate preceding samples. These deviations are attributed to the exponential charge recombination in these samples (confirmed in their R_{ct} and τ_n values), as a result of the high charge density in the TiO_2 NPs of these samples. It is also interesting to note that these samples have the lowest η_{cc}s, yet, the highest J_{sc}s, compared to the rest of the samples. This further supports their possession of high charge densities.

In order to investigate the effect of the plasmonic NPs on the cell performance at each wavelength, we evaluated their IPCE performance which is shown in Fig. 3.7. Results in Fig.

3.7 a) show an analogous trend as observed in the I-V characterization performance, and hence, have the same explanations. However, in the UV region, there is a general trend of reducing performance with increasing plasmonic NPs content. This observation is clearly seen in Fig. 3.7 b), obtained from the deduction of the IPCE of the reference cell from those of the plasmonic cells. It shows that the reference pristine cell performs better than the plasmonic DSSCs. This is attributed to the reduction in the effective number of TiO_2 P25 NPs replaced by the Ag in the photoanode as a result of the higher relative atomic mass of Ag than the molecular mass of TiO_2. It also indicates that the plasmonic effect of these NPs does not enhance cell performance in the UV region. Figure 3.7 b) shows that the plasmonic NPs enhance cell performance across the visible and NIR regions, confirming the broadband enhancement effect of our Ag@TiO_2 C-S NPs. However, the highest region of the plasmonic enhancement effect is in the range of 550-720 nm. For the 5 %-doped cell, there is no IPCE enhancement effect from 300-720 nm, which is the active light absorption region of the N719 dye.

The IPCE can also be described as, IPCE = $\eta_{lh}(\lambda) * \eta_{inj}(\lambda) * \eta_{reg}(\lambda) * \eta_{cc}(\lambda)$; where, $\eta_{lh}(\lambda)$ is light harvest efficiency, $\eta_{inj}(\lambda)$ is charge injection efficiency and $\eta_{reg}(\lambda)$ is dye regeneration efficiency. Thus, the non-performance in this region is due to poor charge injection, and/or probably, in addition to poor dye regeneration. However, it clearly indicates that the plasmonic NPs are behaving as direct sensitizers in the NIR region. We further investigated the relative IPCE enhancement effect of the plasmonic NPs by dividing the IPCEs of the plasmonic cells by that of the reference cell. The results are shown in Fig. 3.7 c), with the expanded form shown in Fig. 3.7 d). There is a reversal of the plasmonic NPs enhancement effect on IPCE performance trend, in an observed increasing IPCE enhancement effect with increasing plasmonic NPs content.

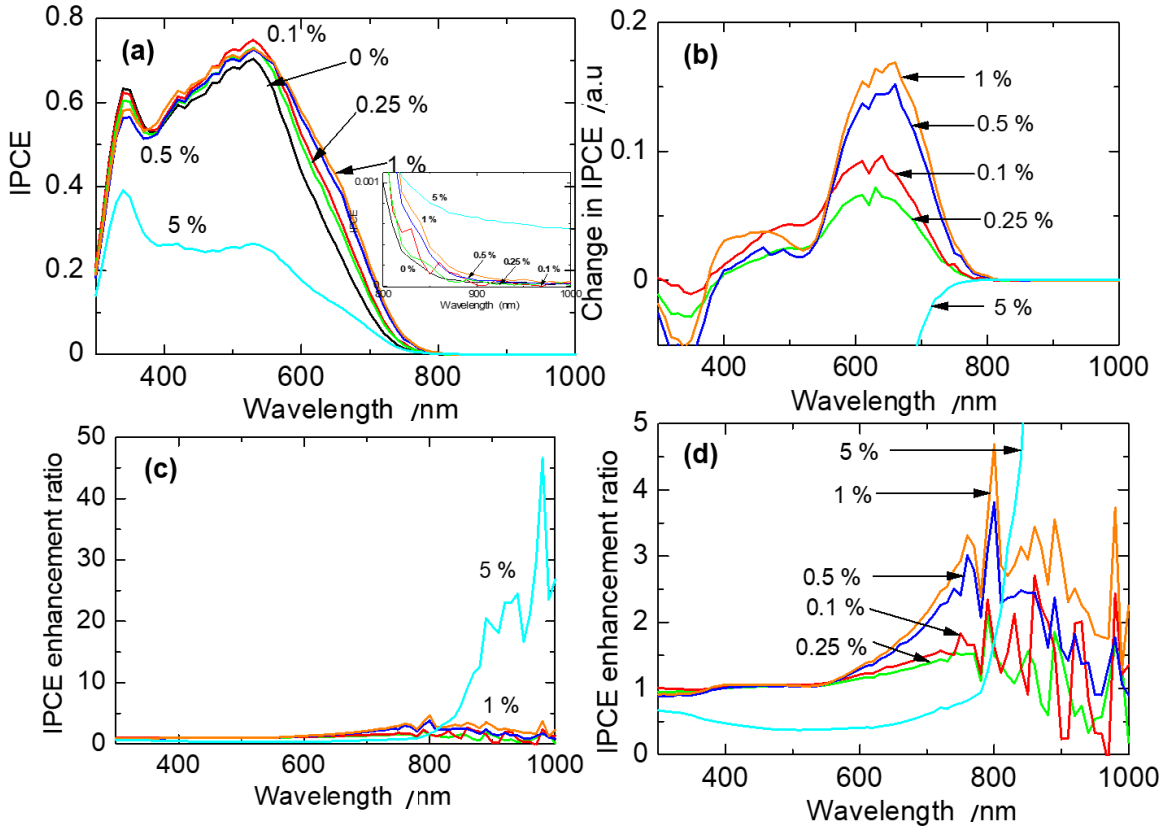

Figure 3.7 a) IPCE spectra of the fabricated DSSCs to show the effect of plasmonic NPs on device performance with respect to wavelength, inset: expanded NIR region to show IPCE activity; **b)** the change in IPCE of plasmonic NPs-doped DSSCs over the pristine DSSC; **c)** the relative change in IPCE of plasmonic NPs-doped DSSCs over the pristine DSSC; **d)** an expanded part of figure c).

3.4 Conclusion

We have successfully prepared Ag@TiO_2 NPs with undulating shell structure, to study the effects of plasmonic NPs on the performance of DSSCs via extended characterization and a systematic approach. These plasmonic NPs had a broadband enhancement effect in their

DSSCs. They enhanced cell performance via four main routes: a) enhancement of light absorption by the N719 dye via their LSPR effect; b) modification of the fermi level of the TiO_2 photoanode for efficient charge injection; c) enhancement in the NIR region by acting as direct sensitizers; and d) balancing the negative and positive electron-sink effects of the core Ag NPs, at optimal doping content, on cell performance parameters of J_{sc}, V_{oc}, FF, R_{ct}, and τ_n. Two optimal doping concentrations were observed with enhanced PCE over a reference pristine cell of PCE of 4.66 %: a) 0.1%; with the highest J_{sc}, with the main enhancement via efficient charge injection, by lowering the fermi level of the TiO_2 photoanode, producing a PCE of 4.88 %; and b) 1 %; with the main enhancement via the electron-sink effect improving cell performance parameters of J_{sc}, V_{oc}, FF and R_{ct}, producing a PCE of 5.00 %. These two samples produced the highest J_{sc}s, respectively, although on the other hand they recorded the lowest η_{cc}s. Thus, the plasmonic NPs exhibited the anticipated characteristics for highly efficient DSSCs, however, the intrinsic exponential charge recombination at high charge carrier density on TiO_2 prevented the realization of making the expected high impact. Nevertheless, with the appropriate modification to harvest the abundant charge carriers generated, this expected impact for highly efficient DSSCs can be achieved. To put it rather simply, if a plasmonic DSSC is designed to harvest the high charge density of electrons induced by the plasmonic NPs, then extremely high PCE can be achieved to meet the desired high expectation of plasmonic DSSCs. In addition, if the fermi level upward shift effect is controlled, then higher plasmonic NPs loaded DSSCs can be prepared, without significant loss to cell performance to inefficient charge injection. This would also increase the cell performance in the energy-rich infrared region of the solar energy flux. Thus, we believe our results might serve as invaluable guide for the preparation of highly efficient plasmonic DSSCs. However, our work is based on just one plasmonic nanostructure, and since the LSPR effect is dependent on the composition, size, environment and shape of the

plasmonic NP. Thus, further studies based on these properties would give a deeper and wider understanding of the effects of plasmonic NPs in DSSCs.

References

1. M. Gratzel, The advent of mesoscopic injection solar cells, *Prog. Photovolt. Res. Appl.* **14** (2006) 429-442.

2. W. R. Erwin, H. F. Zaricka, E. M. Talbert and R. Bardhan, Light trapping in mesoporous solar cells with plasmonic nanostructures, *Energy Environ. Sci.* **9** (2016) 1577-1601.

3. M. Ye, *et al.*, Recent advances in dye-sensitized solar cells: from photoanodes, sensitizers and electrolytes to counter electrodes, *Materials Today*. **18** (2015) 155-162.

4. M. L. Parisi, S. Maranghi and R. Basosi, The evolution of the dye sensitized solar cells from Grätzel prototype to u-scaled solar applications: a life cycle assessment approach, *Renewable and Sustainable Energy Reviews*, **39** (2014) 124 –138.

5. Best research-cell efficiencies. *NREL* https://www.nrel.gov/pv/assets/images/efficiency-chart.png (2017).

6. S. Mathew *et al.*, Dye-sensitized solar cells with 13% efficiency achieved through the molecular engineering of porphyrin sensitizers, *Nat. chem*, **6** (2014) 242-247.

7. B. O'Regan and M. Gratzel, M. A low-cost, high-efficiency solar cell based on dye sensitized colloidal TiO_2 films, *Nature* **353** (1991) 737-740.

8. H. J. Snaith, Perovskites: The emergence of a new era for low-cost, high-efficiency solar cells, *Phys. Chem. Lett.* **4** (2013) 3623–3630.

9. J. B. Baxter, Commercialization of dye sensitized solar cells: present status and future research needs to improve efficiency, stability, and manufacturing, *J. Vac. Sci. Technol. A* **30** (2012) 020801.

10. X-D. Gao, X-M. Li and X-Y. Gan, Enhancing the light harvesting capacity of the photoanode films in dye-sensitized solar cells, *InTech* **DOI 10.5772/51633** (2013) 169-202.

11. S. V. Boriskina, H. Ghasemi and G. Chen, Plasmonic materials for energy: From physics to applications, *Materials Today*, **16** (2013) 375-386.

12. J. Villanueva-Cab, J. L. Montaño-Priede and U. & Pal, Effects of plasmonic nanoparticle incorporation on electrodynamics and photovoltaic performance of dye sensitized solar cells, *J. Phys. Chem. C* **120** (2016) 10129-10136.

13. H. Choi, W. T. Chen and P. V. Kamat, Know thy nano neighbor: plasmonic versus electron charging effects of metal nanoparticles in dye-sensitized solar cells, *ACS Nano*, **6** (2012) 4418–4427.

14. J. Qi, X. Dang, P. T. Hammond A. M. Belcher, Highly efficient plasmon-enhanced dye-sensitized solar cells through metal@oxide core-shell nanostructure. *ACS Nano.* **5** (2011) 7108-7116.

15. X. Wei, S. P. Nbelayim, G. Kwamura, H. Muto and A. Matsuda, Ag nanoparticle-filled TiO_2 nanotube arrays prepared by anodization and electrophoretic deposition for dye-sensitized solar cells, *Nanotechnology* **28** (2017) 135207-135214.

16. N. Nyein, W. K. Tan, G. Kawaura, A. Matsuda and Z. Lockman, Anodic Ag/TiO_2 nanotube array formation in NaOH/fluoride/ethylene glycol electrolyte as a photoanode for dye-sensitized solar cells, *Nanotechnology* **27** (2016) 355605-355616.

17. G. Kawamura, H. Ohmi, W. K. Tan, Z. Lockman, H. Muto and A. Matsuda, Ag nanoparticle-deposited TiO_2 nanotube arrays for electrodes of dye-sensitized solar cells, *Nanoscale Res. Lett.* **10** (2015) 219.

18. Q. Xu, *et al.*, Broadband light absorption enhancement in dye-sensitized solar cells with Au-Ag alloy popcorn nanoparticles, *Sci. Rep.* **3** (2013) 2112.

19. L. Guo, J. A. Jackman, H-H. Yang, P. Chen, N-J. Cho and D-H. Kim, Strategies for enhancing the sensitivity of plasmonic nanosensors, *Nano Today* **10**, 213-239 (2015).

20. Wen, C., Ishikawa, K., Kishima, M. & Yamada, K. Effects of silver particles on the photovoltaic properties of dye-sensitized TiO_2 thin films. *Sol. Energy Mater. Sol. Cells*, **61** (2000) 339-351.

21. S. P. Lim, A. Pandikumar, H. N. Lim, R. Ramaraj and N. M. Huang, Boosting Photovoltaic Performance of Dye-Sensitized Solar Cells Using Silver Nanoparticle-Decorated N,S-Co-Doped-TiO_2 Photoanode, *Sci. Rep.*, **5** (2015) 11922.

22. A. Wood, M. Giersig and P. Mulvaney, Fermi level equilibration in quantum dot−metal nanojunctions, *J. Phys. Chem. B* **105** (2001) 8810–8815.

23. M. K. Nowotny, L. R. Sheppard, T. Bak and J. Nowotny, Defect chemistry of titanium dioxide, Application of defect engineering in processing of TiO_2-based photocatalysts, *J. Phys. Chem. C* **112** (2008) 5275–5300.

24. F. J. Knorr, C. Mercado, and J. L. McHale, Trap state distributions and carrier transport in pure and mixed phase TiO_2: influence of contacting solvent and interphasial electron transfer, *J. Phys. Chem. C*, **112** (2008) 12786-12794.

25. C. Mercado, Z. Seeley, A. Bandyopadhyay, S. Bose, and J. L. McHale, Photolumiscence of dense nanocrystalline titanium dioxide thin films: effect of doping and thickness and relation to gas sensing, *ACS Appl. Mater. Interfaces* **3**, (2011) 2281-2288.

26. S. Ramakrishna, M. Pelton, S. K. Gray and T. Seideman, Plasmon-enhanced electron injection in dye-sensitized solar cells, *J. Phys. Chem. C*, **119** (2015) 22640–22645.

27. Z. Ning, Q. Zhang, W. Wu, H. Pei, B. Liu and H. Tian, Starburst triarylamine based dyes for efficient dye-sensitized solar cells, *J. Org. Chem.*, 2008 **73** (2008) 3791–3797.

28. M. Mojiri-Foroushani, H. Dehghani and N. Salehi-Vanani, Enhancement of dye-sensitized solar cells performances by improving electron density in conduction band of nanostructure TiO_2 electrode with using a metalloporphyrin as additional dye, *Electrochim. Acta*, **92** (2013) 315-322.

29. S. A. Haque, Y. Tachibana, D. R. Klug and J. R. Durrant, Charge recombination kinetics in dye-sensitized nanocrystalline titanium dioxide films under externally applied bias, *J. Phys. Chem. B*, **102** (1998) 1745-1749.

30. S. A. Haque, *et al.*, Charge separation versus recombination in dye-sensitized nanocrystalline solar cells: the minimization of kinetic redundancy, *J. Am. Chem. Soc.*, **127** (2005) 3456-3462.

31. S. A. Standridge, G. C. Schatz and J. T. Hupp, Toward plasmonic solar cells: protection of silver nanoparticles via atomic layer deposition of TiO_2, *Langmuir*, **25** (2009) 2596-2600.

32. S. Wooh, *et al.*, Plasmon-enhanced photocurrent in quasi-solid-state dye-sensitized solar cells by the inclusion of gold / silica core-shell nanoparticles in a TiO_2 photoanode, *J. Mater. Chem. A*, **1** (2013) 12627-12634.

33. H. Jung *et al.*, Enhanced photovoltaic properties and long-term stability in plasmonic dye-sensitized solar cells via noncorrosive redox mediator, *ACS Appl. Mater. Interfaces*, **6** (2014) 19191-19200.

34. T. Hoshikawa, R. Kikuchi, K. Sasaki and K. Eguchi, Impedance analysis of dye-sensitized solar cells, *Electrochem.*, **70** (2002) 675-680.

35. F. Fabregat-Santiago, J. Bisquert, G. Garcia-Belmonte, G. Boschloo and A. Hagfeldt, Influence of electrolyte in transport and recombination in dye-sensitized solar cells studied by impedance spectroscopy, *Sol. Energy Mater. Sol. Cells*, **87** (2005) 117-131.

36. R. Kern, R. Sastranwan, J. Ferber, R. Stangl and J. Luther, J. Modeling and interpretation of electrical impedance spectra of dye solar cells operated under open-circuit conditions, *Electrochim. Acta*, **47** (2002) 4213-4225.

37. M. Adachi, M. Sakaamoto, J. Jiu, Y. Ogata and S. Isoda, Determination of parameters of electron transport in dye-sensitized solar cells using electrochemical impedance spectroscopy, *J. Phys. Chem. B*, **110** (2006) 13872-13880.

38. J. Nissfolk, K. Fredin, A. Hagfeldt and G. Boschloo, Recombination and transport processes in dye-sensitized solar cells investigated under working conditions, *J. Phys. Chem. B*, **110** (2006) 17715-17718.

Chapter 4

Effects of multi-sized and -shaped Ag@TiO_2 nanoparticles on the performance of plasmonic dye-sensitized solar cells

4.1 Introduction

The dye-sensitized solar cell (DSSC) has come to be accepted as one of the viable alternatives to conventional solid-state p-n junction photovoltaics [1-3] since an unprecedented high power conversion efficiency (PCE) of 7.1 % was designed by B. O'Regan and M. Gratzel [4], in 1991, by the use of a nanoporous-structured TiO_2 working electrode (WE). It has the core advantages of facile and low-cost fabrication, environmentally friendly and good performance under variable light conditions [1-6]. Nevertheless, they have competitively low PCEs, with a certified record PCE of 11.9 %, compared to the more common conventional Si based solar cells in the range of 20-28 % [7]. Thus, the need to improve the PCE of DSSCs.

A brief description of the basic structure and working principle of the DSSC is as follows: a) the WE/photoanode – made up of a porous network of a wide bandgap semiconductor material (SCM; eg TiO_2), sensitized by a layer of dye (eg N719) and supported on a transparent conducting oxide (TCO; eg Fluorine-doped thin oxide (FTO)). The dye absorbs sunlight, generates electrons and inject them into the conduction band (CB) of the SCM which transports them to the TCO, to an external circuit to do work and onward to the counter electrode (CE). b) the CE – consists of a catalytic material (eg Pt) coated on a TCO. It receives the electrons and uses them in the catalytic reduction of the hole conducting material (HCM)/electrolyte (eg I^-/I_3^- redox couple); and c) the HCM – this is sandwiched between the WE and the CE (separated by a thin plastic spacer), and used to reduce the

excited dye to restore and re-start the cycle again. During the percolation of the photogenerated electrons through the SCM, these electrons are likely to recombine with the HCM, and they usually do, referred to as recombination. Thus, the light-to-electric conversion process of the DSSC consists of complicated optical, electrical and chemical processes, which must be kept in a delicate balance. For an efficient cell, efficient light harvesting, rapid electron transport and minimum recombination are critical.

The WE has been identified as the most critical component in the pursuit of improving the PCE of DSSCs, especially in regards to efficient light harvesting [6, 8]. In this regard five WE designs can be identified: a) plasmonic photoanodes; b) mesoporous photoanodes with large surface area (SA); c) hierarchically nanostructured photoanodes; d) dual-functioning scattering layer on top of nanocrystalline electrode; and e) photonic crystal photoanodes [8]. In this work our focus is on plasmonic photoanodes because they have the critical advantages of facile preparation; use of less material; and the high potential of extremely enhancing light absorbance via the localized surface plasmon resonance (LSPR) effect [6, 9, 10].

The LSPR effect arises from subwavelength metallic materials, such that mobile CB electrons are easily polarized about the nanometal and the coulombic restoring force effect, from the nucleus, in an effort to reverse the polarization causes the oscillation of this neutral cloud of electrons and positive charges (plasma) about the nanometal. When light with similar frequency as the oscillating plasma interacts with it, it causes the oscillating plasma to resonate, causing the phenomenon LSPR about the nanostructure. This generates very intense electric field and can modify the density of states (DOS) of vicinal materials. The DOS can be described as ‘channels’ for storing and/or routing electromagnetic energy [10], thus enhancing the optical interactions of the materials. Plasmonic enhancement in plasmonic solar cells can be described by four mechanisms, via two major routes: a) radiative – where the LSPR decays, due to its finite lifetime, and releases its energy in the form of photons.

This decay process can either generate DOS in vicinal materials, referred to as “near-field” effect; or cause light scattering into its vicinal environment, referred to as “far-field” effect; b) non-radiative decay, where the LSPR relaxes to generate electron-hole pairs. This process can occur through Landau damping to generate hot-electrons which can have sufficient energy to traverse a Schottky barrier to the CB of SCMs, referred to as “hot-electron transfer”; or electron-hole pairs transfer below and near the SCM band edge via dipole-dipole coupling, referred to as “plasmon-energy transfer” [9]. The LSPR effect is affected by the size, shape, composition and environment of the nanometal.

With this high potential to increase the light absorption of the WE, and ultimately the PCE, of DSSCs, there has been intensive research into plasmonic DSSCs with various approaches, with the primary focus on enhancing light absorbance of the cell/WE; and with significant successes [9, 11-25]. Nevertheless, the highest plasmonic DSSC PCE is still < 11% [9]. This is because, apart from enhancing the light absorbance of the cell, plasmonic nanostructures have secondary effects that affect the ultimate performance of the cell. These secondary effects are not yet well understood. Hence, the focus of our research is to improve the understanding of these secondary effects. Most of the referenced papers above on plasmonic DSSCs have unequivocally observed the enhancement of light absorption of their cells/WEs. Some have also observed some of these secondary effects such as poor performance of cells at high plasmonic loadings, which is increasingly being explained to be due poor charge injection efficiency, resulting from the upward shift of the CB edge of the SCM by the plasmonic nanostructures.

Villanueva-Cab *et al.* [12] investigated the assumption that bare plasmonic metal nanoparticles (NPs) work as recombination centres in plasmonic DSSCs, using Au NPs. Their results showed that the plasmonic WEs showed lower absorbances in the ultraviolet-visible (UV-Vis) region than the pristine reference sample, although higher performance in

the near infra-red (NIR) region. They also showed lower values of short-circuit current density (J_{sc}), open-circuit voltage (V_{oc}), charge transfer resistance (R_{ct}) and electron life time (τ_n), than the reference sample. Charge collection efficiency (η_{cc}) was said to be constant. They observed poor charge injection efficiency (η_{inj}) from upward CB edge shift. They concluded that Au NPs acting as recombination centres cannot fully explain photovoltaic behaviours of DSSCs. Choi *et al.* [18] investigated the charging effects of plasmonic NPs in DSSC using SiO_2 (insulator)- and TiO_2 (SCM)-capped Au NPs. They observed enhanced light absorbance, with consequent increase in J_{sc}, in both samples; but increase in V_{oc} was observed only in the TiO_2-capped Au NPs samples. The increase in V_{oc} was ascribed to the capture of electrons from TiO_2 and TiO_2-dye composite by the Au core, and undergoing a fermi level equilibration (charging effect). There was no observed significant plasmonic effect on fill factor (*FF*), but an effect of decreasing J_{sc} at plasmonic NPs loadings > 0.7 %, suggested to be due to filtering effects of the Au core. In the work of Qi *et al.* [19], using uniform shell and size distribution of Ag@TiO_2 core-shell (C-S) NPs, they observed enhanced light absorbance and PCE. The major enhancement effect in their incident photon-to-current efficiency (IPCE) results was observed in the wavelength region of 400-500 nm, where the LSPR peak of their NPs is located. They did not observe significant effects on *FF* and V_{oc}, but J_{sc} and PCE decreased in > 0.6 % plasmonic loading, which they suggested was due to electron trapping and part-conversion of incident radiation to heat. In our laboratory, using bare Ag NPs-filled TiO_2 nanotube plasmonic DSSCs, fabricated with various growth techniques and NPs-loading approaches [26-28], we observed enhanced light absorption, J_{sc} and PCE. We also observed increased V_{oc} and *FF*, but in one study with electrochemical impedance spectroscopy (EIS) evaluation, we observed a reduction in R_{ct} and τ_n [26].

Thus, there are significant variations in reported results on the effects of plasmonic NPs in DSSCs, barring the differences in the DSSC types employed; suggesting the need for more

systematic studies on the effects of plasmonic NPs on the performance of DSSCs. We think this is because of the use of limited characterizations with fewer and narrow-range plasmonic loading concentrations.

In this work of chapter 4 we have combined extended characterizations (optical absorption; photoluminescence spectroscopy (PL); I-V; EIS and IPCE) and wider-range plasmonic NPs loading concentrations (0.1, 0.25, 0.5, 1 and 5 %), with a systematic approach to obtain a more holistic and synergistic effect of plasmonic NPs in DSSCs. We used Ag@TiO_2 C-S PNPs to avoid the possible corrosion of the Ag NPs by the corrosive I-/I_3^- electrolyte [22]. Since the LSPR effect is affected by the size and shape of the NPs, we selected wide-range particle size and shape distributions for a panchromatic enhancement effect. Although a panchromatic plasmonic enhancement effect was observed, the IPCE results showed a complex trend effect.

4.2 Experimental

4.2.1 One-pot synthesis of Ag@TiO_2 C-S NPs

The Ag@TiO_2 PNPs were prepared using a procedure in literature [29] with slight modification. Briefly, 112.5 ml of N, N-dimethylformamide (super dehydrated, Wako; ≥ 99.5%) (DMF) was mixed with 1.62 ml of 0.26 mol L^{-1} $AgNO_3$ (Wako; ≥ 99.8% min.) and stirred for 30 min at 350 rpm into a pale yellow solution of Ag NPs. The DMF served both as a reducing agent for the Ag^+ ions and a dispersing agent for the Ag NPs. A second solution of $Ti(OC_4H_9)_4$ (Wako; ≥ 95.0%) (TOB) was prepared by mixing 0.881 g of it with 445 ml ethanol (super dehydrated, Wako; ≥ 99.5%) and stirred for 20 min at 700 rpm. It was chelated (to control hydrolysis) with 0.259 g acetylacetone (Wako; ≥ 99.0%) in 5 ml ethanol and then stirred for 30 min at 700 rpm. This solution was added, gradually, to the Ag NPs solution, whiles stirring. The mixture was then refluxed at ~ 104 ˚C for 1.5 h, with stirring at 350 rpm.

A greenish-black colloidal solution was obtained. This was cooled to room temperature and centrifuged at 8000 rpm for 1 hr. The residue was re-dispersed and washed in ethanol by sonication, and then centrifuged again. This was repeated a second time with a final re-dispersion in ethanol, evaporated at 80 °C and heat treated at 250 °C (based on TG-DTA analysis, not shown here) to obtain the pure Ag@TiO_2 C-S NPs.

4.2.2 Pastes and photoanodes preparation

The pastes for the photoanodes fabrication were prepared using a planetary ball miller (Fritsch pulverisette 7) with alumina mortar and balls. For the pristine paste (0 %), 1.74 ml of ethylene glycol (dehydrated, Wako; ≥ 99.5%) was added to 1.0 g of TiO_2 P25 (Sigma-Aldrich; 21 nm; ≥ 99.5%) and then milled at 500 rpm for 1 hr. After that 1.69 g Citric acid (Chameleon reagent; anhydrous, ≥ 99.5%) was added and milled again for another 1 h. For the Ag@TiO_2-doped pastes, the same preparation procedure was used with the appropriate mass of Ag@TiO_2 replacing the appropriate amount of TiO_2 P25 to obtain the doped pastes (0.1, 0.25, 0.5, 1 and 5 %).

The photoanodes were prepared via a doctor blade coating on fluorine-doped tin oxide (FTO)-on-glass substrates (85% T, 9 Ω/□; 3 × 2 cm). The FTO substrates were first cleaned by RCA treatment and coated with a TiO_2 buffer layer by treatment in 0.04 mol L^{-1} $TiCl_4$ (Wako; ≥ 99.0%) solution at 70 °C for 30 min (with 2 cm^2 active area masking), washed with water and heat-treated at 450 °C for 1 h. The FTO substrates were coated with the pastes using 60 μm scotch tape masks with a circular active area (diameter; 10 mm (0.785 cm^2) each. For uniformity and reproducibility, the doctor blade was kept at a constant distance over the substrate and an 80 g weight of steel blocked applied on it to make contact with the substrate. The blade was drawn at a rate of 2.5 mm s^{-1} to spread the paste. The samples were dried sequentially on a hot plate at ambient temperature: at RT, 60 °C and 120 °C, for 5 min each, and a final heat treatment (HT) at 500 °C for 1 h. The calcined samples were washed with

ethanol and dried with a hot blower. For dye sensitization, the dried samples were immersed in a 0.3 mmol L^{-1} of N719 dye (ALDRICH; 65 mol% dioxole), in a 1:1 solvent system of acetonitrile (Wako; 99.5 %)-tert-butyl alcohol (Wako; 99.0 %), for 24 h. The dye-sensitized photoanodes were rinsed with acetonitrile to remove excess dye, and dried using a hot blower.

4.2.3 DSSCs Assembling

Sandwich-type cells were prepared using a 50 μm plastic spacer (DuPont, Himilan) with an open area of 1.13 cm^2 (12 mm diameter). The dye-sensitized photoanodes were sealed to the platinized CEs via heating on a hot plate at 105 °C, with a 1 kg weight load, for about 5 min. The CEs were prepared using RCA-cleaned FTO substrates with drilled holes, 11.5 mm apart, and Pt coating using a sputter coater (Hitachi E-1030 ion sputter) at 15 mA for 600 s. An acetonitrile solvent based electrolyte, composed of 0.05 mol L^{-1} iodine (Aldrich; ≥ 99%), 0.1 mol L^{-1} lithium iodide (Strem Chemicals; anhydrous, ≥ 98 %), 0.6 mol L^{-1} 1, 2-dimethyl-3-propylimidazolium iodide (TCI; > 98 %), and 0.5 mol L^{-1} 4-tert-butylpyridine (Aldrich; 96 %), was injected into the cell and sealed with a piece of the spacer and scotch tape. Dye-sensitized solar cells with Ag@TiO_2 PNPs doping concentrations of 0.1, 0.25, 0.5, 1 and 5 %, in addition to a reference un-doped DSSC, 0 %, were obtained.

4.2.4 Characterization

The optical absorption characteristics of the plasmonic NPs and photoanodes were evaluated using a JASCO V-670 UV-Vis-NIR spectrophotometer. The particle size, size distribution and core-shell structure of the Ag@TiO_2 C-S NPs were observed using a JEOL JEM-2100 F TEM. A Rigaku Ultima IV R285S XRD was used to study the composition and crystallinity of the Ag@TiO_2 C-S NPs. The PL spectroscopy of the photoanodes was evaluated using a He-Cd laser (325 nm) as the excitation source. The luminescence was evaluated by a multi-

channel CCD spectrometer. The I-V characteristics of the cells were evaluated using ADCMT 6244 DC Voltage/Current Source/Monitor and an HAL-320 W solar simulator (Asahi spectra) with a 300 W xenon lamp and an air-mass 1.5 global filter. The solar simulator was calibrated to an intensity of 100 mW cm^{-2} (One sun), using a One sun checker (Asahi CS-40). The IPCE characterization was done via a DC method, using Bunkoukeiki SM-250KB spectrometer with a Keithley 2401 source meter and an irradiation flux of 2.0 x 10^{15} photons, with a masking with active area of 1 cm^2. A Hitachi S-4800 FE-SEM was used to study the morphology and thickness of photoanode coatings. The electron transport dynamics of the photogenerated electrons was evaluated via an EIS equipment (Solartron SI 1287 Electrochemical Interface and Solartron1255B Frequency Response Analyzer) under bias of the open circuit voltage, V_{oc}, within a frequency range of 0.1 Hz to 1 MHz, and an ac amplitude of 40 mV; and under a light irradiation of 100 mW/cm^2 (1 SUN).

4.3 Results and discussion

4.3.1 Formation, morphology and composition of Ag@TiO_2 C-S NPs

We monitored the formation of the Ag and Ag@TiO_2 C-S NPs in the preparation process using optical absorbance spectroscopy. The results are shown in Fig. 4.1 a). The LSPR peak of the Ag NPs was seen at 410 nm. The peak shifted to 420 nm with a panchromatic enhanced absorbance into the NIR region in the C-S NPs spectrum, which is the characteristic red-shift due to higher dielectric TiO_2 shell covering. Figure 4.1 b) shows the TEM image of well-dispersed C-S NPs after extraction and HT at 250 °C. The inset image is a magnified portion to show the complex varied size (7-40 nm) and shape (hexagonal, triangular, circular, cylindrical, etc.) distributions of the PNPs which we believe caused the enhanced absorbance into the NIR region by promoting different plasmon modes. Figure 4.1 c) is a high resolution (HR)-TEM image of a cluster of the C-S NPs to clearly show the thin (~ 2 nm) TiO_2 shell, marked with red asterisks. The thinness of the shell is very critical for

transmission of the LSPR field enhancement effects as they have a penetration depth of ~ 10 nm [21], although transmission mechanisms via far-field scattering and secondary effects of surface plasmon polaritons can reach depths of 100 nm and 1 μm, respectively [21]. A thin shell is also necessary for possible hot-tunneling transfer of hot electrons generated from the LSPR effect.

We also evaluated the crystalline structure of the plasmonic C-S NPs via XRD characterization, Fig. 4.1 d). The as-prepared and dried sample at 80 °C showed crystalline Ag core NPs with diffraction patterns of cubic Ag of (111), (200), (220) and (311) planes (JCPDS No. 04-0783). This is corroborated by the crystalline fringes of the Ag core in the HR-TEM image in Fig. 4.1 c). There were no observed TiO_2 peaks, indicating an amorphous shell. At 250 °C HT to obtain the pure plasmonic NPs, the shell was still amorphous, however, at 500 °C, the HT temperature for the photoanode fabrication, the shell crystallized with a broad diffraction peak from the (101) plane of anatase (JCPDS No. 21-1272). Crystallization of the TiO_2 shell is necessary for conduction of electrons. The broadness of the peak is attributed to the small crystallite size (< 2 nm) of the TiO_2 shell.

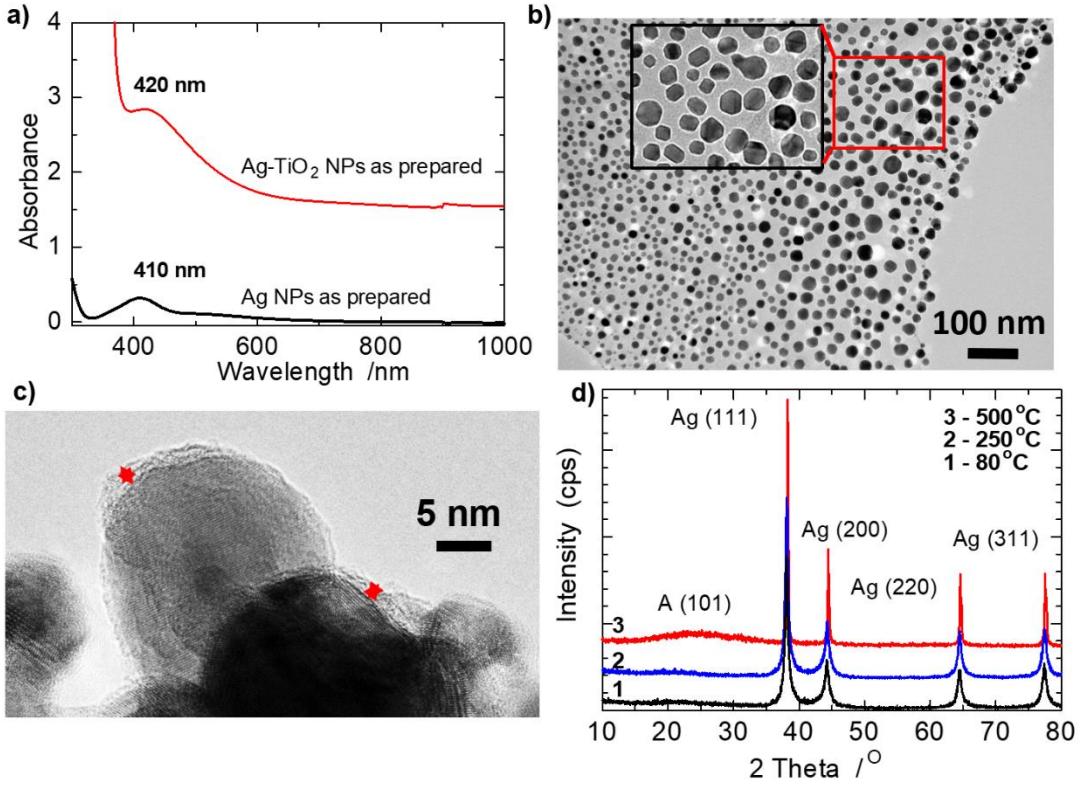

Fig. 4.1 a) Absorbance spectra of Ag and Ag@TiO_2 NPs. **b)** TEM image of the Ag@TiO2 NPs after HT at 250 °C; inset: expanded portion to show complex composite of Ag@TiO_2 NPs of various shapes and sizes. **c)** HR-TEM image of Ag@TiO_2 NPs after HT at 250 °C. **d)** XRD patterns of the Ag@TiO_2 NPs at various HT temperatures.

4.3.2 Corrosion stability of the plasmonic Ag@TiO_2 NPs

One of the functions of the TiO_2 shell is to protect the plasmonic Ag core from the corrosive effects of the I^-/I_3^- redox couple electrolyte. Thus we performed a corrosion stability test using 1 % $HNO_{3(aq)}$ and optical absorbance spectroscopy. From the curves in Fig. 4.2 a), the LSPR peak of Ag at 410 nm disappears in the acid-treated sample but is prominent in the non-treated sample. This indicates the dissolution of the Ag NPs, and is corroborated visually

in the inset image with the pale yellow Ag NPs suspension in the non-treated sample (left) disappearing to a colourless solution in the acid-treated sample (right). In an analogous test using 250 °C heat treated Ag@TiO_2 C-S NPs, Fig. 4.2 b), a broadband panchromatic plasmonic absorbance effect is observed in both non- and acid-treated samples, except for a slightly lower absorbance intensity in the acid-treated sample. This lower absorbance is attributed to the dilution effect of the added acid. The optical absorbance test result is corroborated by a visual examination test, inset image of Fig. 4.2 b), in which both the non-treated (left) and acid-treated sample (right) possess the same black colour of the C-S NPs suspensions. Thus, the thin TiO_2 shell protects the core plasmonic Ag NPs against corrosion, and by extension against the corrosive electrolyte. This also corroborates the C-S structure of the plasmonic NPs.

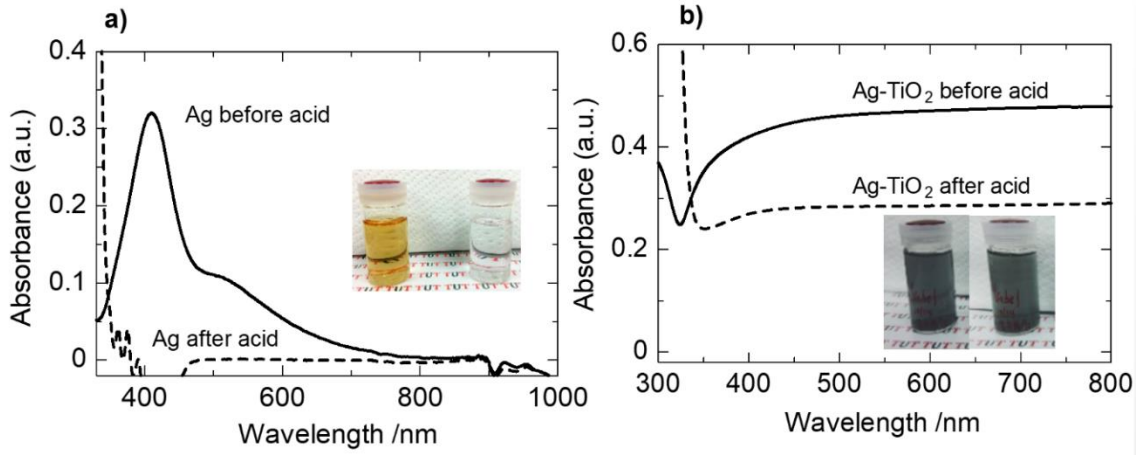

Fig. 4.2 Absorbance spectra of corrosion stability tests: **a)** Ag nanoparticles. **b)** Ag@TiO_2 nanoparticles.

4.3.3 Effects of PNPs via optical characterization

Recombination of photogenerated electrons in the TiO_2 SCM of DSSCs is one of the major contributors to the low performance of DSSCs. Metallic NPs have been reported to capture electrons onto themselves, so called electron-sink effect [14, 18, 24, 30], which causes efficient electron-hole separation. This has a consequent increase in charge transfer resistance against recombination and increase in electron lifetime; but also contributes to the upward shift of the fermi level of the TiO_2 SCM. We investigated the electron-sink effect via PL spectroscopy, which measures the intensity of photon emissions resulting from electron-hole recombination. The results are shown in Fig. 4.3 a). As is seen, the pristine sample records the highest PL intensity, indicating the highest electron-hole recombination. This is followed by a trend of decreasing PL intensity with increasing amount of plasmonic NPs, indicating increasing electron capture with increasing plasmonic NPs. Anatase as an indirect band gap SCM ordinarily should not exhibit PL, however, with intrinsic oxygen vacancies (giving it its *n*-type semiconductor property) [31], generating different kinds of electron-hole traps, randomly distributed within the forbidden band gap, various transitions are created, resulting in the typical broadband Vis PL spectrum of TiO_2 [32], as observed in Fig. 4.3 a). The generally low PL intensities obtained are attributed to the porous and thin (5.5 μm) nature of our coatings, as similarly reported by Mercado *et al.* [33].

We evaluated the light absorbance enhancement effect of the plasmonic NPs via optical absorbance spectroscopy, using dye-sensitized photoanodes, Fig. 4.3 b).

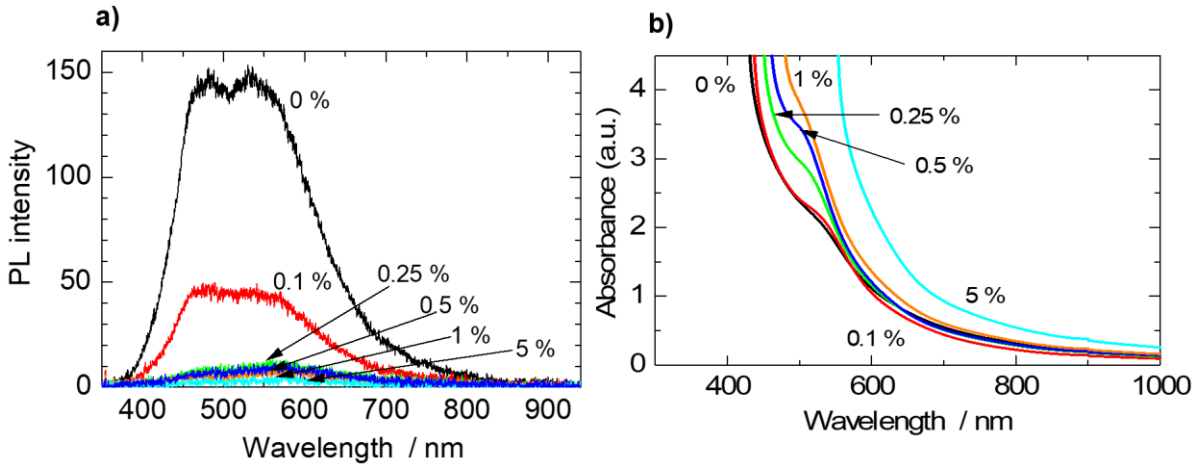

Fig. 4.3 a) PL spectra of photoanodes with various amounts of Ag@TiO_2 loadings. **b)** Absorbance spectra of N719 dye-sensitized photoanodes with various amounts of Ag@TiO_2 loadings.

As seen in the absorbance spectra of the photoanodes, photoanode absorbance increases with increasing plasmonic NPs loading, and thus these enhancements in light absorption are attributed to the LSPR effect. Sample 0.1 % seems to have, averagely, the same absorbance as the pristine sample; this is due to the balancing of the complex effects of low concentration and distribution of PNPs in a thin coating (5.5 µm) with a reduced SA (Table 4.1). And by distribution, we refer to the complexity of total number of plasmonic NPs (PNPs) in the coating; PNPs per unit area; distance between PNPs; amount of different shapes and sizes PNPs and their interactive effects.

To obtain a deeper and clearer enhancement effect of the PNPs on the dye absorbance, we investigated various dye-PNPs combinations in solution. The results are shown in Fig. 4.4. All solutions were prepared in 5 mL ethanol with concentrations of "dye only" and "Ag-TiO_2

only" PNPs as 3 mmol L^{-1} and 4 mg in 5 mL ethanol, respectively. It can be seen, Fig. 4 a), that addition of 3 mg PNPs to the dye solution increased the absorbance of the resultant solution (green spectrum) over both dye only (black spectrum) and PNPs only (red spectrum), with a further increase when the PNPs amount was increased to 4 mg (orange spectrum). These results corroborate the light absorbance enhancement effect of the PNPs on the N719 dye in the photoanode. To investigate an interactive synergistic effect between the dye and PNPs, we compared the spectra of the dye-PNPs solutions; dye only spectrum; and the spectrum of an arithmetic addition of dye only absorbance and 3 mg PNPs only absorbance (blue spectrum) to each other. As observed in Fig. 4.4 a), the peaks and troughs of the dye-PNPs solutions spectra match each other and are blue-shifted, compared to the dye only spectrum; whiles the spectrum of the arithmetical sum matches that of the dye only spectrum. These observations indicate an interactive coupling effect between the dye molecules and the LSPR of the PNPs.

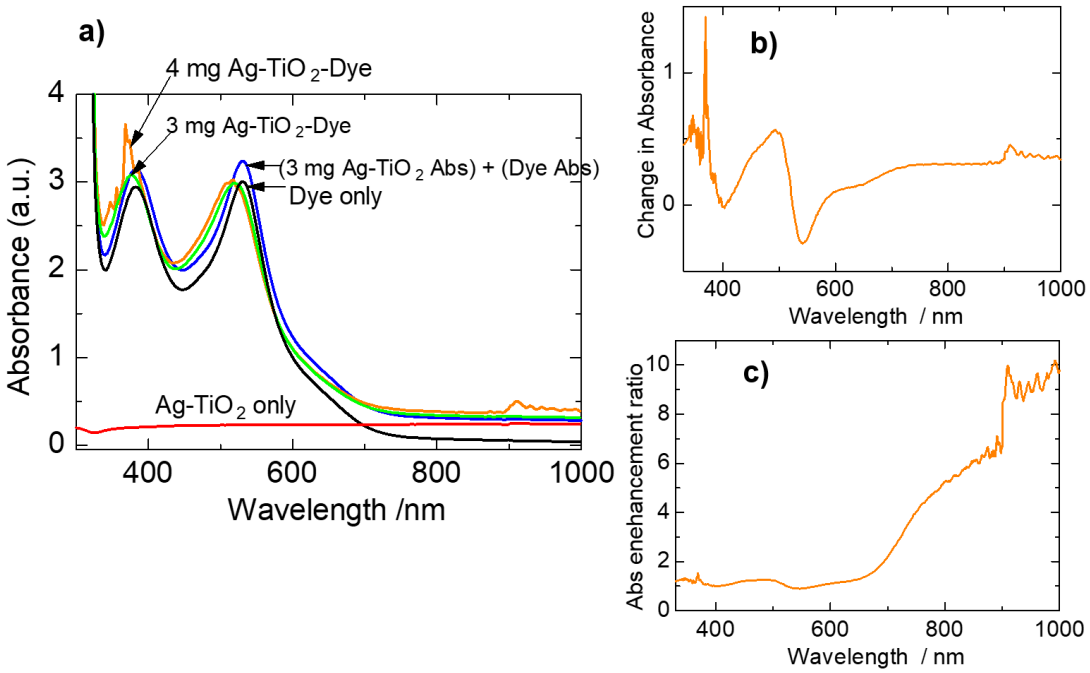

Fig. 4.4 a) Absorbance spectra of PNPs, N719 dye and their mixtures (dye-PNPs) in solution. **b)** [dye-PNPs absorbance] – [N719 dye absorbance]. **c)** [dye-PNPs absorbance] / [N719 dye absorbance].

To obtain the quantitative enhancement effect of the PNPs on the dye, we deducted the absorbance of the dye from the absorbance of dye-4 mg PNPs mixture to obtain the spectrum in Fig. 4.4 b). It revealed the highest absorbance enhancement (~ 0.5) was in the region of 400-500 nm, which is the maximum LSPR peak region of the PNPs. It also revealed that it enhanced the dye in its weak absorbing regions, especially in the energy-rich IR region. On the other hand, it also reveals that these PNPs, under these conditions, have no significant enhancement effect at the most efficient absorbing regions of the N719, around 390 and 530 nm. To investigate the relative enhancement effect of the PNPs, we divided the absorbance of

the dye-4 mg PNPs by the absorbance of the dye only to obtain the spectrum of Fig. 4.4 c). It revealed a panchromatic enhancement effect, with the major effect in the NIR region by about x9. Thus, the PNPs unequivocally enhanced the N719 dye absorbance across the UV-Vis-NIR region; hence, with the appropriate tuning very high light absorbance can be obtained.

4.3.4 Effect of PNPs on DSSC performance via I-V characterization

The ultimate aim of the use of the plasmonic effect of PNPs in DSSCs is to enhance the PCE of DSSCs. Thus, we assembled the plasmonic and pristine photoanodes into DSSCs to investigate their effects on the various key performance parameters of DSSCs that lead to the final PCE. The results are summarized, quantitatively, in Table 4.1 and graphically in Fig. 4.5. We first evaluated the I-V characterization results, columns 3-6 of Table 4.1. We also measured the SA of powders obtained from calcination at 500 °C of the plasmonic and pristine pastes to study the effect of the PNPs on the SA of the photoanode. The results are shown in column 2 of Table 4.1 and Fig. 4.5 a), which show a gradual and steady decreasing effect on SA with increasing PNPs loading. This suggests less surface for dye attachment; hence, less light absorbance in PNPs-loaded photoanodes.

However, upon evaluating the dye loading amounts of the photoanodes the following values were obtained: 2.10; 2.11; 2.12; 2.12; 2.12; and 2.10×10^{-6} moles cm^{-2}. These results suggest that the effect of reduction in surface area due to loaded PNPs did not have significant effect on the amount of dye adsorbed by the photoanodes. The apparent slightly higher adsorbed dye in the plasmonic loaded samples over the pristine sample may be due to modification of surface states of TiO_2 (which affect the anchorage of dye molecules onto the surface of TiO_2) by the PNPs; or slight leaching of PNPs into the dye solution to give false absorbance readings. The dye loading was done using optical absorbance spectroscopy by deducting the absorbance of the 10 mL dye solution in which each photoanode was soaked from the

absorbance of the dye before the soaking. This evaluation was repeated using the more common dye desorption method, which gave very similar results. However, the optical absorbance spectroscopy results of the photoanodes in Fig. 4.3 b) shows otherwise: with increasing light absorbance as PNPs loading amount increased. This is a situation of the LSPR effect on light absorbance outweighing the negative SA effect on light absorbance. We also observe in column 3 that the sample with the highest J_{sc} of 8.67 mA cm^{-2} is a plasmonic cell with 0.1 % PNPs loading. This J_{sc} value is 24.4 % higher than the pristine sample, although it has 1.5 % less SA. The sample with 0.25 % PNPs loading, with an even lower SA (2.0 % less) has also got a higher J_{sc} than the pristine sample by 9.2 %. These results show the light absorbance enhancement effect of the PNPs. The rest of the samples have lower J_{sc}s than the pristine sample and with a generally decreasing trend with increasing amount of PNPs loading. These lower values are attributed to the synergistic effects of reducing SA and poor charge injection efficiency, but mainly due to poor charge injection efficiency, because of the rapid decreasing of J_{sc} compared to the decreasing trend of SA.

In addition the results of the optical absorbance spectroscopy of the photoanodes showed a continuous increasing absorbance with increasing PNPs loading. The poor charge injection is the result of LSPR effect-induced upward shift of the CB edge/fermi level of the TiO_2, evidenced in the increasing V_{oc} with increasing PNPs loading. One definition of the V_{oc} of DSSCs is, the difference between the fermi level of the SCM and the redox potential of the electrolyte. Hence, since it was only the SCM which was being changed with different amounts of PNPs loading, the observed changing V_{oc} is the result of the PNPs effect. The observed apparent deviation from the trend in Fig. 4.5 d) with a lower V_{oc} of the 0.1 % loaded sample than the pristine sample is attributed to PNPs-induced deep traps which lower quasi-fermi level and decrease conductivity [34]. The lowered V_{oc} would enhance efficient injection of photogenerated electrons [35], as observed in the high J_{sc} value of the 0.1 % loaded sample,

because there is a threshold energy difference value between the LUMO of the N719 and the CB of TiO_2 below which there is inefficient charge injection from the LUMO [15, 35, 36]. An analogous explanation is given to the results of sample 1 %. These results suggest that depending on the distribution (as described under section 4.3.3) the PNPs may induce shallow trap (which means upward shift of fermi level, with possible lower charge injection efficiency, but enhanced conductivity) or deep traps (which means lower fermi level which promotes enhanced charge injection efficiency, but with lower charge carrier conductivity).

This observation is corroborated by the *FF* results in Table 1 and Fig. 4.5 e). The results show a general trend of increasing *FF* with increasing amount of PNPs loading. However, the samples with 0.1 and 1 % PNPs loadings show relatively lower *FF* values, compared to their preceding samples. The *FF* value is mainly lowered by increase in series resistance, which reduced conductivity. Hence, the lower *FF* values for 0.1 and 1 % loadings are attributed to PNPs-induced deep traps.

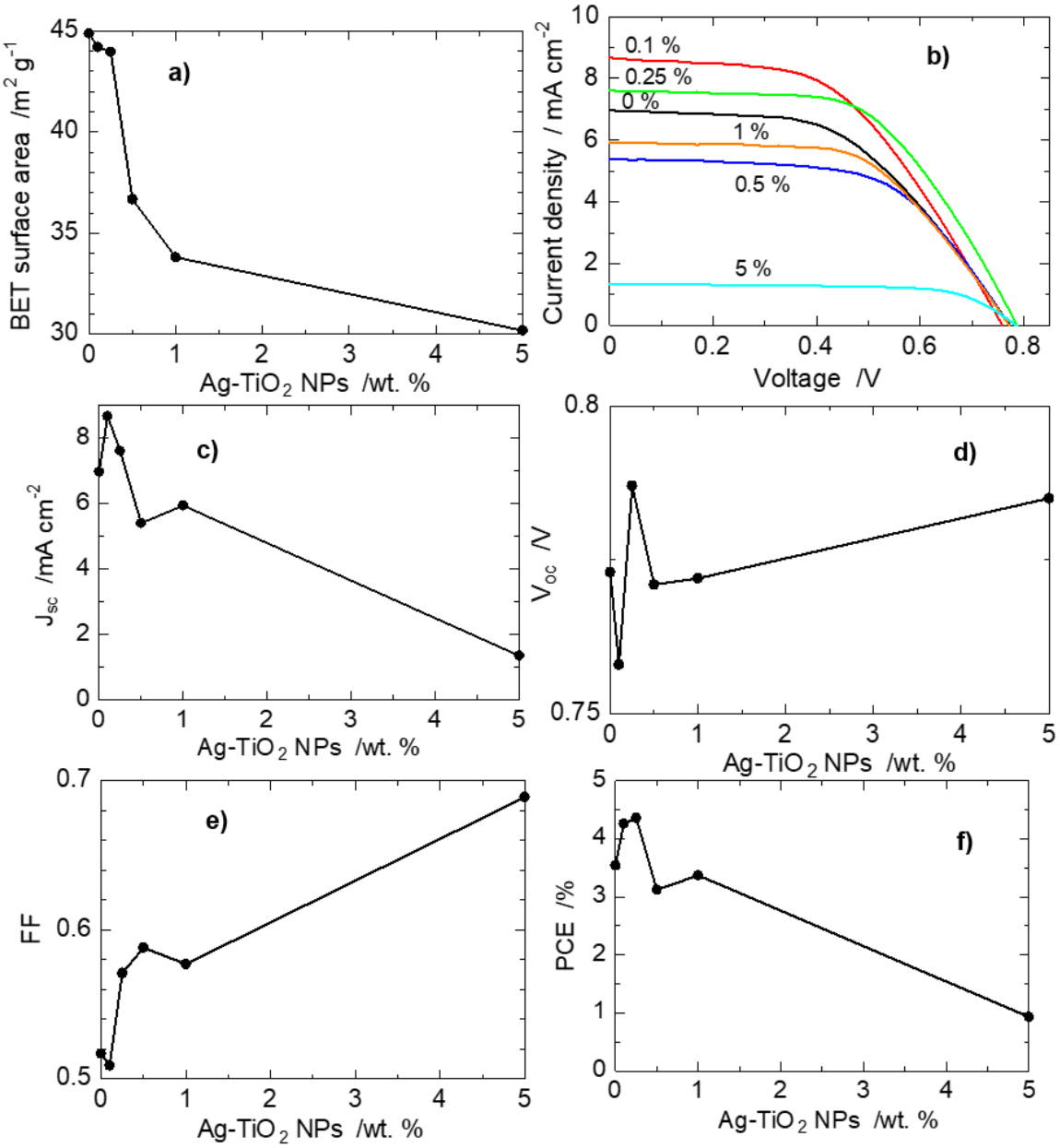

Fig. 4.5 a) Surface area changes of the photoanodes from various Ag@TiO_2 loadings. **b)** I-V curves of DSSCs. Changes in **c)** J_{sc}, **d)** V_{oc}, **e)** *FF* and f) PCE from various Ag@TiO_2 loadings, respectively.

The PCE is given by (J_{sc} * V_{oc} * FF) / P_{in}; where P_{in} is the incident light power per unit area; thus, the effects of the PNPs on the key parameters in the relation, and as explained above, resulted in the PCE values of Table 4.1 and PNPs effect trend of Fig. 4.5 f). However, the interesting point in these results is that although sample 0.1 % generated the highest J_{sc}, it did not produce the highest PCE. The general basic aim of the use of plasmonic nanostructures in photovoltaics is to increase light absorbance to generate abundant charge carriers and to ultimately increase PCE of cells. Sample 0.1 % performed these functions and increased PCE by more than 20 %, nevertheless it was sample 0.25 % which produced the highest PCE of 4.36 %, more than 23 % enhancement. These results reveal that, with a focus on appropriately balancing the positive and negative effects of plasmonic nanostructures loading on the key PCE parameters higher efficiencies can be obtained than focusing only on producing photoanodes with high light absorbance to generate the highest J_{sc}.

4.3.5 EIS characterization

To support the explanations given for the observed results in the I-V characterization, we carried out EIS characterization for key electron kinetics parameters. The results are shown in the last three columns of Table 4.1 and in Fig. 4.6. Figure 4.6 a) is the Nyquist plots of the DSSCs showing the typical three semicircles representing charge transfer kinetics at the counter electrode, photoanode and electrolyte, from left (high frequency region) through the middle (mid-frequency; 1000-3.16 Hz for our DSSC system) to the right (low frequency region) of the graph, respectively. There is no significant difference among the curves in the high and low frequency regions semicircles, indicating that the PNPs do not affect the charge kinetics at the counter electrode and in the electrolyte, as expected. However, significant differences are observed in the middle semicircles of the photoanodes, where the PNPs are located. Especially obvious is the generally increasing diameter with increasing PNPs loading. This diameter represents R_{ct}, which measures the resistance against charge carrier

recombination at the TiO_2-dye/electrolyte interface. This is evidence of the electron-sink effect of the PNPs causing effective electron-hole separation via electron trapping by the Ag core.

The R_{ct} values of samples 0.1 and 1 % are lower than their preceding samples, supporting our explanation of PNPs-induced deep trap states which lowers resistance against recombination because these are avenues for recombination. This was also corroborated in the extracted electron lifetime, τ_n, of the DSSCs, which is the time period before an excited charge carrier recombines, and hence a measure of charge recombination. It was estimated using the relation, $\tau_n = 1 / (2\pi f)$, where f is the frequency at the peak of the semicircle. As can be seen from Table 1 and Fig. 4.6 c) this parameter generally increases with increasing PNPs loading, showing the electron-sink effect of trapping the electrons before they recombine.

Table 4.1: Key DSSC performance parameters from I-V and EIS characterizations of 5.5 µm-thick photoanodes.

Amt. of Ag@TiO_2 /wt. %	BET SA /$m^2\ g^{-1}$	J_{sc} /mA cm^{-2}	V_{oc} /V	*FF*	PCE /%	R_{ct} /Ω	τ_n /ms	η_{cc}
0	44.88	6.97	0.773	0.517	**3.54**	8.4	5.04	0.271
0.1	44.20	8.67	0.758	0.509	**4.26**	7.2	7.96	0.232
0.25	43.96	7.61	0.787	0.571	**4.36**	9.1	10.07	0.294
0.5	36.68	5.40	0.771	0.588	3.12	10.0	12.63	0.323
1	33.81	5.94	0.772	0.577	3.37	8.4	10.07	0.271
5	30.19	1.35	0.785	0.689	0.93	16.5	15.92	0.532

The lower value of sample 1 % compared to the preceding sample (0.5 %) supports the assertion of induced deep traps increasing recombination, as observed in the I-V and R_{ct}

results. A similar result is obtained between sample 0.1 % and the pristine sample. However, sample 0.1 % recorded a higher value (7.96 > 5.04 ms). Nevertheless, we think there was still an increase in recombination but not to the extent that the τ_n of sample 0.1 % would be lower than that of the pristine sample. This is supported by its lower η_{cc} (which is a measure of how efficiently photoinjected electrons are transported to the FTO substrate) than that of the pristine sample; with an analogous result between sample 1 % and 0.5 %. An interesting observation here is that, although sample 0.1 % had the lowest η_{cc} it still recorded the highest J_{sc}, indicating the abundant amount of charge carriers generated and a significant loss to recombination at this optimal PNPs loading concentration. There may also be the contributory effect of increased exponential recombination as a consequence of high charge density generated in the TiO_2 SCM [37]. The η_{cc} values were calculated using the relation, $\eta_{cc} = 1 / [1 + (R_s / R_{ct})]$; where R_s is the series resistance, obtained from the intercept of the Nyquist plots at the high frequency end of the real axis (Z'). Generally, the PNPs increased η_{cc} as observed in the generally increasing values of η_{cc} with increasing PNPs loading. This enhancement effect is attributed to the contributory effects of trapping-detrapping of photogenerated charge carriers from the electron-sink effect and generation of shallow trap states, especially close to the CB of the TiO_2 SCM, which improves charge transport [34]. The increasing η_{cc} at higher PNPs loadings also has the contributory effect from the increased R_{ct} with low charge recombination as a result of low charge density in TiO_2 as ripple effects of PNPs-induced increased V_{oc} and poor charge injection efficiency.

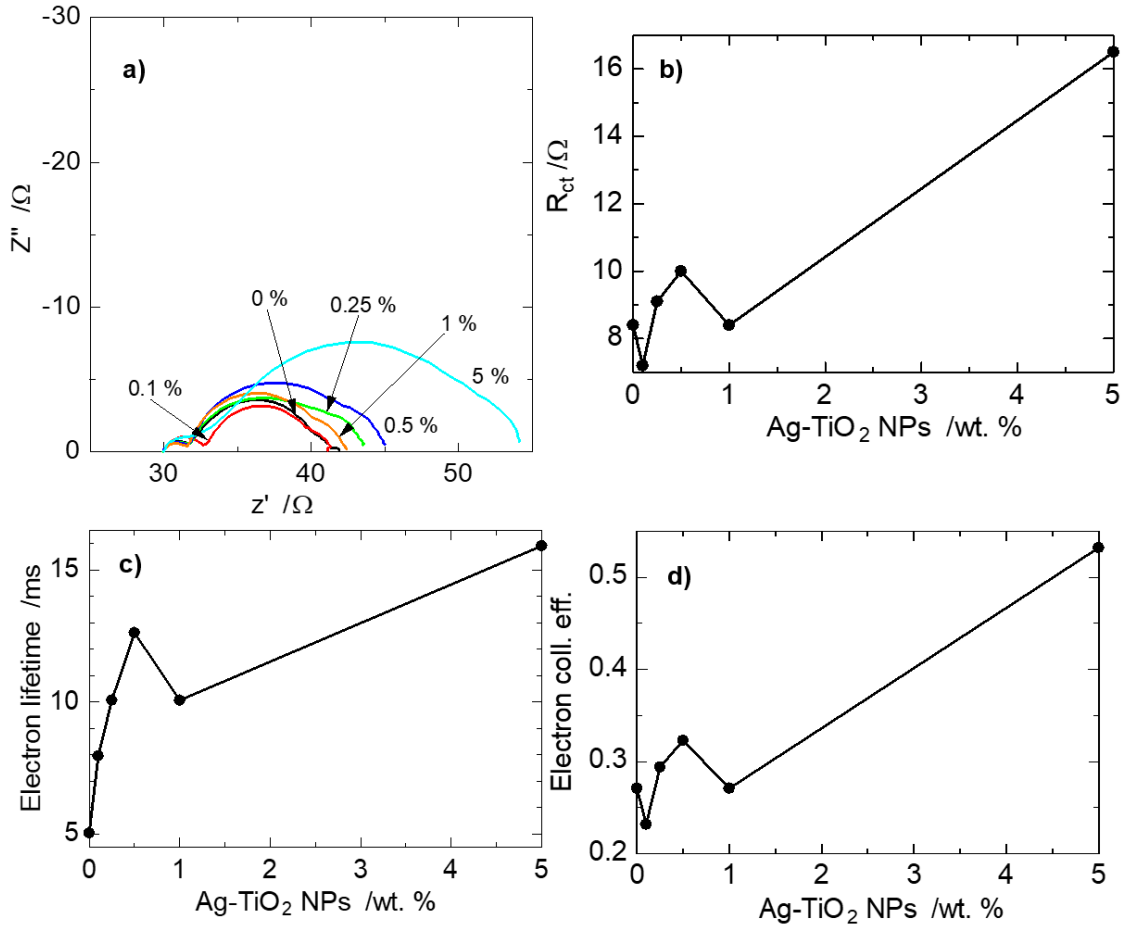

Fig. 4.6 a) Nyquist plots of DSSCs with various amounts of Ag@TiO_2 loadings. Changes in **b)** R_{ct}, c) τ_n and d) η_{cc} with various amounts of Ag@TiO_2 loadings, respectively.

4.3.6 IPCE characterization

Plasmonic effect on the performance of the DSSCs was further investigated with respect to wavelength via IPCE evaluation. The results are shown in Fig. 4.7. Figure 4.7 a) shows the IPCE spectra of the plasmonic DSSCs and that of the pristine sample. We observed the same PNPs-effect trends as in the I-V and EIS characterization results, and hence accord the same explanations. However, the pristine sample has the highest performance in the UV region,

where light absorbance is mainly from the TiO_2 SCM. Thus, this observation is attributed to effective loss of TiO_2 NPs (replaced by the amount of Ag in the Ag@TiO_2 PNPs) in the plasmonic samples. To estimate the quantum of PNPs enhancement effect, we deducted the IPCE of the pristine sample from those of the plasmonic samples to obtain the spectra of Fig. 4.7 b) (as change in IPCE). As is seen in Fig. 4.7 b), the PNPs have a panchromatic enhancement effect with the major enhancements in mainly the Vis region, which is also the major absorbing region of the N719 dye. It can also be observed that the peak/major enhancement pattern depends on the amount of PNPs loading, and thus, the distribution of PNPs. We attribute these observed effects to the complex composition of our PNPs of wide particle size range and varied shapes, such that different LSPR modes were generated with possible multiple LSPR modes from the interaction of these generated modes [21], depending on the PNPs distribution. These complex interactions can be constructive/harmonic or destructive, and possibly responsible for the different peak regions of enhancement. Still in Fig. 4.7 b) the amount of enhancement decreases with increasing amount of PNPs loading. This supports the reducing charge injection efficiency effect of the PNPs; especially so in the 5 % PNPs loaded sample in which there is no observed enhancement in the absorbing region of the dye, but observed enhancement effect from 720 nm into the IR region. This indicates that in this region, the PNPs are behaving as direct sensitizers directly injecting electrons into the CB of the TiO_2 SCM.

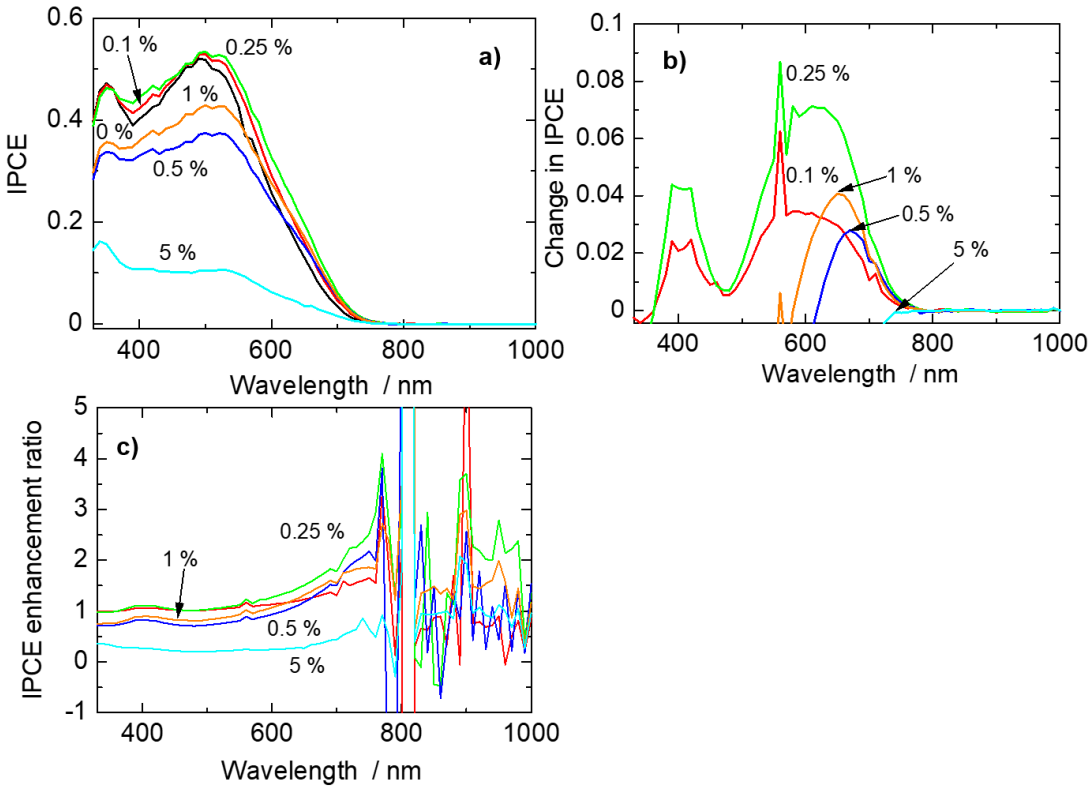

Fig. 4.7 a) IPCE spectra of DSSCs with various amounts of Ag@TiO_2 loadings. **b)** [IPCE of plasmonic DSSCs] – [IPCE of pristine sample]. **c)** [IPCE of plasmonic DSSCs] / [IPCE of pristine sample].

The PNPs enhancement of cell performance was estimated at particular wavelength regions by dividing the IPCEs of the plasmonic cells over the pristine sample (termed as enhancement ratio) to obtain the spectra of Fig. 4.7 c). In Fig. 4.7 c), we observe the same pattern of enhancement as discussed above with the highest enhancement in the IR range of about x2 (although very minimal in quantum terms as observed in Fig. 4.7 b)), within the limit of our measuring range. Although the contributory effect of this is almost negligible, it is still relevant to discuss the IPCE activity observed in this energy rich region for the

possibility of enhancing this activity which can greatly enhance PCE with even the minimum significant enhancement. In addition, in a similar yet unreported work in our lab, we used uniform size (20 nm) and shape (circular) Ag@TiO_2 NPs (with thin, ~ 2 nm TiO_2 shell), we observed a different enhancement pattern in this region. There was reversal of enhancement effect, with the 5 % PNPs loaded sample recording the highest enhancement effect with as much as 25 times over the pristine sample. The plasmonic enhancement effect is this region is thought to be dominated by surface plasmon polaritons (SPPs) from SPR effect, mainly in the form of hot electrons [21, 38, 39]. It has been reported that for the efficient propagation of the SPP for the efficient generation and injection of these hot electrons, periodicity and small size (< 40 nm) nanostructures are required [38]. Thus, the complex, random and largely large particle size (~ 40 nm) distributions of our PNPs in this work do not support the efficient enhancement performance effect in the IR region.

4.3.7 Effect of PNPs in thicker photoanodes

The plasmonic effect pattern with thicker (9 µm) photoanodes was also investigated. A summary of the results from this investigation is shown in Table 4.2 and Fig. 4.8. From Table 4.2, similar plasmonic effect patterns on the key performance parameters are seen, although less obvious to an extent. One obvious change is the higher V_{oc} values in these thicker photoanode samples due to more absorbing material (dye, PNPs and TiO_2 NPs) generating more charge carriers. These already high V_{oc} values will limit the extent to which the PNPs can modify the V_{oc}s of these plasmonic DSSCs as a result of the limiting factor of finite DOS. This would affect the inductive effect by these PNPs for the optimal DOS modification. Thus, this would be responsible for the minimal difference in the V_{oc} between the pristine sample and the 0.1 % PNPs loaded sample, compared to their analogues in the 5.5 µm thick photoanodes. An effect also observed in the relatively lower difference in J_{sc} values between these samples. However, it appears there is a possibility that with the appropriate adjustment

in PNPs concentration higher J_{sc} and PCE can be obtained, based on the discussions made so far. In addition, the highest PCE was obtained in the sample with the highest J_{sc}, unlike in the thinner photoanode samples it was found in the optimal balance of the negative and positive plasmonic induced effects on the values of the key cell performance parameters of J_{sc}, V_{oc} and *FF*. With this, it can also be suggested that with the appropriate adjustment in concentration of the PNP, commensurate with the increase in photoanode thickness, this optimal sample with a higher PCE can be obtained. But what is clear in these differing results is that the distribution (in its broadest sense, and as defined under section 4.3.3) is very critical to obtaining an optimal plasmonic cell with a very high PCE. It appears the V_{oc} in the thicker photoanode is at the maximum value for this system and hence the observed differences may be as a result of band fluctuation[40]. This is supported by the IPCE change spectra in Fig 4.8, in which only the 0.1 % PNPs loaded sample shows enhancement effect in the dye absorbing visible region, suggesting poor charge injection efficiency in the rest of the plasmonic samples as a result of extreme upward shift of the fermi level of the photoanodes of these cells.

Table 4.2: Key DSSC performance parameters from I-V and EIS characterizations of 9 µm-thick photoanodes

Amt. of Ag@TiO_2 /wt. %	J_{sc} /mA cm^{-2}	V_{oc} /V	*FF*	PCE /%	R_{ct} /Ω	τ_n /ms	η_{cc}
0	7.44	0.807	0.573	**4.39**	6.6	6.6	0.223
0.1	8.09	0.801	0.554	**4.58**	7.1	8.0	0.236
0.25	6.16	0.790	0.614	3.82	8.8	10.1	0.277
0.5	4.54	0.785	0.650	2.95	13.8	10.1	0.375
1	5.78	0.823	0.649	3.93	12.0	10.1	0.343
5	2.37	0.815	0.710	1.75	33.4	12.6	0.592

In addition, comparing the spectra of sample 0.1 % in Fig. 4.8 and Fig. 4.7 b), we observe different patterns of enhancement, especially with regards to the wavelength regions of enhancement peaks and troughs. This supports the claim of destructive and/or constructive interaction of the effects of the PNPs, with strong dependence on the distribution of the PNPs.

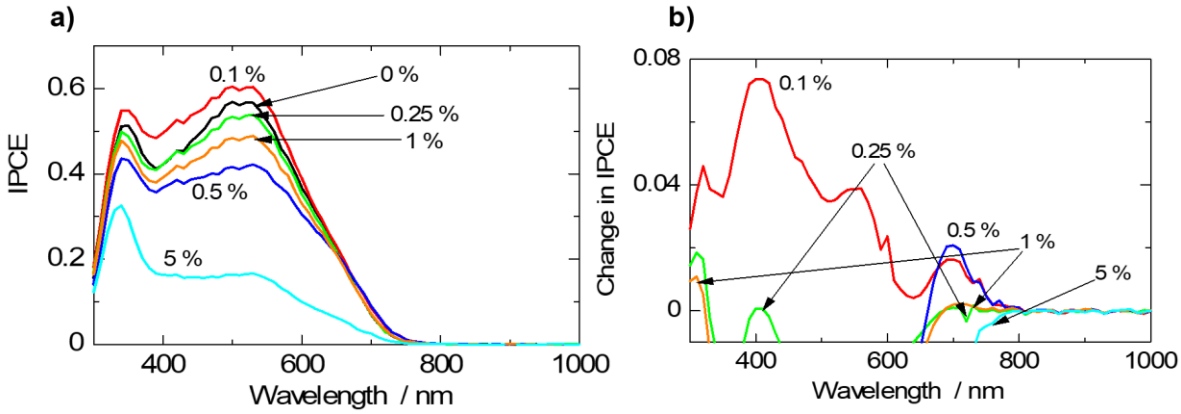

Fig. 4.8 Effect of the plasmonic nanoparticles on the performance of the 9 µm-thick photoanode DSSCs with respect to wavelength from: **a)** IPCE spectra; **b)** [IPCE of plasmonic DSSCs] – [IPCE of pristine sample].

4.4 Conclusion

We prepared a complex composition of Ag@TiO_2 C-S PNPs of varying shapes and sizes to study the effects of plasmonic nanostructures on the performance of DSSCs. The results showed complex PNPs effect patterns, with further complication from the complex composition of these PNPs. Nevertheless, using extended characterizations, wide range

PNPs-loaded cells and a systematic approach of analysis of the results some clear effect patterns on key performance parameters were observed. The thin TiO_2 shell (~ 2 nm) proved to be a good protection to the core plasmonic Ag against corrosive effect of the I^-/I_3^- electrolyte and still allowed for transmission of its plasmonic effect. The PNPs induced a panchromatic absorbance by the N719 dye. PL spectroscopy showed electron-sink effect of the PNPs. The electron-sink property showed a complex effect pattern on the performance of the cells: the trapping of photogenerated electrons onto the plasmonic Ag NPs caused effective charge separation, increased electron lifetime and caused an upward shift of the fermi level of the TiO_2, with a consequent increase in V_{oc}. Increase in V_{oc} was good for higher PCE but beyond a certain threshold, it caused poor injection of photogenerated electrons into the CB of TiO_2 by the dye. In addition, the strong electromagnetic field generated by the (L)SPR effect of the PNPs can also induce shallow or deep trap states in the TiO_2 SCM, which can also affect the CB edge position and electron kinetics, which explained some of the apparent deviations from the general plasmonic effect patterns observed in this research. Of particular interest is the lowering of V_{oc} at 0.1 and 1 % PNPs loadings with accompanying increased charge recombination, attributed to induced deep traps. The PNPs also increased *FF* and η_{cc}, attributed to generation of shallow trap states and trapping-detrapping of photogenerated electrons by the core Ag NPs. The highest enhanced PCEs of 4.26 and 4.36 % at 0.1 and 0.25 % loaded PNPs samples, respectively (from the pristine sample PCE value of 3.54 %), had their major enhancement effect from efficient charge injection and a balance of the negative and positive effects of the PNPs on key PCE parameters. These results suggest that there is the possibility of obtaining higher plasmonic PCEs by focusing on the balance of positive and negative effects of PNPs instead of the conventional focus on obtaining the highest plasmonic generated J_{sc}s. However, it was also observed that the relative lower PCE of the 0.1 % sample was as a result of increased recombination of the

abundantly generated and injected electrons. Hence, with the appropriate steps to curtail this increased recombination, very high PCEs can be obtained from plasmonic DSSCs.

The PNPs showed very little IPCE activity in the energy-rich NIR region and independent of the amount of PNPs loading. This was attributed to large PNPs (~ 40 nm) and complex composition of the PNPs with no periodicity to promote efficient generation and propagation of SPPs, which are thought to be mainly responsible for the cell activity in the region. Thus, the results of this work has reaffirmed some effects of plasmonic nanostructures on the performance of DSSCs; supported some predicted effects and revealed some yet unobserved effects. Hence, it has deepened the understanding of the effects of plasmonic nanostructures and would serve as a good guide in the field of plasmonic DSSCs and related fields.

References

1. M. Grätzel, The advent of mesoscopic injection solar cells, *Prog. Photovolt: Res. Appl.*, **14** (2006) 429-442.

2. A. Hagfeldt, G. Boschloo, L. Sun, L. Kloo and H. Pettersson, Dye-sensitized solar cells, *Chem. Rev.*, **110** (2010) 6595–6663.

3. M. L. Parisi, S. Maranghi and R. Basosi, The evolution of the dye sensitized solar cells from Grätzel prototype to up-scaled solar applications: A life cycle assessment approach, *Renew. Sust. Energ. Rev.*, **39** (2014) 124-138.

4. B. O'Regan and M. Gratzel, A low-cost, high-efficiency solar cell based on dye-sensitized colloidal TiO_2 films, *Nature*, **353** (1991) 737-740.

5. M. Grätzel, Recent Advances in sensitized mesoscopic solar cells, *Acc. Chem. Res.*, **42** *(*2009) 1788-1798.

6. M. Ye, X. Wen, M. Wang, J. Iocozzia, N. Zhang, C. Lin and Z. Lin, Recent advances in dye-sensitized solar cells: from photoanodes, sensitizers and electrolytes to counter electrodes, *Mater. Today*, **18** (2015) 155-162.

7. Best research-cell efficiencies. *NREL* https://www.nrel.gov/pv/assets/images/efficiency-chart.png (2017).

8. X-D. Gao, X-M. Li, X-Y. Gan, *InTech*, DOI 10.5772/51633, (2013) 169-202.

9. W. R. Erwin, H. F. Zaricka, E. M. Talbert and R. Bardhan, Light trapping in mesoporous solar cells with plasmonic nanostructures, *Energy Environ. Sci.*, **9** (2016) 1577-1601.

10. S. V. Boriskina, H. Ghasemi and G. Chen, Plasmonic materials for energy: From physics to applications, *Mater. Today*, **16** (2013) 375-386.

11. D. N. Joshi, S. Mandal, R. Kothandraman and R. A. Prasath, Efficient light harvesting in dye sensitized solar cells using broadband surface plasmon resonance of silver nanoparticles with varied shapes and sizes, *Mater. Lett.*, **193** (2017) 288-291.

12. J. Villanueva-Cab, J. L. Montaño-Priede and U. Pal, Effects of plasmonic nanoparticle incorporation on electrodynamics and photovoltaic performance of dye sensitized solar cells *J. Phys. Chem. C*, **120** (2016) 10129-10136.

13. L. Zhao, C. Zhong, Y. Wang, S. Wang, B. Dong and L. Wan, Ag nanoparticle-decorated 3D flower-like TiO_2 hierarchical microstructures composed of ultrathin nanosheets and enhanced photoelectrical conversion properties in dye-sensitized solar cells, *J. Power Sources*, **292** (2015) 49-57.

14. S. P. Lim, A. Pandikumar, H. N. Lim, R. Ramaraj and N. M. Huang, Boosting photovoltaic performance of dye-sensitized solar cells using silver nanoparticle-decorated N,S-co-doped-TiO_2 photoanode, *Sci. Rep.* **5** (2015) 11922(1-14).

15. S. Ramakrishna, M. Pelton, S. K. Gray and T. Seideman, Plasmon-enhanced electron injection in dye-sensitized solar cells, *J. Phys. Chem. C*, **119** (2015) 22640-22645.

16. S. P. Lim, A. Pandikumar, N. M. Huang and H. N. Lim, Enhanced photovoltaic performance of silver@titania plasmonic photoanode in dye-sensitized solar cells, *RSC Adv.*, **4** (2014) 38111-38118.

17. Q. Xu, F. Liu, Y. Liu, K. Cui, X. Feng, W. Zhang and Y. Huang, Broadband light absorption enhancement in dye-sensitized solar cells with Au-Ag alloy popcorn nanoparticles, *Sci. Rep.*, **3** (2013) 2112(1-7).

18. H. Choi, W. T. Chen and P. V. Kamat, Know thy nano neighbor. Plasmonic versus electron charging effects of metal nanoparticles in dye-sensitized solar cells, *ACS Nano*, **6** (2012) 4418-4427.

19. J. Qi, X. Dang, P. T. Hammond, and A. M. Belcher, Highly Efficient Plasmon-Enhanced Dye-Sensitized Solar Cells through Metal@Oxide Core–Shell Nanostructure, *ACS Nano*, **5** (2011) 7108-7116.

20. N. C. Jeong, C. Prasittichai and J. T. Hupp, Photocurrent enhancement by surface plasmon resonance of silver nanoparticles in highly porous dye-sensitized solar cells, *Langmuir*, **27** (2011) 14609-14614.

21. I-K. Ding, J. Zhu, W. Cai, S-J. Moon, N. Cai, P. Wang, S. M. Zakeeruddin, M. Grätzel, M. L. Brongersma, Y. Cui and M. D. McGehee, Plasmonic dye-sensitized solar cells, *Adv. Energy Mater.*, **1** (2011) 52-57.

22. S. D. Standridge, G. C. Schatz and J. T. Hupp, Toward plasmonic solar cells: protection of silver nanoparticles via atomic layer deposition of TiO_2, *Langmuir*, **25** (2009) 2596-2600.

23. J-W. Yoon, T. Sasaki and N. Koshizaki, Dispersion of nanosized noble metals in TiO2 matrix and their photoelectrode properties, *Thin Solid Films*, **483** (2005) 276-282.

24. C. Wen, K. Ishikawa, M. Kishima and K. Yamada, Effects of silver particles on the photovoltaic properties of dye-sensitized TiO2 thin films, *Sol. Energy Mater. Sol. Cells*, **61** (2000) 339-351.

25. G. Zhao, H. Kozuka and T. Yoko, Sol-gel preparation and photoelecrochemical properties ofTiO_2 films containing Au and Ag particles, *Thin Solid Films*, **277** (1996) 147-154.

26. X. Wei, P. S. Nbelayim, G. Kwamura, H. Muto and A. Matsuda, Ag nanoparticle-filled TiO2 nanotube arrays prepared by anodization and electrophoretic deposition for dye-sensitized solar cells, *Nanotechnology*, **28** (2017) 135207-135214.

27. N. Nyein, W. K. Tan, G. Kawaura, A. Matsuda and Z. Lockman, Anodic Ag/TiO_2 nanotube array formation in NaOH/fluoride/ethylene glycol electrolyte as a photoanode for dye-sensitized solar cells, *Nanotechnology*, **27** (2016) 355605-355616.

28. G. Kawamura, H. Ohmi, W. K. Tan, Z. Lockman, H. Muto and A. Matsuda, Ag nanoparticle-deposited TiO_2 nanotube arrays for electrodes of dye-sensitized solar cells, *Nanoscale Res. Lett.*, **10** (2015) 219 (1-6).

29. I. Pastoriza-Santos, D.S. Koktysh, A.A. Mamedov, M. Giersig, N.A. Kotov and L.M Liz-Marzán, One-pot synthesis of Ag@ TiO_2 core− shell nanoparticles and their layer-by-layer assembly, *Langmuir*, **16** (2000) 2731-2735.

30. A. Wood, M. Giersig and P. Mulvaney, Fermi level equilibration in quantum dot−metal nanojunctions, *J. Phys. Chem. B*, **105** (2001) 8810–8815.

31. M. K. Nowotny, L. R. Sheppard, T. Bak and J. Nowotny, Defect chemistry of titanium dioxide. Application of defect engineering in processing of TiO_2-based photocatalysts, *J. Phys. Chem. C*, **112** (2008) 5275-5300.

32. F. J. Knorr, C. Mercado and J. L. McHale, Trap-state distributions and carrier transport in pure and mixed-phase TiO_2: Influence of contacting solvent and interphasial electron transfer, *J. Phys. Chem. C*, **112** (2008) 12786-12794.

33. C. Mercado, Z. Seeley, A. Bandyopadhyay, S. Bose and J. L. McHale, Photoluminescence of dense nanocrystalline titanium dioxide thin films: effect of doping and thickness and relation to gas sensing, *ACS Appl. Mater. Interfaces*, **3** (2011) 2281-2288.

34. B. Roose, S. Pathak and U. Steinr, Doping of TiO_2 for sensitized solar cells, *Chem. Soc. Rev.*, **44** (2015) 8326-8349.

35. M. Borgwardt, M. Wilke, T. Kampen, S. Mahl, W. Xiang, L. Spicca, K. M. Lange, I. Y. kiyan and E. f. Aziz, Injection kinetics and electronic structure at the n719/tio2 interface studied by means of ultrafast XUV photoemission spectroscopy, *J. Phys. Chem. C*, **119** (2015) 9099-9107.

36. Z. Ning, Q. Zhang, W. Wu, H. Pei, B. Liu, and H. Tian, Starburst triarylamine based dyes for efficient dye-sensitized solar cells, *J. Org. Chem.*, **73** (2008) 3791-3797.

37. S. A. Haque, Y. Tachibana, D. R. Klug and J. R. Durrant, Charge recombination kinetics in dye-sensitized nanocrystalline titanium dioxide films under externally applied bias, *J. Phys. Chem. B*, **102** (1998) 1745–1749.

38. X-C. Ma, Y. Dai, L. Yu and B-B. Huang, Energy transfer in plasmonic photocatalytic composites, *Light Sci. Appl.*, **5** (2016) 1-13.

39. J. Li, S. K. Cushing, P. Zheng, F. Meng, D. Chu and N. Wu, Plasmon-induced photonic and energy-transfer enhancement of solar water splitting by a hematite nanorod array, Nat. Commu., **4** (2013) 2651(1-8).

40. E. F. Schubert, Physical Foundations of Solid-State Devices, 2006 Edt., Rensselaer Polytechnic Institute Troy, New York, Chapter 16 (2006).

Chapter 5

Ag@TiO_2 nanowires-loaded dye-sensitized solar cells and their effects on the various performance parameters

5.1 Introduction

With current interest in green energy due to adverse environmental effects such as global warming, resulting from the major energy source of fossil fuels (> 85 %) [1]. In addition, there is a growing world population, and emerging and growing economies. These require alternative sustainable energy sources as the current major source is fast depleting and non-renewable. Current common proposed sustainable alternative energy sources include geothermal, biomass, hydropower, wind and solar/photovoltaics (PVs). Solar energy appears to be the best option with its critical advantages of being clean, inexhaustible, free of cost, hugely abundant with 3.89×10^{26} J s^{-1} from its thermonuclear fusion reactions (with about 1.367 kW m^{-2} reaching the earth's atmosphere: the solar constant). The solar constant, although a small portion, is still more than enough to meet the human energy needs if efficiently captured. This fact is aptly expressed by N. Lewis [2] in his statement that, "More energy from sunlight strikes Earth in 1 hour than all of the energy consumed by humans in an entire year." Dye-sensitized solar cells (DSSCs), among the 3rd generation of solar cells, and under the sub-generation of emerging PVs, have the attractive core advantages of facile preparation, low-cost fabrication, environmentally friendly and good performance under variable light conditions. However, DSSCs, although with high power conversion efficiencies (PCEs), are still competitively lower, with a certified record PCE of 11.9 % by SHARP [3] and a laboratory record PCE of 14.3 % by Kakiage *et al.* [4], compared to 14-22 %; 4-23 %;

and 25-46 % of the 1st generation, 2nd generation and concentrator sub-3rd generation solar cell [3], respectively.

Plasmonic DSSCs were predicted to have very high PCEs from the unrivalled concentration of optical energy due to the localized surface plasmon resonance (LSPR) effect of plasmonic nanostructures (PNSs). PNSs such as metallic nanostructures of sub-wavelength sizes have mobile conduction band (CB) electrons on their surfaces which are easily displaced. The displacement of these electrons causes polarization of a PNS. The restorative coulombic force of the nucleus and the susceptibility of the electrons to re-displacement causes oscillation of the electrons about the nanostructure, forming a plasmon. When light of the same frequency as the oscillation interacts with the plasmon, resonance occurs, referred to as LSPR, which generates an extremely intense electromagnetic field.

The LSPR effect can enhance the light absorption and hence carrier generation to ultimately enhance PCE of DSSCs via basically four proposed mechanisms: a radiative decay mechanism via far-field photon scattering and near-field photon coupling with vicinal optical materials; and a non-radiative decay mechanism by the generation of electron-hole pairs via hot-electron transfer and plasmon resonant energy transfer [5-7].

There have been many reported works on plasmonic DSSCs [5, 7, 8] since the probably first significant works on plasmonic DSSCs by C. Wen *et al.* [9]. Almost all of these reported works have shown PCE enhancements over their respective reference samples. However, the highest plasmonic DSSC PCE of 10.8 % [10] is still lower than many pristine state-of-the-art DSSCs, such as the record DSSC of Kakiage *et al.* [4]. In addition, although there is a vast amount of publications on plasmonic DSSCs there is still significant amount of discrepancies/controversies regards the effect of PNSs in DSSCs [7, 8. 11] with examples including, the interpretation of reducing cell performance at high PNS loadings and effects on

key cell performance parameters. Thus, these issues suggest the need for further research on plasmonic DSSCs.

In our previous studies we have used uniformly sized and shaped Ag@TiO_2 core-shell nanoparticles (C-S NPs) [11] and multi-sized and-shaped Ag@TiO_2 C-S NPs in an effort to understand the effects of PNSs in DSSCs. In the former we observed that the uniform particle size with undulating TiO_2 shell of the NP promoted increasing cell performance in the near-infrared (NIR) region with increases in PNP loading, while in the latter destructive interference effect of multi-modes LSPRs suppressed performance in the NIR region.

In this study, we have employed Ag@TiO_2 C-S nanowires (NWs). Our hypothesis being that since the LSPR effect is affected by the composition, shape, size and environment, the NW morphology may exhibit a different effect pattern from the NPs used in our previous studies mentioned above. In addition, since NWs have little or no inter-grain boundaries, we thought this will aid in the efficiently transport of the abundant LSPR-enhanced photo-generated electrons and consequently lead to higher DSSC performance/PCE enhancement.

Plasmonic DSSCs employing the NW morphology are relatively limited [5, 7]. Huang *et al.* [13] used Ag NW/TiO_2 composite films in their plasmonic DSSC study and observed an increase in PCE from 4.68 % to 5.31 % at 3 % PNS loading. They attributed the enhancement effect to be due to, mainly, the reduced charge transfer impedance at the TiO_2/dye/electrolyte interface and light scattering effects of the NWs. Sahu *et al.* [14] used Au-TiO_2 NW photoanode materials in their DSSCs and using characterization results from UV-Vis optical spectroscopy, I-V and dye loading proposed that enhancement of cell performance in the plasmonic sample was due to enhanced light absorbance probably from light scattering effect of the core Au nanostructures. Guo *et al.* [15] used 0.6 % Ag@SiO_2 NWs in TiO_2 photoanodes to enhanced cell performance via light scattering. They attributed poor cell

performance at higher NW loadings to reduced dye absorption, and low V_{oc} to insulating effect of SiO_2 shell. Chandrasekhar *et al.* [16] used 0.9 % Ag NWs in TiO_2 photoanodes to also enhance cell performance from improved light harvesting. They attributed poor performance at high PNW loadings to possible reduction in photoanode surface area and pore blocking.

In this study we have used wide-range PNW loadings and extended characterization to obtain a more in-depth and synergistic observation of the plasmonic effect on the performance of DSSCs. We obtained an enhanced cell performance at 0.1 % PNW loading by the optimal balance of the positive and negative effects of the PNWs, with a prediction of at least one more high-performing cell at another optimal PNW loading concentration via efficient charge injection with a lowered Fermi level (low V_{oc}).

5.2. Experimental

5.2.1 Synthesis of Ag@TiO_2 C-S NWs

The Ag@TiO_2 PNWs were prepared using a modified method from literature [10] using a solvothermal technique. Typically, 88 ml of ethylene glycol (dehydrated, Wako; ≥ 99.5%) was measured into a 1 L stainless steel vial and 2.55 g of $AgNO_3$ (Wako; ≥ 99.8% min.) was added. The mixture was sealed and stirred for about 10 min at 350 rpm. A 2.52 g $Ti(OC_4H_9)_4$ (Wako; ≥ 95.0%) was subsequently added and further stirred for about 15 min until all the $AgNO_3$ had dissolved. The reaction mixture was sealed once more and put in an oven at 270 °C for 14 h. It was then cooled to room temperature. The product was put through a series of 4 cycles of washing in ethanol (by sonication) and centrifuging (8000 rpm; 40 min). The final residue was dried at 80 °C for 12 h in a vacuum oven to obtain the C-S NWs.

5.2.2 Pastes and photoanodes preparation

The pastes for the photoanode fabrication were prepared using planetary ball milling (Fritsch pulverisette 7) with an alumina mortar and balls. For the pristine paste (0 %), 1.74 ml of ethylene glycol (dehydrated, Wako; ≥ 99.5%) was added to 1.0 g of TiO_2 P25 (Sigma-Aldrich; 21 nm; ≥ 99.5%) and milled at 500 rpm for 1 hr; 1.69 g of citric acid (Chameleon reagent; anhydrous, ≥ 99.5%) was added and milled for another 1 h. For the Ag@TiO_2-loaded pastes, the same preparation procedure was used with the appropriate mass of Ag@TiO_2 NWs replacing TiO_2 P25 to obtain the Ag@TiO_2 NW-loaded pastes of 0.1, 0.25, 0.5, 1, 3 and 5 % loading concentrations.

The photoanodes were prepared via doctor blade coating on FTO glass substrates (85 % T, 9 Ω/□; 3 × 2 cm). The FTO substrates were first cleaned by RCA treatment and coated with a TiO_2 buffer layer by treatment in 0.04 mol L^{-1} $TiCl_4$ (Wako; ≥ 99.0%) solution at 70 °C for 30 min (with 2 cm^2 active area masking), washed with water and heat-treated at 450 °C for 1 h. The buffer layer-treated FTO substrates were then coated with the pastes using a 60 μm thick scotch tape masks, each with a circular active area diameter of 10 mm (0.785 cm^2). For uniformity and reproducibility, the squeegee was maintained at a constant distance over the substrate and then applying an 80 g steel block weight to make contact with the substrate. The blade was drawn at a rate of 2.5 mm s^{-1} to spread the paste. The samples were dried stepwise on a hot plate at ambient temperature, 60 °C and 120 °C, for 5 min each; and finally heat-treated together at 500 °C for 1 h. The calcined samples were washed with ethanol and dried with a hot blower. For dye sensitization, the dried samples were immersed in 0.3 mmol L^{-1} of N719 dye (ALDRICH; 65 mol% dioxole), in a 1:1 solvent system of acetonitrile (Wako; 99.5 %) : *tert*-butyl alcohol (Wako; 99.0 %), for 24 h. The dye-sensitized photoanodes were rinsed with acetonitrile to remove excess dye, and dried afterwards using a hot blower.

5.2.3 DSSCs Assembling

Sandwich-type cells were prepared using a 50 μm plastic spacer (DuPont, Himilan) with a circular open diameter of 12 mm (1.13 cm^2). The electrodes were sealed on a hot plate at 105 °C, with a 1 kg weight load for about 5 min. The CEs were prepared using RCA-cleaned FTO substrates with holes drilled 11.5 mm apart, and Pt coating applied with a sputter coater (Hitachi E-1030 ion sputter) at 15 mA for 600 s. An acetonitrile solvent-based electrolyte, composed of 0.05 mol L^{-1} iodine (Aldrich; ≥ 99%), 0.1 mol L^{-1} lithium iodide (Strem Chemicals; anhydrous, ≥ 98 %), 0.6 mol L^{-1} 1, 2-dimethyl-3-propylimidazolium iodide (TCI; > 98 %), and 0.5 mol L^{-1} 4-*tert*-butylpyridine (Aldrich; 96 %), was injected into the cells and sealed with a piece of the spacer and scotch tape. Dye-sensitized solar cells with Ag@TiO_2 PNW loadings of 0.1, 0.25, 0.5, 1, 3 and 5 %, in addition to a reference un-doped DSSC of 0 %, were obtained.

5.2.4 Characterization

The optical absorption characteristics of the PNPs and photoanodes were evaluated using a JASCO V-670 UV-Vis-NIR spectrophotometer. The particle size, size distribution and core-shell structure of the Ag@TiO_2 C-S NWs were observed using a JEOL JEM-2100 F TEM. A Rigaku Ultima IV R285S XRD was used to study the composition and crystallinity of the C-S NWs. The PL spectroscopy of the photoanodes was evaluated using a He-Cd laser (325 nm) as the excitation source. The luminescence was evaluated by a multi-channel CCD spectrometer. The I-V characteristics of the cells were evaluated using an ADCMT 6244 DC Voltage/Current Source/Monitor and an HAL-320 W solar simulator (Asahi spectra) with a 300 W xenon lamp and an air-mass 1.5 global filter. The solar simulator was calibrated to an intensity of 100 mW cm^{-2} (1 sun), using a One sun checker (Asahi CS-40). The IPCE characterization was done via the DC method using a Bunkoukeiki SM-250KB spectrometer

with a Keithley 2401 source meter and an irradiation flux of 2.0 x 10^{15} photons, with masking of active area of 1 cm^2. A Hitachi S-4800 FE-SEM was used to study the morphology and thickness of the photoanode coatings. The electron transport dynamics of the active cells was evaluated using an electrochemical impedance spectroscopy (EIS) equipment (Solartron SI 1287 Electrochemical Interface and Solartron1255B Frequency Response Analyzer) under bias open circuit voltage (V_{oc}) within the frequency range of 0.1 Hz to 1 MHz, and an AC amplitude of 40 mV; and under light irradiation of 1 SUN.

5.3 Results and discussion

5.3.1 Morphological, structural and corrosion stability studies of the NWs

Figure 1 a) is the FE-SEM image of the NWs showing diameters between 80-300 nm. They have high aspect ratios of lengths in 100s of micrometers. Figure 5.1 b) is the TEM-EDX mapping image showing the core-shell structure of Ag (red) and TiO_2 (green) of diameter of ~ 60 nm and thickness of ~ 10 nm, respectively. Figure 5.1 c) is the HR-TEM image of the tip of the NW sealed by the TiO_2 shell. The C-S structure protect the plasmonic Ag core from aggregating during the high temperature heat-treatment photoanode preparation and from the corrosive effect of the I^-/I_3^- electrolyte, but still allow for the LSPR effect. Thus, it is significant that the ends of the NWs are sealed. In Fig. 5.1 d) the XRD patterns of the NWs show only crystalline peaks of cubic Ag of (111), (200), (220) and (311) planes (JCPDS No. 04-0783), suggesting an amorphous TiO_2 shell. At a heat treatment of 300 $^{\circ}$C to remove organic

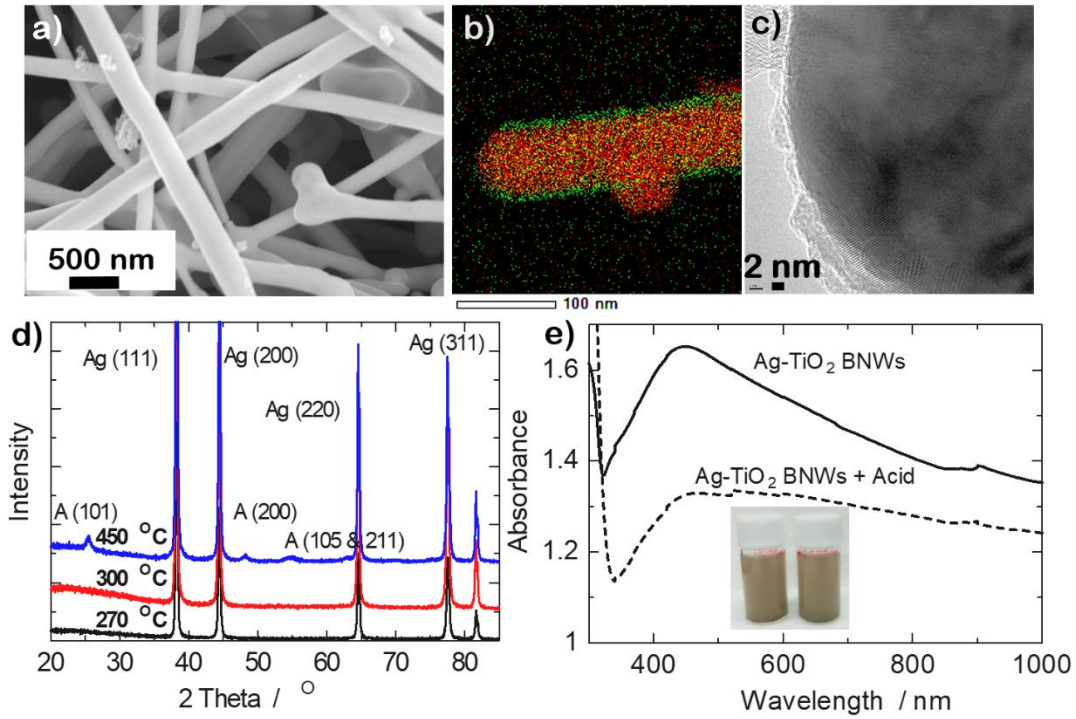

Fig. 5.1 a) SEM image of the NWs; **b)** TEM-EDX mapping image of a NW showing the Ag (red)-TiO_2 (green) core-shell structure; **c)** HR-TEM image of the tip of the NW showing a sealed end; **d)** XRD patterns of the NWs at various heat treatment temperatures with crystallization of the TiO_2 shell after 450 °C; and **e)** Optical spectroscopy of suspensions of the NWs showing acid (corrosion) stability with LSPR peaks before and after acid treatment; inset image: NWs suspension before (left) and after (right) acid treatment.

component, based on themogravimetric analysis (results not provided here), the shell is still amorphous until after 450 °C heat treatment when it crystallizes into the more preferred anatase (A) phase and (101) plane (the most intense anatase peak) (JCPDS No. 21-1272).

Crystallization of the TiO_2 shell is necessary for the efficient conduction of electrons. The Ag peaks are still prominent at 450 °C, indicating the protective effect of the TiO_2 shell with respect to heat. We tested the protective effect of the shell against corrosion via an acid stability test (1 % HNO_3; 24 h). The results are shown in Fig. 5.1 e). Both absorbance spectra of NW suspensions in ethanol before and after acid treatments show LSPR peaks around 450 nm, indicating the plasmonic Ag core was preserved. However, there is about 19 % decrease in absorbance intensity of the acid treated sample, this has be attributed to the dilution effect of the added acid, and its consequent effect on the interacting (constructive and/or destructive) different LSPRs within the suspension. The stability is confirmed visually with the inset images having the same colour, before and after acid treatments. Standridge *et al.* [17] made a similar study and observed that an I^-/I_3^- solution dissolved unprotected plasmonic Ag coatings within 1 h, but 7.7 nm, or 5.8 nm with Al_2O_3 adhesive, TiO_2 protective coating prevents the dissolution of the plasmonic Ag. Thus our 24 h stable acid-treated NWs shows corrosion stability.

5.3.2 Optical studies on the plasmonic effects on the photoanode

At the Ag-TiO_2 junction electrons in the CB of TiO_2 flow to the Ag as a result of the lower Fermi level of Ag, as a metal, than the TiO_2, as a semiconductor. This continues until their two Fermi levels equilibrate at a quasi Fermi level. Thus, the band structure between them becomes distorted, creating a potential energy barrier preventing the semiconductor-metal electron flow. This consequently creates a depletion layer which influences the band bending/distortion or Schottky barrier. This Schottky barrier can prevent the backward flow of electrons from the Ag to the TiO_2, effectively serving as an electron trap, described as the electron-sink effect. This electron-sink effect can prevent recombination of photogenerated electrons and prolong electron lifetime. In addition, it can cause the shifting of the CB edge/quasi Fermi level of the TiO_2.

We investigated the electron-sink effect of our prepared un-dyed plasmonic photoanodes using PL spectroscopy. This measures the luminescence from the electron-hole recombination after excitation. The results of 3 selected photoanodes are shown in Fig. 5.2 a). The plasmonic samples (of 0.1 and 0.25 % loadings) have lower (by about 83 %) PL intensities than the pristine sample of 0 % PNW loading. This indicates the trapping of excited electrons, in the plasmonic samples, severely reducing electron-hole recombination to release photoluminescence. Thus, effective electron-sink effect in the plasmonic photoanodes. The broadband PL spectra are attributed to trap states within the band gap, mainly from intrinsic oxygen vacancies in TiO_2 (responsible for its *n*-type semiconductor property [18]) which generate a varied range of electron-hole trap states within the forbidden energy band gap [19, 20] giving a broad range of transitions.

The photoanodes were subsequently dyed to evaluate the light absorbance enhancement effect of the PNWs in the photoanode. The results are shown in Fig. 5.2 b). All the plasmonic photoanodes have higher absorbances than the pristine sample, and the absorbance increases with increasing plasmonic NW loadings. This is attributed to the LSPR light absorbance enhancement effect of the plasmonic NWs on the photoanode.

The photoanodes were also characterize by FE-SEM to observe the distribution and orientation of the PNWs, shown in Fig. 5.2 c), and observed in the 1-5 % PNW loaded photoanodes. The PNWs were randomly distributed without aggregating to only a section of the photoanode, and also randomly oriented with at least in a direction towards the FTO substrate/eternal circuit. Thus, not completely horizontally oriented.

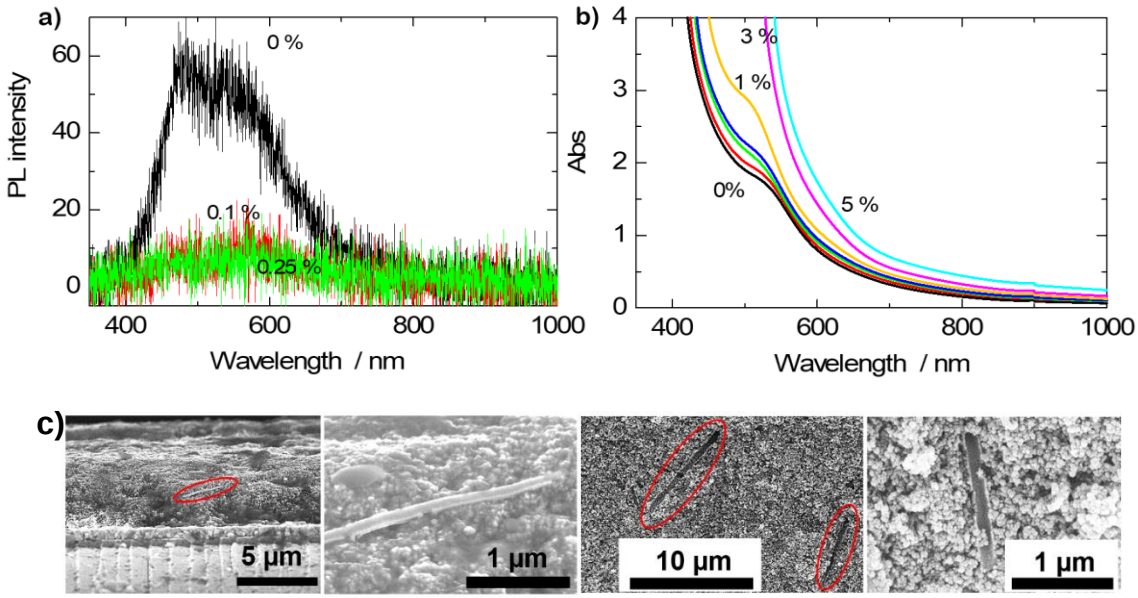

Fig. 5.2 a) PL spectra of un-dyed photoanodes showing electron-sink effect; **b)** Optical absorbance spectra of dyed photoanodes showing enhanced light absorbance in plasmonic photoanodes; **c)** FE-SEM images of photoanodes showing randomly distributed and oriented PNWs

To obtain the pristine effect of the PNWs on only the N719 dye, a series of tests involving mixtures of dye-PNWs in solution were carried out, shown in Fig. 5.3 a). When the dye is spiked with 3 mg of PNWs, the absorbance (orange spectrum) increases above both those of PNWs-only (red spectrum) and dye-only (black spectrum), although lower than the absorbance of the PNWs-only in the NIR region. This lower absorbance is attributed to a destructive interference effect of the interacting LSPRs generated. A further increase of the spiking to 4 mg of PNWs shows a further increase in absorbance (blue spectrum), but this

time with a slightly higher performance than the PNWs-only in the NIR, indicating a constructive interference of the LSPRs. Thus, the increasing absorbance with increasing PNWs loading is an indication of the light absorbance enhancement effect of the PNWs on the N719 dye. To corroborate this, an arithmetic addition of the absorbances of the dye-only and the PNWs-only, was plotted as a fifth spectrum (green) to compare. The first observation is that this spectrum showed the highest absorbance; which is an indication the PNWs-dye mixtures had an interacting effect between them such that, although the PNWs enhanced the

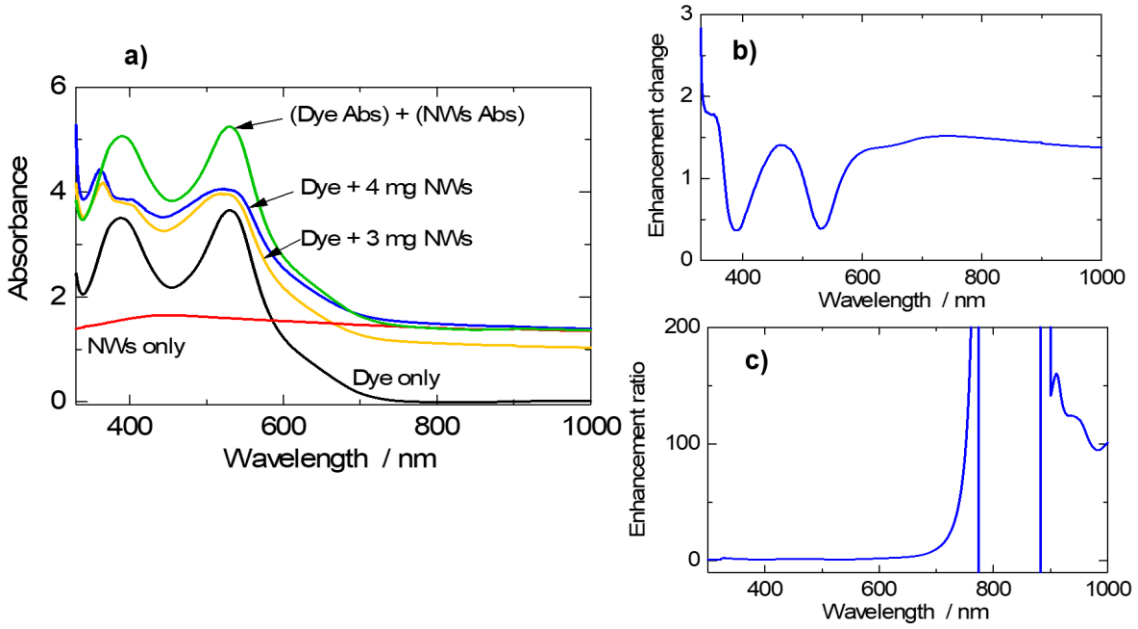

Fig. 5.3 Optical absorption spectra showing enhanced broadband light absorbance of the N719 dye of: **a)** PNWs-only in ethanol; dye-only; dye-PNWs mixtures; and arithmetic addition of dye-only and PNWs-only absorbances, respectively. **b)** [Absorbance of 4 mg PNWs dye] – [absorbance of dye-only]. **c)** [Absorbance of 4 mg PNWs in dye] ÷ [absorbance of dye-only].

absorbance of the dye they also reduced their expected higher combined absorbance as a result of this interaction. The second observation is that the absorbance peaks of the N719 dye around 388 and 530 nm of the dye-PNWs mixtures on one hand, are blue-shifted compared to those of the dye-only and arithmetic sum of dye and PNWs, on the other hand. This blue-shifting is an indication of a coupling interaction between the dye molecules and LSPR of the PNWs.

To investigate the magnitude and pattern of these enhancements, the dye-only absorbance (as a baseline) was deducted from the dye-4 mg PNWs absorbance to obtain Fig. 5.3 b). The most enhanced regions are the weak absorbing regions of the dye, while the least enhanced regions are the strong absorbing regions such as the peak regions of 388 and 530 nm. For the relative enhancement, the absorbance of the dye-PNWs mixture was divided by the absorbance of the dye-only to obtain Fig. 5.3 c).The results showed that the most enhanced region was the NIR region. Thus, by these patterns and magnitudes of light absorbance enhancement effect on the dye, these PNWs are expected to greatly enhance the photoelectron generation across the UV-Vis-NIR solar radiation region.

5.3.3 I-V characterization

The effects of the PNWs on the various performance parameters were investigated via I-V characterization. The results are shown in the first five columns of Table 5.1. The J_{sc} is a measure of the combination of efficient charge generation, injection, transport and extraction to generate power. The pristine sample (0 %) recorded the highest J_{sc} of 7.64 mA cm^{-2} and then the J_{sc} steadily reduces with increasing PNW loadings till the minimum of 3.68 mA cm^{-2} in the sample with 5 % PNW loading. There is however a slight increase in that of the sample with 1 % PNW loading, from 3.94 (of 0.5 % PNW loading) to 4.28 mA cm^{-2}. This apparent deviation from the reducing J_{sc} trend is explained with results from EIS characterization. The

decreasing J_{sc} with increasing PNS loadings is a common observation in plasmonic DSSCs, although usually it initially increases to a maximum and then begin the decreasing trend afterwards. However, the interpretation of this observation has been varied. Nevertheless, there is an increasing consensus of interpreting it as due to poor charge injection efficiency as a consequence of the upward shift of the electron-conducting-semiconductor material's (TiO_2) quasi Fermi level/CB edge[5] by the plasmonic nanostructures. We [11, 12] belong to this group of thought because it is usually supported by a higher V_{oc} in plasmonic DSSCs than those of their corresponding pristine samples. In this study all the plasmonic samples have higher V_{oc}s than the pristine sample, and since only the photoanodes of these cells were modified with PNWs, these higher values are due to the upward shift of their quasi Fermi levels/CB edges by the PNWs; with the inference that the V_{oc} of DSSCs is the potential difference between the quasi Fermi level of the photoanode (TiO_2) and the redox potential of the electrolyte [21, 22]. There is a minimum threshold energy difference requirement between the lowest unoccupied molecular orbital (LUMO) of the dye and the CB edge of TiO_2 (0.2 eV[23]) for the efficient injection of photogenerated charge. Thus, when this minimum threshold energy difference is exceeded, although photoelectrons will be generated by the dye, there is inefficient injection of these charges into the CB of TiO_2. Thus, the observed lower J_{sc} values for the plasmonic DSSCs are due to inefficient photogenerated-charge injection, since the optical absorbance spectroscopy evaluation results showed that the plasmonic photoanodes had higher absorbances than the pristine sample (Fig. 5.2 b)).

Table 5.1 I-V and EIS performance parameters of fabricated DSSCs.

Amt. of Ag@TiO_2 NWs /wt.%	J_{SC} /mA cm^{-2}	V_{oc} /V	*FF*	PCE /%	R_{ct} /Ω	τ_n /ms	η_{cc}
0	7.64	0.836	0.568	4.63 ± 0.02	7.9	6.3	0.208
0.1	6.97	0.857	0.661	5.03± 0.15	7.9	6.3	0.208
0.25	6.27	0.865	0.660	4.56± 0.07	8.9	8.0	0.229
0.5	5.79	0.858	0.621	3.94± 0.25	9.2	6.3	0.235
1	5.82	0.875	0.660	4.28± 0.04	10.3	8.0	0.255
3	4.17	0.859	0.657	3.18± 0.37	15.1	12.6	0.335
5	3.68	0.848	0.703	2.79± 0.11	25.5	15.9	0.459

As mentioned already, the J_{sc} of the plasmonic DSSCs usually rises from a minimum to surpass that of the pristine sample and reducing thereof with increasing PNS loadings [11-13, 15, 24]. This trend is consistent with the upward shifting of the CB edge when explained with the enhanced photogeneration effect of the PNSs. In this study the decreasing trend begins immediately after the pristine sample, 6.97 mA cm^{-2} of 0.1 % NW loading (from 7.64 mA cm^{-2} of the pristine sample). This is attributed to the intrinsic high V_{oc} of this batch system of DSSCs causing poor charge injection efficiency; with the pristine sample having a V_{oc} of 0.836 V (6.6 µm), compared to our previous publications [11, 12] with pristine samples V_{oc}s of 0.709 (6.6 µm) and 0.773 V (5.5 µm), respectively, although painstaking efforts were taken to ensure the same preparation conditions, barring their different PNSs and climatic season in which they were prepared. The high V_{oc}s recorded are attributed to conditions that promoted a slight decrease in deep trap states density, usually from oxygen vacancies, from the delicate and difficult-to-control electronic properties of TiO_2 nanocrystals, resulting in an upward shift of the Fermi level and thus an increase of the V_{oc} [18, 19, 25, 26].

In addition, the increasing V_{oc} is limited by the limiting factor of finite density of states of the CB of TiO_2 which limits the shifting of the quasi Fermi level. Thus, the DSSC system in this study seem to have reached the V_{oc} limit and hence the decreasing V_{oc} trend with increasing PNS loading, although present it is not clearly seen, with apparent deviations at 0.5, 3 and 5 % NW loadings. These apparent deviations are attributed to extra randomly generated and distributed trap states by the PNWs [9, 25, 27] and depending on the type and distribution can affect the V_{oc} and charge recombination of the cell. Oxygen vacancies, titanium interstitials and reduced crystal surfaces in TiO_2 generate trap states, mainly in the form of Ti^{4+} and Ti^{3+}, and the formation of trap states can be catalyzed by PNSs. Shallow traps are mainly composed of Ti^{4+} and make up the lower edge of the TiO_2 CB; they enhance charge conductivity. The Ti^{3+} species is located ~ 0.5 eV below the CB edge; they also aid in the *n*-type characteristics of TiO_2 but also act as charge recombination centers/electron traps due to their location away from the CB edge. One typical route for the formation of the Ti^{3+} species is a photogenerated hole/hot hole neutralizing and desorbing oxygen to activate the Ti^{3+} species [25, 28]. The formation of Ti^{3+} will lower the Fermi level and hence reduce V_{oc}, with a consequent increase in charge recombination, but with enhanced charge injection efficiency. Thus, we propose the LSPR-catalyzed random formation of Ti^{3+} is responsible for the apparent deviations in the increasing V_{oc} trend with increasing PNW loadings in this study.

The fill factor, *FF*, is defined as, $FF = [I_{max} \times V_{max}] / [J_{sc} \times V_{oc}]$, where I_{max} and V_{max} are the current and voltage at the maximum power point of the I-V curve. Thus, the *FF* is affected by almost all components of the cell and it is mainly affected by resistances from any part of cell; with reduced values recorded from increased resistance. Thus, it can indicate the efficiency of charge transport within the cell. Since the only major difference among the cells is the amount of PNW loadings, the differences in *FF* among these cells is attributed to the PNWs. From Table 5.1, the *FF*s of all the plasmonic cells are higher than the pristine sample

with a trend of increasing value with increasing PNW loadings. This is attributed to efficient electron transport by the wire morphology (1D morphology: no/fewer inter-grain boundaries to impede electron transport and increase charge recombination. The apparent deviations from the increasing trend at 0.5 and 3 % PNW loadings are attributed to generated shallow trap states which increased charge trapping and recombination significantly to affect their *FF*s. Fig. 5.4 shows graphical views of the effects of the PNWs on I-V performance parameters of the fabricated cells.

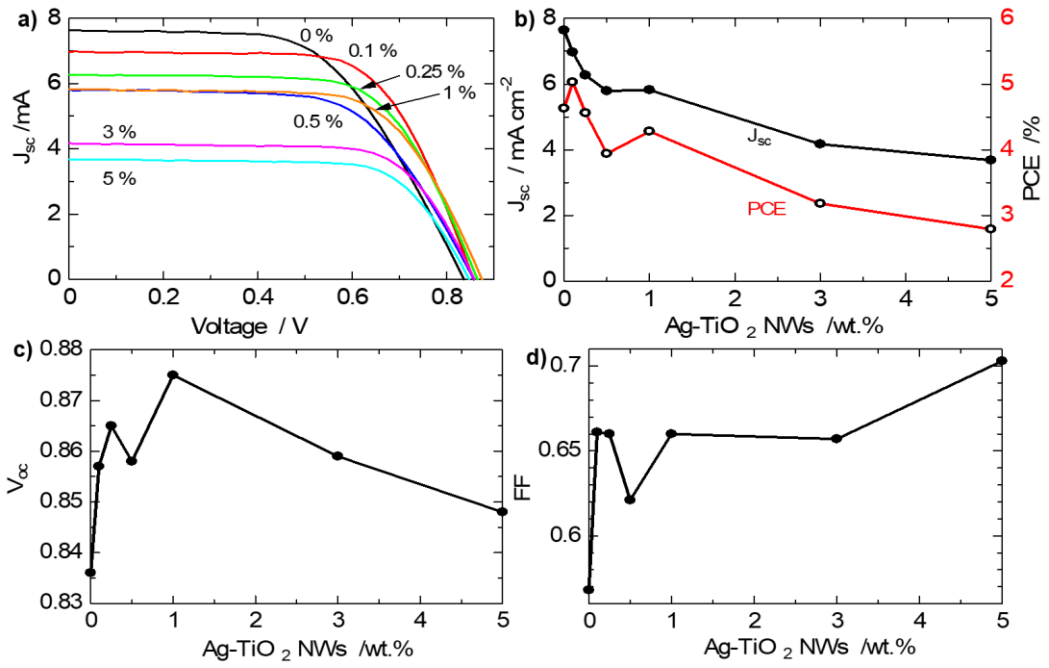

Fig. 5.4 Plasmonic NWs effect pattern curves on DSSC from I-V characterization: **a)** J-V; **b)** J_{sc} and PCE; **c)** V_{oc}; **d)** *FF*.

The PCE is given by, PCE = [J_{sc} x V_{oc} x FF]/P_{in}; P_{in} is incident power. Thus, the PCE is determined by the values of the three parameters of J_{sc}, V_{oc} and FF, and consequently all other factors that affect these three parameters. Hence it is observed from Fig. 5.4 a), and Table 5.1, that the PCE pattern does not follow the exact pattern of the J_{sc}. This is as a result of the varying effects on the PNWs on the above mentioned three parameters depending on the amount of PNWs loaded. There are the competing effects of enhancement of light absorption of the dye/DSSC from the LSPR effect, which leads to abundant photogenerated electrons and should lead to high J_{sc}. However, abundant photogenerated electrons in the CB of TiO_2 exponentially increases electron charge recombination with I_3^-/I^- electrolyte [29]; in addition the electron-sink effect of PNWs increase V_{oc} (by the upward shifting of the CB edge of TiO_2) which reduces charge injection efficiency, below a certain minimum threshold energy difference between the LUMO of the dye and the CB edge. Nevertheless, the electron-sink effect also increases charge separation and hence increases charge transfer resistance against recombination (R_{ct}) in addition to enhancing efficient charge transport, increasing FF. Additionally, the LSPR effect catalyzes the generation of trap states and depending on their distribution can shift the Fermi level of TiO_2 upwards or downwards, increasing or decreasing V_{oc}, respectively, and the consequent effects of that such as reduction or increment of charge recombination, respectively. Finally, the 1-D structure of the PNWs enhances electron transport which will lead to increased J_{sc} and FF. Thus, depending on the amount of PNW loading, these competing effects affect the performance parameters to varying extents, as shown in Fig. 5.4 and Table 5.1, and these combine synergistically to produce the different PCEs observed, Fig. 5.4 b) and Table 5.1.

5.3.4 EIS characterization

To corroborate the explanations given in the I-V results analysis, the electron kinetics of the fabricated DSSCs were investigated via EIS and the extracted charge parameters results are

shown in the last three columns of Table 5.1, and in Fig. 5.5. Fig. 5.5 a) shows the Nyquist plots of the DSSCs showing semi-/pseudosemi-circles of electron evolutions at various interfaces within the cells. Ideally, there should be as many semi-circles as there are electron transfers at interfaces in the cell make up, but three semi-circles are commonly seen due to some of these frequency response charge transfers processes coinciding. The typical three semi-circles are, the high frequency semi-circle (on the left), attributed to charge transfer processes at the counter electrode of a cell; the mid-frequency semi-circle, attributed to charge transfer processes in the electron transport semiconductor TiO_2 photoanode; and the low frequency semi-circle (on the right) resulting from charge transfer (ion diffusion) processes in the electrolyte component [30]. In this study the mid-frequency semicircles end points were obtained at 1000 and 3.16 Hz. Analysis of the high and low frequency semicircles showed no significant differences among the cells with their resistances at the real (Z'-) axis between 1-3 Ω. Thus, the PNWs did not affect these parts of the DSSCs. The series resistance, R_s, resulting from the conducting FTO substrates and external conducing wires, is obtained from the intersection of the high frequency semi-circle and the Z'-axis, was approximately the same for all cells, ~ 30 Ω, Fig. 5.5 a). This also indicates that the PNWs did not affect those components of the cells. However, when it comes to the mid-frequency semicircle, it is observed that it changes with PNW loadings, Fig. 5.5 a); especially with regards to the diameter, which is the resistance against charge recombination at the TiO_2-Dye-electrolyte interface, R_{ct}. The diameter increases with increasing PNW loadings, which is attributed to the electron-sink effect of these PNWs trapping photogenerated electrons and thus preventing them from recombining with the electrolyte, whiles efficiently transporting them. Thus, a large R_{ct} promotes efficient DSSCs. Nevertheless, it is common in reported plasmonic DSSC works [13, 15, 16, 31] for low R_{ct} values to be interpreted as good because the optimal most efficient cell usually has a lower or the lowest R_{ct}.

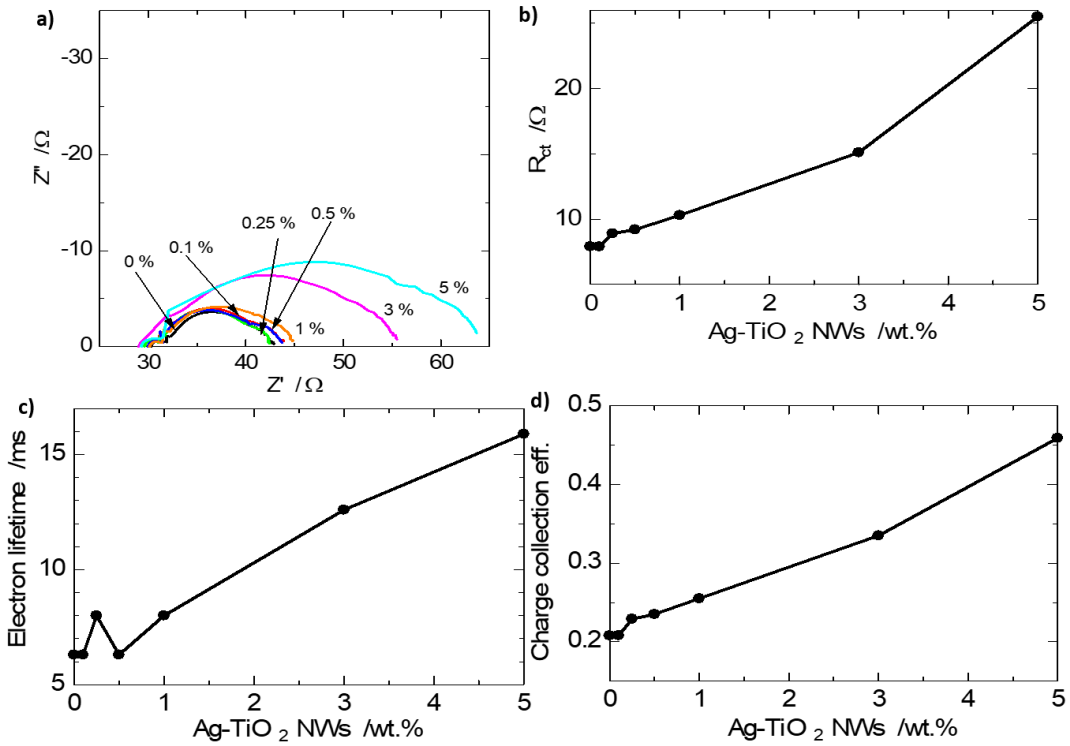

Fig. 5.5 a) Nyquist plots of the DSSCs and the PNWs effect pattern curves of extracted key parameters: **b)** charge recombination resistance; **c)** electron lifetime; and **d)** charge collection efficiency.

This is usually so because of one of two reasons or their combination: either the generation of deep trap states that lower the Fermi level (reduced V_{oc}) and hence increasing recombination to result in low R_{ct}; or abundant phogenerated electrons in the CB (from either LSPR energy transfer effect or efficient charge injection from optimal Fermi level lowering, or both) causing exponential charge recombination; or a combined effect of lowered Fermi level and abundant electrons in the CB. In this study the results followed the expected increasing trend, Fig. 5.5 b) and Table 5.1.

The electron lifetime, τ_n, measurement in DSSC is the perturbation of the Fermi level that induces the recombination by charge transfer; that is measurements in which excess charge carriers are not extracted at the contacts [32]. In other words the time taken for the system to return to equilibrium after the perturbation. But basically it indicates charge recombination: high or increased τ_n value indicates reduced charge recombination and a low or lowered τ_n value indicates increased charge recombination. Since the PNWs affected only the photoanode component of the DSSCs the discussion will focus on the τ_n of only that part. The τ_n of the photoanode is given by, $\tau_n = 1 / (2\pi f)$ [30]; f is the frequency at the maximum peak of the mid-frequency circle. Thus, this relation, with the Nyquist plots of Fig. 5 a), were used to obtain the τ_n values of Table 5.1 and the effect pattern trend of Fig. 5.5 c). The results indicate an increasing τ_n with increasing PNW loadings, attributed to the electron-sink effect causing effective charge separation and temporal trapping of the photogenerated electrons. Thus, reducing charge recombination. However, at 0.5 % PNW loading there is an apparent deviation from the trend with a decrease in the τ_n value from 8.0 ms of 0.25 % PNW loading to 6.3 ms. This is attributed to the catalyzed generation of trap states, observed as decrease in V_{oc}, and significant enough to cause significant charge recombination to reduce τ_n and FF.

The charge collection efficiency, η_{cc}, measures how efficiently electrons in the CB (injected photogenerated charges) are transported to the back contact FTO substrate of the photoanode. The η_{cc} values of Table 1 were obtained using the relation, $1 / [1 + (R_s / R_{ct})]$ [33]. The effect trend pattern is shown in Fig. 5.5 c). The effect of the PNWs on η_{cc} is increasing value with increasing PNW loadings. This is also attributed to the electron-sink effect causing efficient charge separation, temporal trapping and efficient transport of these electrons by the core Ag nanostructures, and efficient electron transport from the 1-D NW structure of these PNWs. The three key EIS parameters of R_{ct}, τ_n and η_{cc}, for the pristine sample and the optimal most efficient sample are the same. This is attributed to either the relatively low PNWs loading of

0.1 % or the effect of the intrinsic high V_{oc} of this system of DSSC under this study. It also indicates that the high enhancement in PCE by the PNWs is as a result of the balancing of the negative and positive competing effects of the PNWs, with particular notice to the V_{oc} and *FF*, since the J_{sc} value was lower than that of the pristine sample. Thus, with reference to the previous works [11, 12] at least one more optimal PNW loading concentration is predicted; with a lowering of the quasi Fermi level (lowered V_{oc}). This should then lead to efficient charge injection to obtain a higher J_{sc} than the pristine sample and ultimately a higher PCE than the 5.03 % obtained at the 0.1 % PNW loading; since the 1-D NW structure will enhance efficient charge transport to further reduce charge recombination.

5.3.5 IPCE

To investigate the PNWs effect on the performance of the DSSC relative to wavelength within the simulated solar radiation, an incident photon-to-current conversion efficiency, IPCE, evaluation was carried out. The results are shown in Fig. 5.6. The IPCE is also a measure of the combined efficiencies of light harvesting, charge generation, charge injection and transport, charge extraction and charge regeneration. Fig. 5.6 a) shows the IPCEs of the fabricated DSSCs. The results corroborate and show the same effect pattern of the PNWs on cell performance as observed in the I-V results and hence has the same explanations as under sections 5.3.3 and 5.3.4. Fig. 5.6 b) is the IPCE enhancement change obtained by subtracting the IPCE of the pristine sample (0 %; serving as a base line) from the IPCEs of the plasmonic samples. It shows that the most enhanced samples are samples of 0.1 and 1 % PNW loadings, with the most enhanced region being around 400 nm, the characteristic LSPR peak region of Ag, suggesting that the main LSPR energy transfer was via the radiative energy transfer mechanism, although there could be significant contribution via hot electron transfer but this determination is beyond this study.

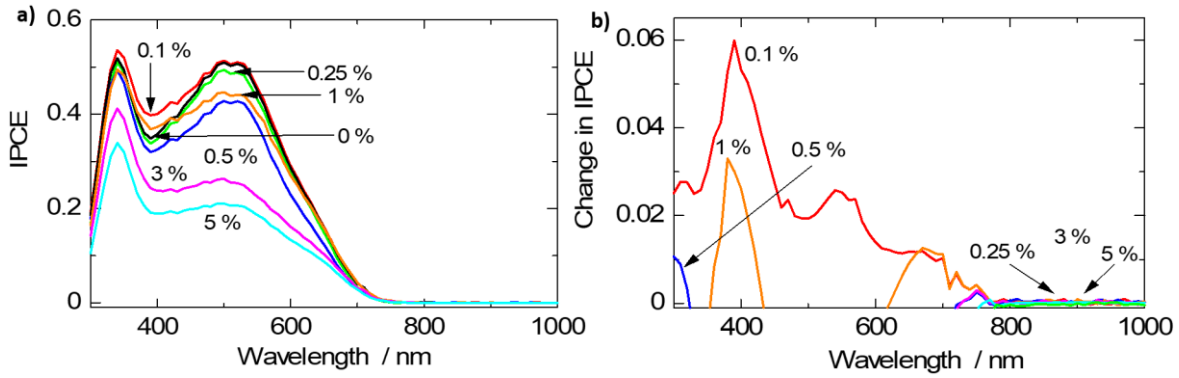

Fig. 5.6 a) IPCE curves of the DSSCs showing the PNWs effect on performance relative to wavelength; **b)** IPCE enhancement change: [IPCE of plasmonic DSSCs] – [IPCE of pristine sample].

The most efficient sample of 0.1 % PNW loading achieved almost a panchromatic enhancement effect, although the contributory effect at the NIR region is relatively insignificant. The rest of the samples showed enhancements only in the NIR region, attributed to poor charge injection efficiency in the visible region where most of the LSPR energy is generated. The relatively poor performance in the NIR, although the dyed photoanodes and PNW-enhanced dye light absorbance test results showed the most enhancement in the NIR region, is attributed to absorbance activity of deep trap states which cannot participate in power generation. The observed performance in the NIR region, although very low, may be from the PNWs acting as direct sensitizers to the TiO_2 semiconductor material since the N719 dye does not absorb light in this region. Further works to improve this minimal performance in the NIR can greatly improve the DSSC performance, since the NIR contains more than 40 % of the energy of the solar radiation.

5.3.6 DSSC stability

To investigate the stability and the TiO_2 shell protective effect on the core plasmonic Ag NWs, we measured the I-V performance of cells stored under dark with electrolyte after three days. Table 5.2 shows the results. The cells were stable with enhanced PCEs. There was a decrease in J_{sc} after the 3 days, including that of the pristine sample, indicating this was not the effect of the plasmonic NWs. The decrease in J_{sc} was attributed to poor charge injection as a result of upward shift of the conduction band of the TiO_2 nanocrystals after the 3 days, observed in the increased V_{oc}s. This increased V_{oc}s are attributed to the 4-*tert*-butylpyridine component of the electrolyte which makes an effective layering over the TiO_2 nanocrystals after the 3 days test period. This layering will also reduce the direct contact between the TiO_2 nanocrystals and the I_3^- ion species of the electrolyte which causes recombination, thus effectively reducing recombination as observed in the improved *FF*s in Table 5.2. However, this enhancement in FFs could have also come from the reduced electron density in the CB of TiO_2 (as in the reduced J_{sc}s) since it was established earlier that abundant charges in the CB exponentially increases recombination, hence, vice versa. Thus, these DSSCs were stable, especially when compared to studies such as Strandrich *et al.*'s [17] who experienced degradation of improperly protected PNSs after 15 h. Although we had expected some level of corrosion of the Ag core due to breakage of the NWs to expose the Ag core during the milling process, however the 3 day stability results suggest that opened end NWs were compactly sealed by TiO_2 P25 NPs during the photoanode preparation stage, most especially the calcination stage.

Table 5.2 I-V characterization results showing DSSCs stability after 3 days.

Sample	J_{SC} **/mA cm^{-2}**	V_{OC} **/V**	***FF***	**PCE /%**
0%	8.00	0.760	0.573	4.43
After 3 days	7.64	0.836	0.568	4.63
0.1%	8.23	0.767	0.596	4.79
After 5 days	6.97	0.857	0.661	5.03
0.25%	7.06	0.773	0.590	4.10
After 3 days	6.27	0.865	0.660	4.56
0.5%	7.03	0.776	0.560	3.89
After 3 days	5.79	0.858	0.621	3.94
1%	6.42	0.792	0.577	4.28
After 3 days	5.82	0.875	0.660	3.73
5%	2.25	0.780	0.689	1.54
After 3 days	3.68	0.848	0.703	2.79

5.4 Conclusion

Ag@TiO_2 PNWs were successfully prepared and incorporated into DSSCs to obtain enhanced DSSC performance from a pristine sample PCE of 4.63 to 5.03 % at a 0.1 % PNW loading. The key difference in the enhancement effect of this morphology of PNSs was efficient charge transport mainly contributed by the 1-D structure of NWs. The study, with reference to our previous studies and other reported plasmonic DSSC works shows some core effects of plasmonic nanostructures, independent of their morphology and material composition, with competing positive and negative effects. These core effects include enhancement of light absorbance; electron-sink effect that causes, effective separation of charges; upward shift of CB edge which reduces charge recombination, increases V_{oc} but reduces charge injection efficiency, especially at higher nanostructure loadings; catalyzes the generation of trap states which can also shift the Fermi level down or up with its consequent effects on charge injection and recombination. Thus this study has further broadened the understanding of the effect of plasmonic nanostructures on DSSC performance; and also increased the consensus on the observed effects so far. Thus, it serves as a good guide to further research work in this field and related fields.

Reference

1. IEA - Key world energy statistics (2017).
2. N. Lewis, Toward cost-effective solar energy use, *Science*, 2007, **315**, 798-801.
3. Best research-cell efficiencies, NREL, www.nrel.gov/pv/assets/images/efficiency-chart.png, (2017).
4. K. Kakiage, Y. Aoyama, T. Yano, K. Oya, J. Fujisawa and M. Hanaya, Highly-efficient dye-sensitized solar cells with collaborative sensitization by silyl-anchor and carboxy-anchor dyes, *Chem. Commun.*, 2015, **51**, 15894-15897.
5. W. R. Erwin, H. F. Zaricka, E. M. Talbert & R. Bardhan, Light trapping in mesoporous solar cells with plasmonic nanostructures, *Energy Environ. Sci.*, 2016, **9**, 1577–1601.
6. X.-C. Ma, Y. Dai, L. Yu and B.-B. Huang, Energy transfer in plasmonic photocatalytic composites, *Light: Science & Applications*, 2016, **5**, 1-13.
7. Y. H. Jang, Y. J. Jang, S. Kim, L. N. Quan, K. Chung and D. H. Kim, Plasmonic solar cells: from rational design to mechanism overview, *Chem. Rev.*, 2016, **116**, 14982-15034.
8. S. V. Boriskina, H. Ghasemi and G. Chen, Plasmonic materials for energy: From physics to applications, *Materials Today*, 2013, **16**, 375–386.
9. C. Wen, K. Ishikawa, M. Kishima and K. Yamada, Effects of silver particles on the photovoltaic properties of dye-sensitized TiO_2 thin films, *Sol. Energy Mater. Sol. Cells*, 2000, **61**, 339–351.

10. J. Du, J. Zhang, Z. Liu, B. Han, T. Jiang and Y. Huang, Controlled Synthesis of Ag/TiO_2 core−shell nanowires with smooth and bristled surfaces via a one-step solution route, *Langmuir*, 2006, **22**, 1307-1312.

11. P. Nbelayim, G. Kawamura, W. K. Tan, H. Muto and A. Matsuda, Systematic characterization of the effect of Ag@TiO_2 nanoparticles on the performance of plasmonic dye-sensitized solar cells, *Sci. Rep.*, 2017, **7**, 15690(1-12).

12. P. Nbelayim, G. Kawamura, Mohamed M. Abdel-Galeil, W. K. Tan, X. Wei, Hiroyuki, H. Muto and A. Matsuda, Effects of multi-sized and -shaped Ag@TiO_2 nanoparticles on the performance of plasmonic dye-sensitized solar cells, *J. Ceram. Soc. Jpn.*, 2018, **126**, 139-151.

13. P.-C. Huang, T.-Y. Chen, Y.-L. Wang, C.-Y. Wua and T.-L. Lin, Improving interfacial electron transfer and light harvesting in dye-sensitized solar cells by using Ag nanowire/TiO_2 nanoparticle composite films, *RSC Adv.*, 2015,**5**, 70172-70177.

14. G. Sahu, S. W. Gordon and M. A. Tarr, Synthesis and application of core-shell Au–TiO_2 nanowire photoanode materials for dye sensitized solar cells, *RSC Adv.*, 2012, **2**, 573-582.

15. K. Guo, M. Li, X. Fang, X. Liu, Y. Zhu, Z. Hu and X. Zhao, Enhanced properties of dye-sensitized solar cells by surface plasmon resonance of Ag nanowires core-shell structure in TiO_2 films, *J. Mater. Chem. A*, 2013, **1**, 7229-7234.

16. P.S. Chandrasekhar, H. Elbohy, B. Vaggensmith, A. Dubey, K. M. Reza, V. K. Komarala, Q. Qiao, Plasmonic silver nanowires for higher efficiency dye-sensitized solar cells, *Materials Today Energy*, 2017, **5**, 237-242.

17. S. A. Standridge, G. C. Schatz and J. T. Hupp, Toward plasmonic solar cells: protection of silver nanoparticles via atomic layer deposition of TiO_2, *Langmuir*, 2009, **25**, 2596–2600.

18. M. K. Nowotny, L. R. Sheppard, T. Bak and J. Nowotny, Defect chemistry of titanium dioxide. Application of defect engineering in processing of TiO_2-based photocatalysts, *J. Phys. Chem. C*, 2008, **112**, 5275–5300.

19. F. J. Knorr, C. Mercado and J. L. McHale, Trap state distributions and carrier transport in pure and mixed phase TiO_2: influence of contacting solvent and interphasial electron transfer, *J. Phys. Chem. C*, 2008, **112**, 12786–12794.

20. C. Mercado, Z. Seeley, A. Bandyopadhyay, S. Bose and J. L. McHale, Photolumiscence of dense nanocrystalline titanium dioxide thin films: effect of doping and thickness and relation to gas sensing. *ACS Appl. Mater. Interfaces*, 2011, **3**, 2281–2288.

21. K. Fredin, J. Nissfolk, G. Boschloo and A. Hagfeldt, The influence of cations on charge accumulation in dye-sensitized solar cells, *J. Electroanal Chem.*, 2007, **609**, 55-60.

22. G. Boschloo, L. Häggman, and A. Hagfeldt, Quantification of the effect of 4-*tert*-butylpyridine addition to I^-/I_3^- redox electrolytes in dye-sensitized nanostructured TiO_2 solar cells, *J. Phys. Chem. B*, 2006, **110**, 13144–13150.

23. M. Mojiri-Foroushani, H. Dehghani and N. Salehi-Vanani, Enhancement of dye-sensitized solar cells performances by improving electron density in conduction band of nanostructure TiO_2 electrode with using a metalloporphyrin as additional dye, *Electrochim. Acta*, 2013, **92**, 315–322.

24. M. Dhonde, K. Sahu, V.V.S. Murty, S. S. Nemala, P. Bhargava, Surface plasmon resonance effect of Cu nanoparticles in a dye sensitized solar cell, *Electrochimica Acta*, 2017, **249**, 89–95.

25. B. Roose, S. Pathak and U. Steiner, Doping of TiO_2 for sensitized solar cells, *Chem. Soc. Rev.*, 2015, **44**, 8326—8349.

26. Q. Xu, F. Liu, Y. Liu, W. Meng, K. Cui, X. Feng, W. Zhang and Y.Huang, Aluminum plasmonic nanoparticles enhanced dye sensitized solar cells, *Opt. Express*, 2014, **22**, A301-A310.

27. S. Meng, and E. Kaxiras, Electron and Hole Dynamics in Dye-Sensitized Solar Cells: Influencing Factors and Systematic Trends, *Nano Lett.*, 2010, **10**, 1238–1247.

28. S. K. Pathak, A. Abate, P. Ruckdeschel, B. Roose, K. C. Go¨del, Y. Vaynzof, A. Santhala, S.-I. Watanabe, D. J. Hollman, N. Noel, A. Sepe, U. Wiesner, R. Friend, H. J. Snaith and U. Steiner, Performance and Stability Enhancement of Dye-Sensitized and Perovskite Solar Cells by Al Doping of TiO_2, *Adv. Funct. Mater.*, 2014, **24**, 6046–6055.

29. S. A. Haque, Y. Tachibana, D. R. Klug and J. R. Durrant, Charge recombination kinetics in dye-sensitized nanocrystalline titanium dioxide films under externally applied bias, *J. Phys. Chem. B*, 1998, **102**, 1745-1749.

30. M. Adachi, M. Sakamoto, J. Jiu, Y. Ogata, and S. Isoda, Determination of parameters of electron transport in dye-sensitized solar cells using electrochemical impedance spectroscopy, *J. Phys. Chem. B*, 2006, **110**, 13872-13880.

31. S. P. Lim, A. Pandikumar, H. N. Lim, R. Ramaraj and N. M. Huang, Boosting photovoltaic performance of dye-sensitized solar cells using silver nanoparticle-decorated N,S-co-doped-TiO_2 photoanode, *Sci. Rep.*, 2015, **5**, 11922.

32. J. Bisquert, F. Fabregat-Santiago, I. Mora-Sero´, G. Garcia-Belmonte and S. Gime´nez, Electron lifetime in dye-sensitized solar cells: theory and interpretation of measurements, *J. Phys. Chem. C*, 2009, **113**, 17278–17290.

33. J. Nissfolk, K. Fredin, A. Hagfeldt and G. Boschloo, Recombination and transport processes in dye-sensitized solar cells investigated under working conditions, *J. Phys. Chem. B*, 2006, **110**, 17715–17718.

Chapter 6

General conclusion

This thesis study can be summarized as shown in Fig. 6.1 below. This study aimed at using the unique phenomena of nanotechnology with the nonoscience understanding of materials of concern to fabricate improved versions of advanced electrochemical devices under the two themes of superhydrophobicity-electrowetting (theme 1) and dye-sensitized solar cells (theme 2).

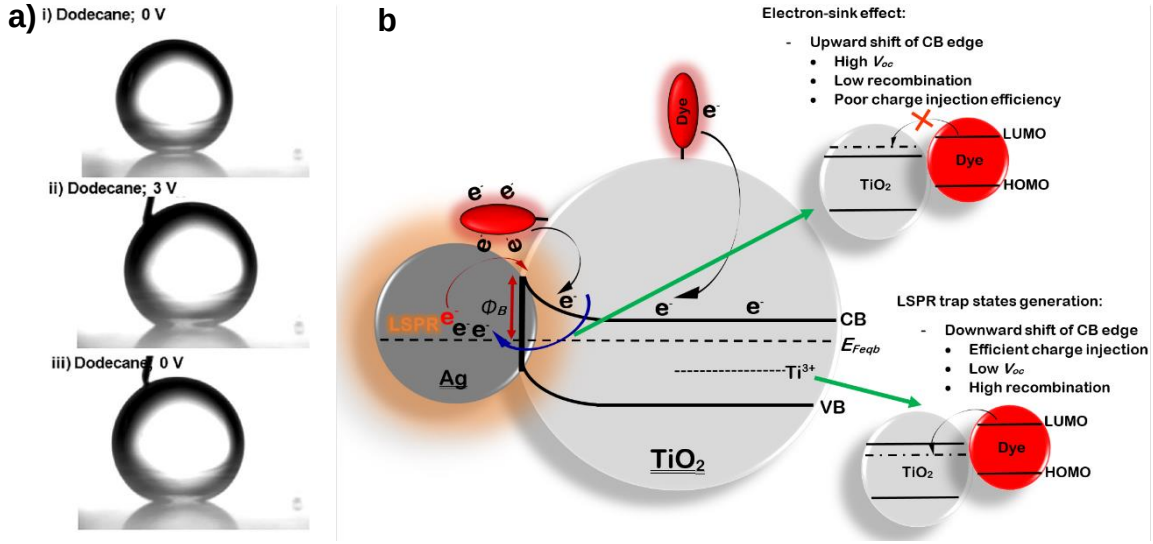

Fig. 6.1 A summarry figure of the studies under this thesis: **a)** extremely low actuation voltage reversible electrowetting on a robust superhydrophobic coating under theme 1, superhydrophobicity-electrowetting; and **b)** the complex effects of plasmonic nanostructures on the electron kinetics in a DSCC.

We successfully prepared nano coatings of Alumina (pseudoboehmite) with about 4 nm thick hydrophobizing coating under theme1; and various Ag@TiO_2 core-shell nanostructures under theme 2.

Under theme 1 we obtained a robust SHS of a CA of 162.7° with 3 μL droplet and a robust electrowetting surface with an unprecedented low actuation voltage of 3 V, in addition to a reliable stability uncommon in nanoscale coated electrowetting surfaces.

Under theme 2 of plasmonic DSSCs, we were able to use the LSPR phenomenon of Ag, in the form of various Ag@TiO_2 C-S NSs, to enhance the PCEs of DSSC; and in addition obtained significant information on the effects of the plasmonic nanostructures on the performance of DSSCs which include:

1. Enhancement of: light absorbance across the UV-Vis-NIR; *FF*; R_{CT}; τ_n; and η_{cc}.

2. Upward shift of the Fermi level of TiO_2 which results in higher V_{oc}s but causes poor charge injection efficiency.

3. There are more than one optimal plasmonic NS loading concentrations to obtain the best enhanced performance DSSCs; a significant occurrence never communicated before, and

4. Destructive and constructive interference effects of LSPR modes.

The electrowetting results are preliminary with a vast opportunity of more improvement such as employing a thermally stable conductive nano coating, or a longer HWT period, in order to obtain longer rough structures to ultimately obtain a wide-range working electrowetting CA. The plasmonic effects under the DSSC study confirmed reported results and revealed new effects observations. Thus, the results of these studies are significant and will serve as good guides for further research in these fields, and also for possible industrial applications.

Acknowledgement

My greatest thank-you goes to my supervisor, Professor Atsunori Matsuda, for giving me the opportunity and trust to study in his laboratory; including his contributions in the facilitation and sponsoring of my many scientific conferences I attended which were no small source of knowledge and experience; and also for containing my idiosyncrasies. And in addition his regime to mold us, his students, into the best scientist we can be.

Thanks to his assistant, Assistant Professor Go Kawamura, for his tough questions and strict adherence to our weekly research progress discussions and other academic activities which challenged me to study and gain an in-depth understanding of my research work; and his invaluable coordinating work in the laboratory.

However, without Professor Masanobu Izaki I probably wouldn't have known Toyohashi University of Technology (TUT) and Prof. Matsuda; and who has also accepted to be one of the reviewers of my thesis defense. We met at a 4 month Japan International cooperation Agency (JICA) training program at Osaka Municipal Technical Research Institute (OMTRI), Osaka, 2007, where he was a researcher and one of our trainers. So, thank you Prof. Izaki. This automatically calls for a thank you to Mrs Miki Wada, who was our wonderful JICA coordinator at this training program and whose invaluable coordination and encouragement pushed me to choose to study at TUT.

I also thank Prof. Hiroyuki Muto, who is one of my supervisors in our laboratory and also one of the reviewers of my thesis, for his guidance especially in regards to good laboratory and research attitudes. In addition, I thank Assoc. Prof. Toshiaki Hattori who, notwithstanding his busy schedule, has also accepted to be one of the reviewers for my thesis.

I am very grateful to the Ministry of Education, Culture, Sports, Science and Technology (MEXT) scholarship which sponsored my studies and livelihood for a total of 5 years in TUT (2008-2010 for my Master's program and 2014-2017 for my PhD program). I haven't only

gained scientific knowledge but about peaceful and beautiful Japan (its rich culture and history) in addition to meeting many international friends, which go a long way to influence my global outlook perspective.

Thanks to Drs. Nguyen Huu Huy Phuc; Teruhisa Okuno; Xing Wei; Shota Azuma and Mohamed M. Abdel-Galeil who taught me how to use most of the characterization equipment in our laboratory related to my research, and in other diverse ways to support my research work. In fact thanks to all our lab members who also supported in no small diverse ways and for creating a convenient atmosphere for my studies. Not forgetting our lab secretary, Mrs Ookawara, Mrs Suzuki and Mrs Yogo, who were invaluable in coordinating our academic lives related to the lab, especially our scientific conference trips and social lives, especially in regards to our responsibilities and opportunities as residents of Japan.

Thank you to Project Assistance Prof. Wai Kian Tan, who supported us, especially international students, with his invaluable experience, both academically and socially.

A big thank you to my family, especially my parents, Mr John Fuseini and Mrs Janet Seini, who constantly called with their parental love; and to my kids, Mae, Miki and Marcel, they were an inspiration in all this.

And I know all these happened by the grace of God. Thanks be to God.

List of Publications

1. **Pascal Nbelayim**, Hisatoshi Sakamoto, Go Kawamura, Hiroyuki Muto and Atsunori Matsuda. Preparation of thermally and chemically robust superhydrophobic coating from liquid phase deposition and low voltage reversible electrowetting, *Thin Solid Films*, **636** (2017) 273-282.

2. Xing Wei, **Pascal Sugri Nbelayim**, Go Kawamura, Hiroyuki Muto and Atsunori Matsuda, Ag nanoparticle-filled TiO_2 nanotube arrays prepared by anodization and electrophoretic deposition for dye-sensitized solar cells, *Nanotechnology*, **28** (2017) 135207 (1-8).

3. **Pascal Nbelayim**, Go Kawamura, Wai Kian Tan, Hiroyuki Muto and Atsunori Matsuda, Systematic characterization of the effect of $Ag@TiO_2$ nanoparticles on the performance of plasmonic dye-sensitized solar cells, *Sci. Rep.*, **7** (2017) 15690 (1-12).

4. **Pascal Nbelayim**, Go Kawamura, Mohamed M. Abdel-Galeil, Wai Kian Tan, Xing Wei, Hiroyuki Muto and Atsunori Matsuda, Effects of multi-sized and -shaped $Ag@TiO_2$ nanoparticles on the performance of plasmonic dye-sensitized solar cells, *J. Ceram. Soc. Jpn.*, **126** (2018) 139-151.